UNIVERSITY OF COPENHAGEN
FACULTY OF SCIENCE

The Sensitivity of the Southern Ocean Circulation to Local Wind Stress Forcing in a Coarse Resolution Coupled GCM

Mads Bruun Poulsen

Supervisor: Prof. Markus Jochum

Submitted: October 15th

Abstract

The intense southern hemisphere westerlies are believed to exert a strong control on the slope of the Southern Ocean isopycnals and the strength of the associated Antarctic Circumpolar Current (ACC). However, the absence of a response in the ocean density structure to the observed ongoing intensification of these winds has motivated a reassessment of the Southern Ocean dynamics. Recent studies have emphasized the compensating role of mesoscale eddies on the circulation, and the sensitivity of the circumpolar transport to wind stress variability is presently debated.

This thesis uses the output from a 1000 yr control integration of the fully coupled coarse resolution Community Climate System Model 4 to investigate this dynamical relationship. Four different measures of the wind stress are evaluated to understand in what way the winds drive the circulation. Moreover, the response of the baroclinic circumpolar transport to wind stress variability is addressed by developing a measure of the large-scale isopycnal slope through the use of the baroclinic potential energy.

It is here shown that the zonal wind stress over the path of the ACC is a useful forcing metric, and that it correctly predicts the relevant ocean Ekman transports. Using this metric, it is found that the isopycnal slope and the baroclinic transport of the ACC responds significantly to changes in the wind stress. This conclusion is supported by a detailed study in the three strongest multi-decadal internal wind stress trends of the model run.

However, recent studies have questioned the capability of coarse resolution models in adequately representing the effect of the mesoscale eddies. This work finds that the model eddies only marginally compensate the variability in the wind-driven circulation, which conflicts with the output from eddy resolving models. This points at an overestimation of the ocean response to wind stress variability that is presented in this thesis. The shortcoming of the model in correctly capturing the dynamical response is partly ascribed to the present formulation of the eddy transfer coefficient in the implemented eddy mixing parameterization.

Resumé

Hældningen på isopyknalerne i det Sydlige Ishav og styrken af den dertil knyttede Antartiske Circumpolare Havstrøm (ACH) er ofte tilskrevet det kraftige vestenvindsbælte på den sydlige halvkugle. Udeblivelsen af en ændring i havets densitetsstruktur, som funktion af de nuværende intensiverende vinde, har dog motiveret en revurdering af de gældende dynamiske forhold. Nylige studier har påvist at turbulente effekter spiller en kompenserende rolle på cirkulation, og følsomheden af den circumpolare transport overfor ændringer i vindforholdene er derfor taget op til diskussion.

Dette speciale anvender output'et fra en 1000år lang integration af den groft-opløste Community Climate System Model 4 i sin fuldt koblede konfiguration, for at undersøge dette dynamiske forhold. Fire forskellige mål for vindens kraftpåvirkning på oceanet bliver efterprøvet i et forsøg på at forstå hvordan vindene driver cirkulationen. Derudover bliver forholdet mellem den barokline circumpolare transport og ændringerne i vindens kraftpåvirkning på oceanet undersøgt, gennem udviklingen af et mål for hældningen på isopyknalerne ved analyse af den barokline potentiale energi.

Det bliver her påvist at de zonale vinde over ACH'ens strømningslinjer er brugbare i forhold til havstrømmens forcering, og at disse vinde på korrekt vis forudsiger de relevante Ekman transporter i oceanet. Ved brugen af dette mål for vindstyrken bliver det vist at hældningen på isopyknalerne og den barokline transport af ACH'en reagerer signifikant som funktion af ændringer i vindene. Denne konklusion er understøttet af et detaljeret studie af de tre kraftigste 50års vindtendenser i modelkørslen.

Nylige studier har dog sået tvivl om hvorvidt groft-opløste modeller er i stand til at modellere effekten af de turbulente forhold på mesoskalaen på korrekt vis. Dette studie påviser at styrken på de turbulente strømme kun marginalt balancerer de vinddrevne, hvilket ikke stemmer overens med output'et fra højere opløste modeller. Dette tyder på at de her præsenterede udsving i den barokline transport som funktion af variabiliteten i vindene er overvurderet. At modellen ikke er i stand til at modellere de dynamiske forhold er delvist tilskrevet den nuværende formulering af koefficienten i den implementerede parameterisering for turbulens.

Preface

With the submission and defense of this thesis I end a five year long education in physics. Reflecting upon what I have been taught, it is difficult to express in words exactly what skills I have acquired, but at least I can say that I (hopefully) have learnt how to think as a physicist. That is, where I was marvelled by nature when I applied for my education back in 2010, I also marvel today, but certainly in a different way, because I can appreciate the greater picture. Understanding that Newtonian mechanics is just a limiting case of a greater truth, or recognizing the vast range of orders of magnitude in time and space of which the universe and its associated physical systems span, are two good examples. An education is physics really makes you feel as a smaller person. In an appreciation of this, I hope that this education marks the first stepping stone out of many in a walk through the world of physics.

First of all I would like to thank Matt and Sarah for providing the inspiration to this thesis work during my stay at SIO in the spring of 2014. It has kept me going until this very end. Markus, my supervisor, also deserves a good amount of gratitude for his guidance and help throughout this last year. I am also grateful to Søren, Christian and Kasper for prolonged coffee breaks when they were needed the most. The biggest thanks, however, goes to Helen for spending a tremendous amount of her time on lengthy physics discussions with me, and reading through some of my temporary writings. She surely has taught me how to take ownership of my own thesis and sound a wee bit more as a brit in my scientific writing.

_____ _____

Signature Date

Contents

Chapter 1

Introduction

Due to the Drake Passage, the opening between the southern tip of South America and the Antarctic Peninsula, the upper part of the Southern Ocean (SO) is subject to a latitude band that is unblocked by topography. This gap facilitates the near-zonal Antarctic Circumpolar Current (ACC), which flows eastward around the Antarctic continent, and carries a volume transport of approximately 130 Sv ($1\,\mathrm{Sv} \equiv 1 \times 10^6\,\mathrm{m^3 s^{-1}}$) - the strongest current observed on the planet (Cunningham et al., 2003).

The SO is also associated with strong meridional gradients in temperature and salinity, which cause isopycnals to shoal poleward and outcrop, and allow water from the interior ocean to upwell adiabatically. This hydrographic property, together with observations of dissolved oxygen (figure 1.1), is often taken as evidence of a Meridional Overturning Circulation (MOC), fed by salty, relatively warm, oxygen-depleted North Atlantic Deep Water (NADW) (Marshall and Speer, 2012).

Thus analog to a crossroad, the SO is the part of the world's ocean where physical, chemical and biological tracers are exchanged between the three major oceans (Thompson, 2008), and where overturning ventilates the deep ocean, with implications for the atmospheric carbon-dioxide balance (Sigman and Boyle, 2000) and the distribution of heat on Earth (Knauss, 2005). Consequently the SO is regarded a key component to the climate system, and therefore attracts much attention in the oceanographic community.

Together with buoyancy forcing, the mid-latitude westerlies in the Southern Hemisphere (SH) (figure 1.2) are an important driving force of the SO circulation (Rintoul and Garabato, 2013). These winds are some of the strongest on Earth (Yuan, 2004), and a major source of energy to the ocean general circulation (Wunsch, 1998).

The variability of these winds is mainly captured by the Southern Annular Mode (SAM), which is a large-scale oscillation with a circumpolar structure (Marshall, 2003).

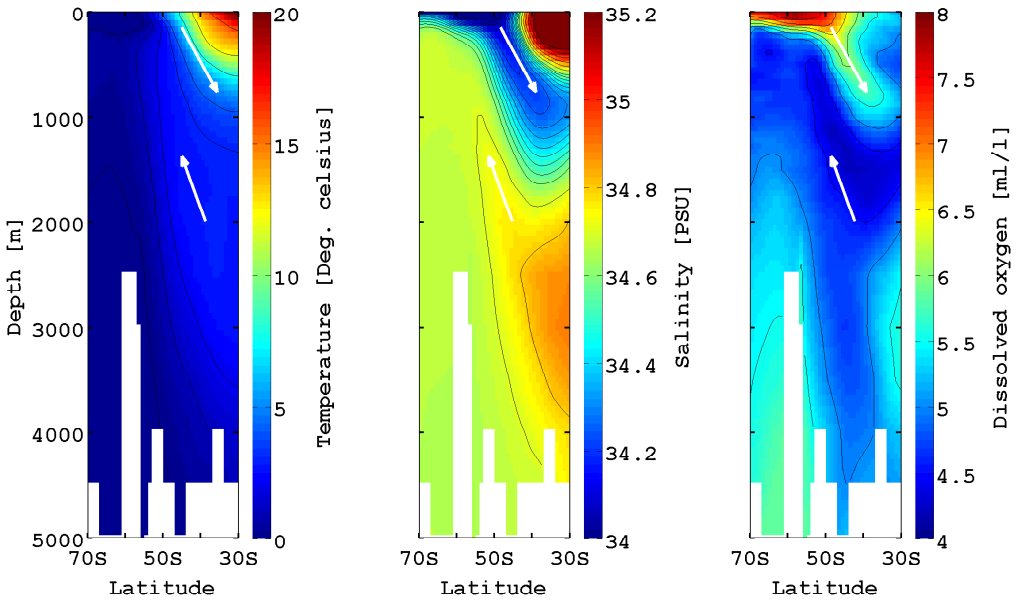

Figure 1.1: Temperature (left panel), salinity (middle panel) and dissolved oxygen (right panel) transsections at 26°W. Data is from the World Ocean Atlas 2009. White color either denote topography or missing data. The figure is inspired by Marshall and Speer (2012), and indicates how relatively warm, salty, oxygen-depleted North Atlantic Deep Water upwells, transforms at the surface, and downwells, forming the upper cell of the Meridional Overturning Circulation. Arrows indicate direction of flow.

This mode of variability is often described by the leading Empirical Orthogonal Function (EOF) of various property fields, as for example the Sea Level Pressure (SLP), where the pressure field anomalies of the SH mid- and polar latitudes are in anti-phase (Thompson and Wallace, 2000). The large-scale atmospheric isobar thus oscillates like a seesaw in the meridional plane on many different timescales (Solomon and Thompson, 2002), and produces near zonally symmetric intensifactions and weakenings of the westerlies.

Since the 1970s there has been a statistically significant trend towards the positive phase of the SAM (stronger westerlies) (Marshall, 2003), and this trend has been tied to Antarctic ozone loss and increases in the atmospheric concentration of green house gasses (Solomon and Thompson, 2002). Therefore much scientific effort has recently been devoted to understand how the ACC transport and MOC respond to variability and trends in local wind forcing (e.g. Hallberg and Gnadadesikan, 2006; Hogg and Blundell, 2006; Sallée et al., 2008; Böning et al., 2008; Munday et al., 2013; Kim and Orsi, 2014).

Fundamentally, the baroclinic transport of the ACC is intimately linked to the meridional density gradient through thermal wind balance,

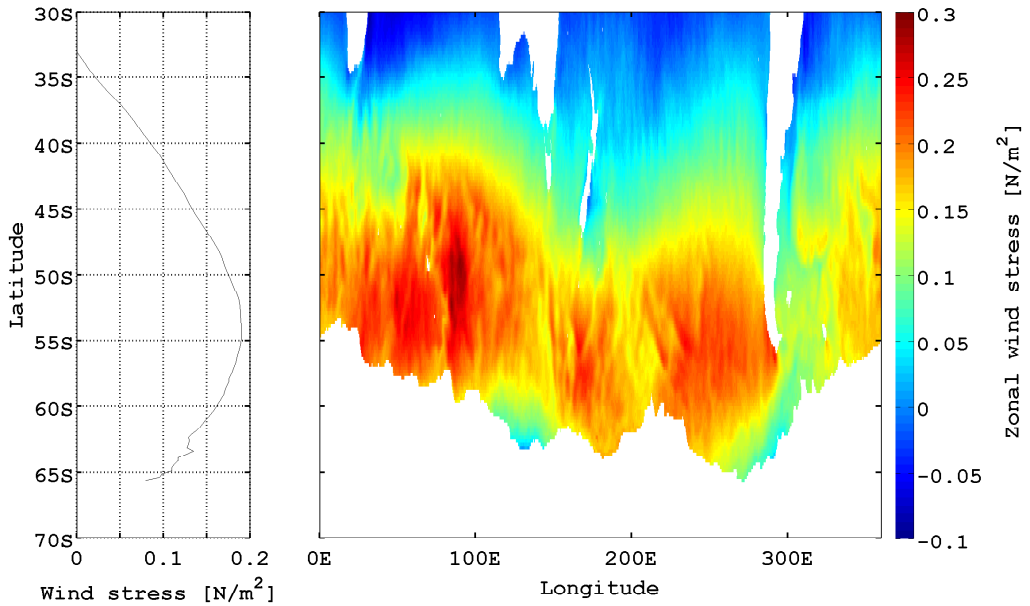

Figure 1.2: Left panel: Zonally-averaged zonal wind stress derived from the 2008-2010 temporal mean wind stress field. The wind strength is obtained from the ASCAT satellite scatterometry (data is available at www.remms.com) product and is translated into wind stress by using the bulk formulae by Large and Yeager (2004). The calculation is relative to a static ocean surface and the wind stress is therefore slightly overestimated. Right panel: The 2008-2010 temporal mean zonal wind stress field. Units are N/m^2.

$$f\frac{\partial \boldsymbol{u}_g}{\partial z} = -\frac{g}{\rho_0}\boldsymbol{k} \times \nabla_2 \rho, \tag{1.1}$$

because the large-scale ocean circulation is in geostrophic and hydrostatic balance (Vallis, 2006). Here f is the Coriolis parameter, $\boldsymbol{u}_g = (u_g, v_g)$ is the horizontal geostrophic velocity field, g is the gravitational constant, ρ_0 is a reference density, $\boldsymbol{k}$ is the vertical unit vector, ∇_2 is the horizontal gradient operator and ρ is the density field. Understanding the relationship between the wind forcing and the baroclinic transport of the ACC thus means understanding how, and to what extent, the winds shape and maintain the density structure of the SO.

The SH westerlies drive an equatorward ageostrophic Ekman drift in the ocean surface, and continuity requires a poleward flow below this transport. The open Drake Passage latitude band strongly constrains such a return flow in the upper ocean, because there is no topography to support a zonal pressure gradient, and hence a net meridional geostrophic flow is prohibited. If the Ekman drift is to be balanced by a geostrophic return flow, it has to take place at depth where topography exists (Thompson, 2008).

The pioneering coarse resolution model-study by Toggweiler and Samuels (1995) suggests that the equatorward surface flow and the deep poleward flow are coupled through Ekman divergence, and hence upwelling, due to the shear in the surface wind stress. This mechanism tilts the isopycnals, such that they shoal poleward and outcrop, allowing dense NADW to upwell adiabatically. The water that upwells is converted into lighter water through buoyancy forcing at the surface and is transported northward with the Ekman drift. The rate of upwelling, and the meridional density gradient and the associated baroclinic transport, is thus controlled by the strength of the zonal wind stress at the northern limit of the Drake Passage, in their non-eddy model experiment.

Christened *The Drake Passage Effect*, this physical process challenges the traditional idea of uniform upwelling through the thermocline (Stommel and Arons, 1959), and directly relates the strength of the Atlantic Meridional Overturning Circulation (AMOC) to the SO winds. The hypothesis is supported by other coarse resolution General Circulation Model (GCM) experiments (Gent et al., 2001; Fyfe and Saenko, 2006), where both the circumpolar transport and the overturning is found to strengthen with intensifying winds.

However, advances in satellite altimetry throughout the last few decades have shown that the SO is rich in eddies (figure 1.3), and their role in SO dynamics is currently a topic of much debate. Most of the SO eddies are at the mesoscale, with a characteristic length scale of tens of kilometers (Chelton et al., 1998), and they are seen to concentrate around frontal regions (Thompson, 2008) and in the lee of topography (Thompson and Garabato, 2014). Fronts (figure 1.4) are traditionally observed in hydrographic data (Orsi et al., 1995), but are also seen in satellite altimetry data (Gille, 1994; Sallée et al., 2008), and defines the transition between two different water masses. They are associated with a relatively strong isopycnal slope, and carry most of the circumpolar transport (Talley et al., 2011). Instability of these fronts, or jets, generate eddies, but eddies are also able to feed back on the mean-flow, and accelerate the fronts, much like atmospheric storm tracks (Williams et al., 2007).

Todays computing capacity promotes higher model grid resolution in ocean GCMs, which allows for the explicit generation of eddies and better resolved topography. The output from these high resolution models confirm that eddies have an important effect on the SO circulation. They are a vital component to the dynamical balance of the ACC, where they transfer momentum in the vertical through interfacial form stress (Johnson and Bryden, 1989), facilitating dissipation at the bottom through form drag (Ivchenko et al., 1997), as envisioned by Munk and Palmén (1951).

Model eddies are also able to supply some of the surface Ekman transport by a

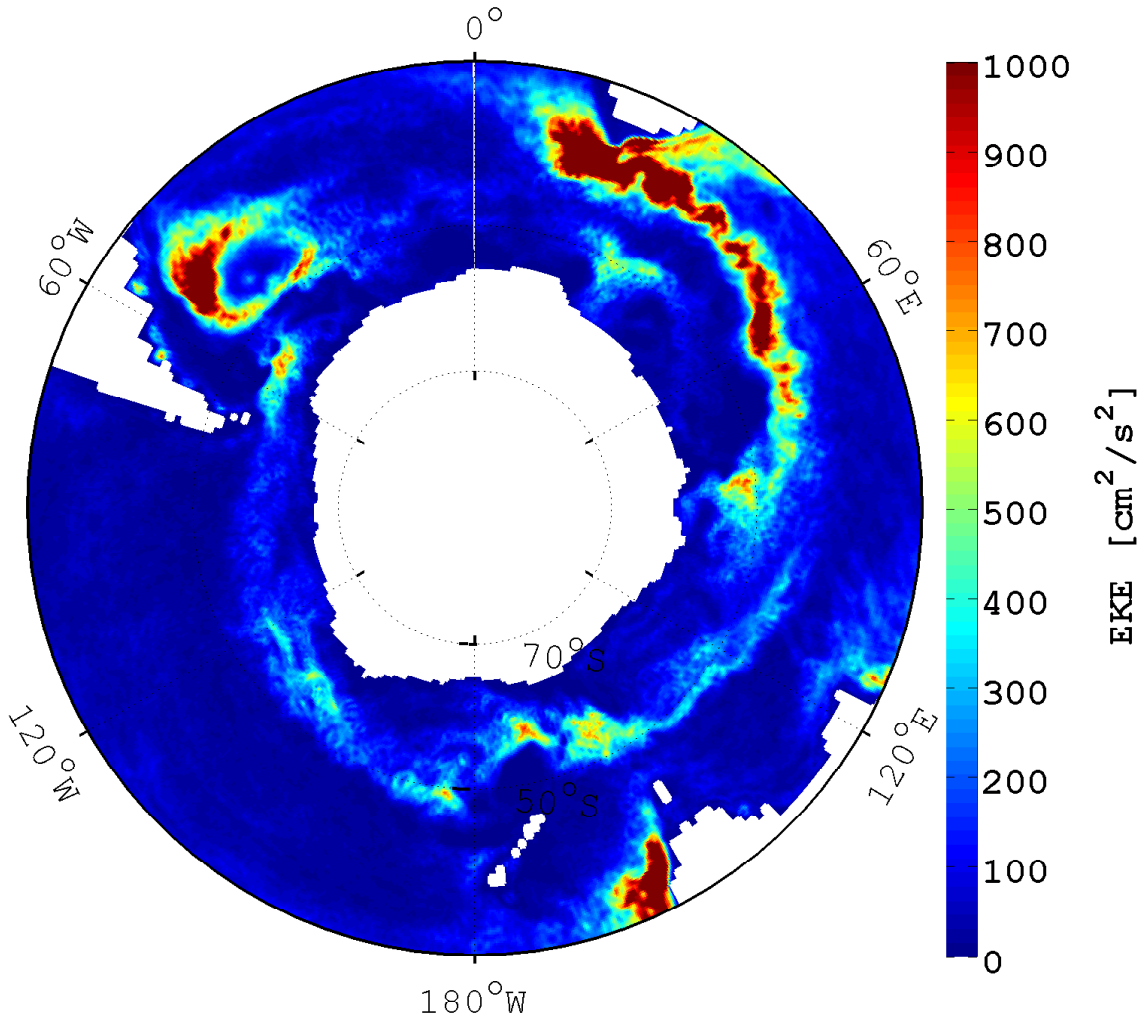

Figure 1.3: 2008-2010 temporal mean surface geostrophic eddy kinetic energy (EKE) field. The surface geostrophic velocity field used to calculate the EKE (EKE = $(u_g'^2 + v_g'^2)/2$, where u_g' and v_g' are the zonal and meridional geostrophic velocity anomalies, respectively, with respect to the 2008-2010 temporal mean) is derived from 7-day mean observations of the sea surface height, provided by the $1/4^\circ$ degree AVISO altimetry product (data is available at www.aviso.altimetry.fr/en/home.html).

poleward transport of water above topography, and compensate some of the effect of the winds on the overturning strength (Hallberg and Gnadadesikan, 2006). These eddies draw their energy from the large-scale available potential energy (APE) through baroclinic instability (Storch et al., 2012), and reduce the isopycnal slope and ACC transport (Langlais et al., 2015). In fact, beyond a certain wind stress magnitude threshold, the eddies are seen to decouple the wind stress strength from the circumpolar transport, as for example seen in the numerical experiments by Munday et al. (2013) - a phenomenon known as eddy saturation (Meredith and Hogg, 2006).

The explanation to the marked contrast between the SO circulation obtained from the coarse resolution model experiments (Fyfe and Saenko, 2006) and the eddy-resolving runs (Hallberg and Gnadadesikan, 2006) is partly to be found in the way eddies are represented in the former type of model. Because the characteristic length scale of the eddies is smaller than the grid discretization, the effect of the eddies needs to be parameterized. A common choice is to use the GM-parameterization scheme (Gent and McWilliams, 1990; Flato et al., 2013), where the advection by the eddies is a function of the large-scale density field and the thickness diffusivity κ_{GM}.

Where this parameterization successfully captures the ocean mean-state in terms of the poleward heat transport using a constant thickness diffusivity (Gent et al., 1995), Munday et al. (2013) shows that it fails to mimic eddy compensation and saturation during changes in local wind forcing, and ascribe the problem to κ_{GM}. Since coarse resolution models with parameterized eddies are important to enable long climate integrations, a correct eddy closure is paramount, and a substantial part of todays research goes into specifying κ_{GM} (See for example Visbeck et al., 1997; Ferreira et al., 2005; Eden and Greatbatch, 2008).

This debate in the modelling community has been weakly guided by observations, but the recent observational study by Böning et al. (2008) supports the results from the eddy-resolving models. They survey historical hydrographic data and profiles obtained from the autonomous Argo floats to assess changes in the SO circulation during the late 20th century on a climatic timescale. Despite finding significant trends in both the temperature and the salinity field, and an overall depression of the isopycnal surfaces, they report minimal changes in the isopycnal slope, and hence an insensitive response of the baroclinic transport of the ACC to the intensifying winds.

They speculate that the excess energy from the wind drives a stronger eddy field that compensates changes in the overturning, instead of entering the mean-flow. This notion is supported by additional observations of the SO published in the present decade, which show a steady Drake Passage transport (Meredith and Coauthors, 2011), but an elevated

level of eddy kinetic energy (EKE) (Hogg et al., 2015). Evidence from observational and eddy-resolving model studies are thus compiling in favor of a relatively insensitive SO circulation, and questioning the ability of coarse resolution ocean models to correctly capture the dynamical response to the intensifying mid-latitude westerlies.

Many of the eddy-resolving model studies are however quite idealized with respect to basin geometry and bottom topography (Hogg et al., 2008; Munday et al., 2013), atmospheric forcing (Hallberg and Gnadadesikan, 2006; Nadeau and Straub, 2009) and governing equations (Hogg and Blundell, 2006; Nadeau and Straub, 2012), in order to make long model integrations possible. These simplifications might have a crucial impact on the model output. For example, none of the mentioned studies agree on the wind stress threshold at which eddy saturation occurs, or which amount of eddy compensation is appropriate, and idealized basin geometry has also been found to suppress important physics (Jochum and Eden, 2015).

Moreover, even though the SAM describes most of the wind stress change in the SO, other modes, such as the El Niño-Southern Oscillation (ENSO), also explain a significant fraction of the variability of the wind field, which is known to have an effect on the response of the SO circulation (Sallée et al., 2008; Morrow et al., 2010; Langlais et al., 2015). For example it has been shown that wind stress anomalies along the coast of Antarctica are able to generate a barotropic ocean response, without visible changes in the baroclinic component (Zika et al., 2013). In addition, the ACC transport sensitivity to wind stress changes has been demonstrated to have a spatial structure that departs from zonal symmetry (Mazloff, 2012), and wind stress forcing remote to the SO also influences the circulation (Allison et al., 2010). This questions if the wind stress variability tied to the SAM is a relevant measure with respect to predicting the SO circulation response.

Motivated by these recent studies and their shortcomings, and in the framework of a fully-coupled climate model with GM-parameterized eddies and a refined specification of the thickness diffusivity, this dissertation addresses the following scientific questions:

1. Which measure of the SO wind stress is useful to understand variability in the SO circulation?

2. Given the eddy parameterization, how well does this climate model eddy compensate and saturate with respect to the results from eddy-resolving models?

3. How does the barotropic ACC component respond to the SO wind stress?

4. By applying the method by Böning et al. (2008) to the model output, how robust

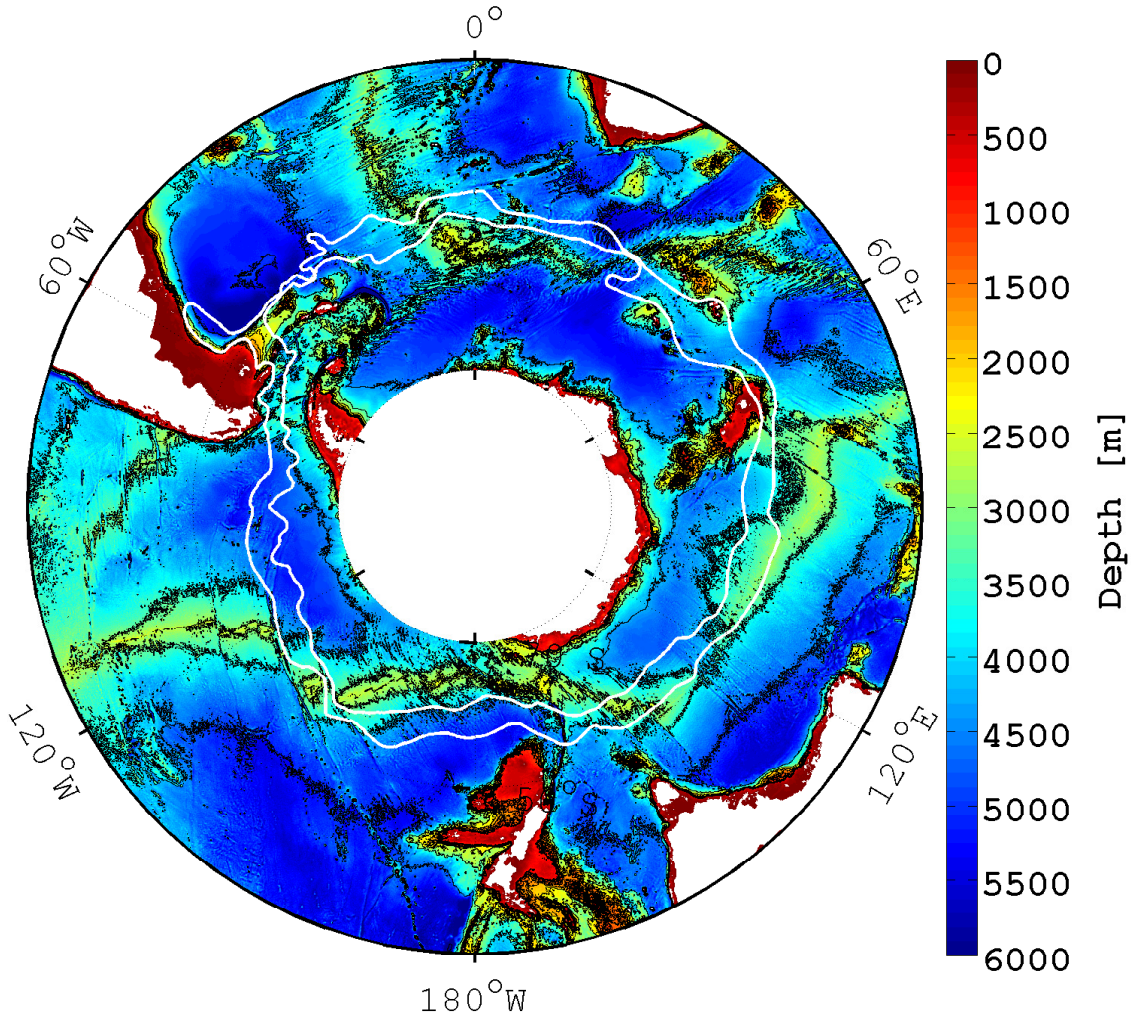

Figure 1.4: Topography of the Southern Ocean, inferred from satellite altimetry and ship depth measurements, and is documented in Smith and Sandwell (1997). The white bold lines are the time-mean positions of the subantarctic front and the polar front, identified by Orsi et al. (1995). The black solid lines are contours of f/h, where f is the Coriolis parameter and h is the ocean depth. Note how the fronts are steered by topography due to potential vorticity (f/h) conservation.

is their suggestion that the SO circulation is insensitive to the observed decadal SAM trend?

It is here shown that the zonal wind stress over the path of the ACC is a useful metric to study SO circulation, and that its variability is well explained by the SAM index. With the use of this wind stress metric, and through the development of a proxy for the isopycnal tilt, it is possible to identify a non-zero response in the baroclinic transport of the ACC to changes in the local wind forcing. This conclusion is especially evident in a detailed study of three multi-decadal wind stress trends of the model integration. The model is however found to be overly sensitive to wind stress variability due to a relatively static eddy field, which questions if the amplitude of the baroclinic transport response is overestimated.

Chapter 2

Zonally-integrated models of the Southern Ocean

2.1 Is the Southern Ocean in Sverdrup Balance?

Western boundary currents are an inherent part of the observed large-scale wind-driven ocean gyres. The physics that govern these gyres is mainly explained by the Sverdrup balance (Pedlosky, 1996),

$$\beta \int_{\eta_B}^{0} v \, \mathrm{d}z = \boldsymbol{k} \cdot \nabla \times \left(\frac{\boldsymbol{\tau}_S}{\rho_0} \right), \tag{2.1}$$

which states an approximate balance between the surface wind stress curl and the meridional advection of planetary vorticity in the ocean column below the Ekman layer. Here $\beta = \partial f / \partial y$ and $\boldsymbol{\tau}_S$ is the surface wind stress, and other variables are as presented in the introduction. This vorticity balance is expected to hold in the interior of the ocean for the large-scale flow, where frictional effects, inertia and local acceleration can be ignored, and the circulation does not interact with the bottom at $z = \eta_B$.

The wind stress shear at the top of the ocean results in divergence and convergence of the Ekman current in the Ekman layer, which drives upwelling and downwelling, respectively. Vortex tube stretching and compression of the water column below the Ekman layer takes place due to this mechanical forcing, and in order to conserve potential vorticity, the water column is advected either poleward or equatorward to gain or lose planetary vorticity. For example, in the interior of the subtropical North Atlantic, the wind stress shear is positive, the Ekman layer is convergent and leads to a net equatorward transport of water - the so-called Sverdrup transport.

Continuity necessitates a return flow to form a closed gyre circulation, and this happen to take place at the western boundary of the basin, where the assumptions Sverdrup balance rest upon break down. Here the governing vorticity balance instead promotes a swift boundary current, where friction generates planetary vorticity and the water returns, and balance the Sverdrup transport. Thus a continental barrier has to exist in order to permit friction and setup a closed gyre circulation.

If one views the ACC as a pure zonal phenomenon, confined to the latitude band coinciding with the Drake Passage, there is no meridional boundary to support a western boundary current in the upper ocean, and applying Sverdrup balance is thus prohibited. This view has led to a group of zonally-integrated theories, that attempts to explain the physics of the ACC without the use of Sverdrup balance, and where the transport of the ACC happens to depend on the zonal wind stress magnitude τ^x. An example of such a theory is presented in the classical paper by Johnson and Bryden (1989), which departures in the zonally-integrated zonal momentum balance and a simple eddy closure. They suggest that the transport of the ACC is a function of the square root of the zonal wind stress within the Drake Passage latitude band, and not its curl, as in Sverdrup theory.

Stommel (1957), however, suggested early on that Sverdrup theory might have some relevance to the SO, by noting that the ACC departures from pure zonality. Right after the transit through the Drake Passage, the ACC is observed to turn northward and hug the east coast of South America, until it confluence with the Brazil current, and is deflected eastward again (figure 1.4). Consequently there is a small southward component to the flow of the ACC throughout its circumpolar travel, that ensures the current reconnects at its return to the Drake Passage. The ACC thus escapes the open Drake Passage latitude band, when it flows north of Cape Horn[1] into a region of the SO where Sverdrup balance applies.

Stommel's suggestion is that the poleward Sverdrup transport set by the wind stress curl at the latitude of Cape Horn supplies the ACC, and that the ACC at the east coast of South America constitutes the western boundary current, which transports water back northward. Viewed this way, the ACC is not a unique zonal phenomenon, but a part of an elongated gyre, and its driving force is the wind stress curl at the northern boundary of the Drake passage latitude band, rather than the wind stress magnitude within the band, as in the theory posed by Johnson and Bryden (1989). Stommel does however not account for the flow through the Drake Passage, which he also denotes as

[1]The southern tip of South America

"*Something of a mystery*".

A comprehensive study by Gent et al. (2001) tested both the theory by Stommel (1957) and Johnson and Bryden (1989) using a coarse resolution ocean GCM with parameterized eddies. Through several wind- and buoyancy forcing experiments, they conclude that neither of these theories satisfactory explain what sets the circumpolar transport at the Drake Passage.

If it is the zonally-integrated poleward Sverdrup transport at the Cape Horn latitude that sets the transport of the ACC, the same amount of water must return northward at the western boundary of southern South America. However, in the model, this is not always the case, as only a part of the ACC veers northward after transit through the Drake Passage. This is particularly evident from a set of wind forcing experiments, where only the wind stress magnitude is increased, and not its curl.

When the model is forced with a wind field that is to mimic present day conditions, the entire model ACC is observed to deflect northward after the Drake Passage transit, and the circumpolar transport (134 Sv) approximates the Sverdrup transport (147 Sv). With the increased wind stress, however, the Drake Passage transport increases dramatically to 241 Sv, but the Sverdrup transport remains essentially the same, and only a part of the ACC is deflected northward. Moreover, analysis of the vorticity budget reveals that the Sverdrup balance does not hold, because topography and eddies influence the circulation substantially.

The model by Johnson and Bryden (1989) performs well in the forcing experiments where only the wind stress magnitude changes, but fails to capture the effect from the buoyancy forcing, simply because it is not built into their analytical model. That is, their model does not tell the entire story, but has relevance to the wind-forced part of the circulation.

It thus appears that both the zonally-integrated theory and Stommel's view rely on assumptions and simplifications that do not completely fit the physics of the ACC, and therefore cannot be expected to fully explain its dynamics. Despite this conclusion, both school of thoughts still appear in the literature of today, and are frequently used as a fundament to present more sophisticated zonally-integrated models (Marshall and Radko, 2003), or hypotheses that unite the two branches (Nadeau and Straub, 2009, 2012). Here we review the assumptions and consequences of assuming pure zonality in the SO, which shed light on the necessarity of eddies in equilibrating the ACC, and how these influence the response of the SO circulation to wind stress changes.

2.2 On the application of the pure-zonal-flow assumption

If one assumes that the ACC is zonally symmetric, and applies a closed zonal integral to the zonal component of the vertically-integrated momentum equation, the balance

$$\oint \mathrm{d}x \left[\underbrace{\int_{\eta_B}^{\eta_S} \frac{\partial (uv)}{\partial y} \, \mathrm{d}z}_{A} + \underbrace{\frac{1}{\rho_0} \delta p_B \frac{\partial \eta_B}{\partial x}}_{B} + \underbrace{\frac{1}{\rho_0} \tau_B^x}_{C} = \underbrace{\frac{1}{\rho_0} \tau_S^x}_{D} \right] \tag{2.2}$$

arises, which can be considered a useful description of the governing dynamics for a flow in a zonal channel on a rotating sphere (see appendix A for the full derivation). It states that the zonal momentum transferred by the surface zonal winds to the ocean (D) is either fluxed laterally away from the ACC (A) or dissipated by bottom form drag (B) or by bottom friction (C). The Coriolis term vanishes due to continuity, and the zonal integral of the vertically-integrated pressure gradient is jettisoned, because it is not possible to sustain a net zonal pressure gradient in the open Drake Passage latitude band.

If one imagine a flat-bottomed ocean ($\eta_B(x, y) = \text{const.}$), the bottom form drag term (B) drops out and the meridional divergence of the meridional flux of zonal momentum and bottom friction balance the momentum input by the winds. As noted by Johnson and Bryden (1989), the observed magnitude of the meridional momentum flux is too small to balance the zonal momentum input by the winds alone, if the transport of the ACC is to fit observations. This is also supported by observations of eddy fluxes from autonomous floats (Gille, 2003).

The other potential candidate, the bottom stress, is normally parameterized with an analog to molecular diffusion,

$$\tau_B^x = \rho_0 A_v \frac{\partial u}{\partial z}, \tag{2.3}$$

where A_v is the turbulent viscosity parameter. In principle it is possible to have an ACC that is equilibrated by bottom friction alone, but using a theoretical measure of the vertical shear of the zonal velocity field, Munk and Palmén (1951) show that if the bottom stress is to balance the wind stress, it requires a viscosity much larger than

observed. Moreover, if the bottom friction is assumed to scale like

$$\tau_{\text{Friction}} \sim \frac{\rho_0 A_v U}{d} \sim d\rho_0 U f, \tag{2.4}$$

where $d = \sqrt{A_v/f}$ is the characteristic depth of the bottom Ekman layer (Holton, 2004) and U is a characteristic velocity, and the bottom form drag scales like

$$\tau_{\text{Form}} = \delta p_B \frac{\partial \eta_B}{\partial x} \sim \eta_B \rho_0 U f \tag{2.5}$$

with the aid of geostrophy, such that

$$\frac{\tau_{\text{Friction}}}{\tau_{\text{Form}}} \sim \frac{d}{\eta_B}, \tag{2.6}$$

the bottom form drag is expected to dominate the bottom friction, as long as the the bottom topography η_B is larger than the thickness of the Ekman layer d (Vallis, 2006). With a typical Ekman layer depth of tens of meters, and topographic obstacles encountered by the fronts of hundreds to thousands of meters (figure 1.4), it is expected that the bottom form drag outcompetes the bottom friction by at least an order of magnitude.

The zonally-integrated zonal momentum balance (2.2) is thus well approximated by the balance

$$\oint \mathrm{d}x \left[\delta p_B \frac{\partial \eta_B}{\partial x} \approx \tau_S^x \right], \tag{2.7}$$

and the main sink of momentum is the bottom form drag, as also emphasized by Johnson and Bryden (1989). Bottom form drag is basically an exchange of momentum with the solid Earth. Upstream of an obstacle, with $\partial \eta_B / \partial x > 0$, the flow will converge and raise the sea surface height (SSH), and hence increase the bottom pressure δp_B. Downstream, where $\partial \eta_B / \partial x < 0$, the flow will diverge and lower the bottom pressure, producing a zonal pressure gradient across the obstable. This pressure difference faciliates the removal of the zonal momentum gained by the surface winds.

2.3 The two limits of the Southern Ocean circulation

A fundamental assumption about the interior ocean is that it approximately evolves adiabatically (Gent and McWilliams, 1990). That is, a water parcel conserves its density

by flowing along isopycnal surfaces, and the volume of water between any two isopycnal surfaces remains constant. Mathematically speaking, the material derivative of the density field in isopycnal coordinates is zero,

$$\frac{D\rho}{Dt} = \frac{\partial \rho}{\partial t} + \boldsymbol{u} \cdot \nabla_\rho \rho + Q \frac{\partial \rho}{\partial \rho} = Q = 0, \tag{2.8}$$

where ∇_ρ is the horisontal gradient along surfaces of constant density, and Q is the heat exchange of the water parcel with its surroundings, and is zero following the adiabatic assumption. Hence the properties of a water parcel is set at the surface of the ocean by interaction with the atmosphere and the cryosphere through thermal and fresh-water fluxes.

Combining the interior ocean adiabatic assumption with the fact that the mass of a water parcel δm is a constant,

$$\frac{D\delta m}{Dt} = 0, \tag{2.9}$$

results in the prognostic equation for isopycnal layer thickness,

$$\frac{\partial^2 h}{\partial t \partial \rho} + \nabla_\rho \cdot \left(\frac{\partial h}{\partial \rho} \boldsymbol{u} \right) = 0, \tag{2.10}$$

where $h(x, y, \rho, t)$ is the height of a specific isopycnal surface and $\partial h / \partial \rho$ is the thickness of an isopycnal layer.

This balance is more illuminating if one recognizes that the velocity field is subject to different spatial scales, and expand it using the Eulerian-mean formalism (Holton, 2004). Decomposing the total flow field $\boldsymbol{u}$ into its time-mean large-scale flow $\overline{\boldsymbol{u}}$ and its eddy contribution $\boldsymbol{u}'$, and likewise for the isopycnal height h, the steady-state density field averaged over the eddy-scale is shown to be set by a combination of fluxes that arise from the large-scale velocity field and the eddy field,

$$\nabla_\rho \cdot \left(\frac{\partial \overline{h}}{\partial \rho} \overline{\boldsymbol{u}} + \overline{\frac{\partial h'}{\partial \rho} \boldsymbol{u}'} \right) = \nabla_\rho \cdot \left(\frac{\partial \overline{h}}{\partial \rho} \boldsymbol{u}_{\text{res}} \right) = 0, \tag{2.11}$$

and the resulting flux of the large-scale thickness is more conveniently captured by the residual velocity,

$$\boldsymbol{u}_{\text{res}} = \overline{\boldsymbol{u}} + \frac{\overline{\frac{\partial h'}{\partial \rho} \boldsymbol{u}'}}{\frac{\partial \overline{h}}{\partial \rho}} = \overline{\boldsymbol{u}} + \boldsymbol{u}^*, \tag{2.12}$$

where the last term is denoted the eddy-induced velocity $\boldsymbol{u}^*$. Evidently the spatial-averaged eddies have an impact on the large-scale density structure.

In the important model study by Toggweiler and Samuels (1995), it was only considered how the winds mechanically force the Eulerian-mean velocity field $\overline{\boldsymbol{u}}$ and sets the large-scale density structure of the SO, and did not include the buoyancy fluxes from eddies. Their view thus constitutes the non-eddy limit, where deep upwelling of NADW due to Ekman divergence supports the deep-reaching ACC, which readily feels the bottom, and momentum is dissipated by bottom form drag, as given by equation (2.7). In this view, substantial water mass transformation has to take place at the ocean surface to close the MOC (Hallberg and Gnadadesikan, 2001), and the SO circulation strengthens with increasing wind stress.

In the eddy-limit, however, deep upwelling is not required to balance the surface Ekman drift. Transient mesoscale eddies arise from baroclinic instability (Storch et al., 2012), and these disturb the isopycnal surfaces and generate motion in the meridional. To zeroth order, these eddies are not able to supply any of the equatorward surface Ekman drift, but they flux buoyancy and maintain the density structure of the SO. The first order ageostrophic effect of the eddy-induced velocity field $\boldsymbol{u}^*$, the Stokes drift, allows a net meridional mass transport of a specific density class across the open Drake Passage latitude band, which balances the surface Ekman drift and the geostrophic poleward flow below topography (Hallberg and Gnadadesikan, 2001, 2006). The Stokes drift is a product of the beta-effect, where the wave characteristics of Rossby waves that travel along isopycnal surfaces change, because the governing dispersion relationship is dependent on the Coriolis parameter f.

In the latter limit, a vertical flux of zonal momentum is necessary in order to dissipate the wind-induced momentum at the bottom, and equilibrate the ACC (eq. (2.7)). This vertical flux is facilitated through interfacial form stress. To understand this stress it is useful to imagine a finite-layered stratified ocean. If the uppermost layer is set in motion by the zonal winds, it will accelerate the layer below if a zonal pressure gradient is present, because the layers will exert a force on each other. This layer will subsequently affect the next layer, and so on, until the bottom is met or the zonal pressure gradients cease to exist (Johnson and Bryden, 1989).

The real SO circulation is likely a combination between the two limiting cases (Hallberg and Gnadadesikan, 2006), and some of the surface Ekman transport is balanced by deep upwelling, and some is supplied by eddy-induced flow above topography. In this refined overturning picture, the eddy-induced circulation is able to counteract, or compensate, the Eulerian-mean overturning, and weaken the dynamical constraint imposed by the Drake Passage latitude band. The residual circulation $\boldsymbol{u}_{\text{res}}$, the superposition of the two circulation contributions, is thus the flow to consider in tracer-advection prob-

lems, and is formulated more quantitatively with residual-mean theory. The question of how the SO circulation responds to changes in the wind stress is then a strong function of eddy behavior.

2.4 Residual overturning circulation and eddy compensation

Realizing that eddies play a fundamental role in setting the SO circulation has motivated many theoretical studies, such as the work by Marshall and Radko (2003), that attempts to reveal in what way eddies influence the overturning circulation, and how the circulation strength is dependent on the wind stress.

The eddy-induced meridional streamfunction in physical coordinates is given by

$$\Psi^* = \frac{\overline{v'b'}}{\frac{\partial \bar{b}}{\partial z}}, \tag{2.13}$$

where b is buoyancy, and it is related to the eddy-induced velocity field $\boldsymbol{u}^*$ by (Vallis, 2006)

$$(v^*, w^*) = \left(-\frac{\partial \Psi^*}{\partial z}, \frac{\partial \Psi^*}{\partial y} \right). \tag{2.14}$$

Together with the zonally-averaged zonal momentum balance and the Eulerian-mean formalism ($\Psi = \overline{\Psi} + \Psi^*$), Marshall and Radko (2003) includes this streamfunction of the eddy-induced velocity field to setup a zonally-integrated theory for the ACC that attempts to explain the stratification, and hence the baroclinic transport of the current, in terms of wind stress and buoyancy forcing at the ocean surface. Besides their assumption that the zonally-averaged zonal momentum and buoyancy equation adequately represent the physical system, the key assumptions are:

- The interior ocean is adiabatic and is isolated from the surface buoyancy forcing
- There is a vertically homogenous diabatic ocean mixed layer on top of the ocean interior which is subject to buoyancy forcing
- The equatorward Ekman drift drives the Eulerian-mean overturning circulation i.e. $\overline{\Psi} = -\tau_S^x / f$
- The eddies are transient and stem from baroclinic instability

In their model, baroclinic instability is a function of the isopycnal slope. This instability effect is captured by assuming the eddy buoyancy flux $\overline{v'b'}$ is linearly dependent on the meridional density gradient $-\kappa_{\mathrm{GM}}\frac{\partial\bar{b}}{\partial y}$. This is the Gent and McWilliams (1990) eddy mixing parameterization, where the constant of proportionality κ_{GM} is the thickness diffusivity, that determines the strength of the eddy advection - see section 3.1. Inserting this parameterization in (2.13) gives

$$\Psi^* = \frac{\overline{v'b'}}{\frac{\partial\bar{b}}{\partial z}} = -\kappa_{\mathrm{GM}}\frac{\frac{\partial\bar{b}}{\partial y}}{\frac{\partial\bar{b}}{\partial z}} = \kappa_{\mathrm{GM}} s_\rho \tag{2.15}$$

where s_ρ is the meridional isopycnal slope,

$$s_\rho = -\frac{\partial\bar{b}}{\partial y}\Big/\frac{\partial\bar{b}}{\partial z}. \tag{2.16}$$

It is important to note that the winds drive an equatorward Ekman current in the ocean surface Ekman layer, which in terms of the Eulerian-mean streamfunction is a *positive* (clockwise) circulation. The eddy-induced cell is a *negative* (counter-clockwise) circulation, because the isopycnals in the SO slope poleward. This means the eddy-cell counteracts the mean flow.

Physically, the Ekman overturning raises the isopycnals to the south of the wind stress core and depresses them to the north, as in the view by Toggweiler and Samuels (1995). This increases the available potential energy (APE) of the system. According to their baroclinic instability assumption, increases in the isopycnal slope enhances the eddy activity, which taps the potential energy and attenuates the effect of the winds on the Eulerian-mean overturning. The eddies are said to *compensate* the direct effect of the wind on the overturning, and because the eddy effect in this model is dependent on the isopycnal slope, the circumpolar baroclinic transport is dependent on the eddies too.

Note that in the framework of Marshall and Radko (2003), total eddy compensation ($\Psi_{\mathrm{res}}(\tau^x) = \text{Const.}$) does not imply that the baroclinic circumpolar transport is independent of wind- and buoyancy forcing, and is in fact linearly dependent on the zonal wind stress. If forcing is increased such that the Eulerian-mean overturning increases, the eddy-induced cell strengthens equally in order to compensate, but it comes at the cost of steeper isopycnals, according to the baroclinic instability parameterization. That is, the circumpolar transport increases, albeit less than if the eddy field was independent from the density field.

The scientific question now is whether the eddy parameterization scheme $\overline{v'b'} = -\kappa_{\mathrm{GM}} \frac{\partial \bar{b}}{\partial y}$ is appropriate. Recent eddy-resolving model studies, both with quasi-geostropic models (Hogg and Blundell, 2006; Nadeau and Straub, 2009) and primitive equation models (Munday et al., 2013), show that for sufficiently strong wind forcing, the circumpolar transport of the ACC *saturates*. That is, the transport becomes independent from the wind stress. Such a state of the ACC is not permitted in the model by Marshall and Radko (2003), and it is thus doubtful that this comprehensive analytical model captures all of the relevant physical processes.

Chapter 3

Modelling the Southern Ocean

The lack of observations from the SO forced scientists early on to put their faith into numerical models in order to understand the physics that govern the ocean. With the development of satellite altimetry and theory, it was realized that mesoscale eddies play an important role in the dynamics and thermodynamics of the SO, and an explicit representation of these, or at least the effect of them, in the models is of high priority.

The size of the eddies than spawn from baroclinic instability is mainly dictated by the first baroclinic Rossby deformation radius, which range from 10 to 30 km in the SO (Chelton et al., 1998). Resolving these eddies explicitly, or at least permitting them, requires a model resolution of about $1/2^{\circ}$ or finer (a crude estimate based on various eddy-resolving/permitting model studies of the SO e.g. Ivchenko et al., 1997; Hogg and Blundell, 2006; Hallberg and Gnadadesikan, 2006; Mazloff et al., 2010; Munday et al., 2013). Integrating a full-domain ocean GCM forward on such a fine grid is a computational demanding task.

The Fine Resolution Antarctic Model (FRAM) was one of the first attempts to model the SO eddies explicitly (Ivchenko et al., 1997). The domain of the model spans the entire southern hemisphere south of 24°S and is gridded by $1/4^{\circ}$ in latitude and $1/2^{\circ}$ in longitude. With this model setup, it took three years of computation to produce six years of model output (Rintoul and Garabato, 2013). The accomplishment was though remarkable, showing both the frontal structure of the ACC and confirming that eddies are important agents in transporting momentum in the vertical.

Another noteworthy model is the Southern Ocean State Estimate (SOSE), documented in Mazloff et al. (2010), released approximately two decades after the production of the FRAM. This model spans the same domain, but is running at a slightly finer resolution of $1/6^{\circ}$. SOSE assimilates all contemporary observations, using the adjoint,

to produce a present day state estimate of the SO that is consistent with both governing dynamics and observational constraints. This constitutes an excellent framework to study the influence of eddies on the SO circulation, but only on a relative short time scale; at time of writing, only an estimate extending from 2005 to 2010 is available.

In contrast, fully coupled climate models are often integrated forward on a model time scale of centuries, or even millennia, to produce climate forecasts or to understand past climate changes (see for example Jochum et al., 2012). Such integrations are not computational feasible on a grid that resolves ocean eddies, and instead the effect of the eddies need be parameterized as function of the available ocean mean-state variables.

According to the physical science basis of the fifth IPCC report (Flato et al., 2013), a common choice is to use the Gent and McWilliams (1990) eddy mixing parameterization (hereafter GM-parameterization), or one of its derivatives, to model isopycnal mixing in the interior ocean in coarse resolution climate models. In short, this closure is obtained by letting the mixing depend on the gradient of the large-scale density field, and the eddy transfer coefficient κ_{GM}, and is normally interpreted as a scheme that introduces eddy buoyancy fluxes as an advection by the eddy-induced velocities, and is similar in effect to the Stokes drift.

It is important that the parameterized eddies mimic the behavior of the explicit eddies, especially in the eddy-rich SO, such that the climate forecasts are physically consistent. Studies, such as Gent et al. (1995) and Gent et al. (2011), have shown that the ocean mean-state is well captured by GCMs that use the GM-parameterization. However, recent work by for example Munday et al. (2013) and Jochum and Eden (2015), have shown that the parameterization scheme have critical shortcomings related to *changes* in the forcing of the ocean, with implications for SO upwelling, the strength of the ACC and the quality of climate forecasts.

3.1 Gent-McWilliams parameterization

Gent and McWilliams (1990) note that coarse resolution ocean models are not able to resolve the isopycnal mixing due to eddies, $\overline{\frac{\partial h'}{\partial \rho}\boldsymbol{u}'}$, which appear as the second term within the parenthesis of the steady-state density balance eq. (2.11), and consequently obtain a wrong steady-state density field. Within the Eulerian mean formalism, they provide a solution to this problem by introducing an extra flux term $\boldsymbol{F}$ that represents

the thickness flux by eddies in the equation for isopycnal thickness (2.10),

$$\frac{\partial^2 h}{\partial t \partial \rho} + \nabla_\rho \cdot \left(\frac{\partial h}{\partial \rho} \boldsymbol{u} \right) + \nabla_\rho \cdot \boldsymbol{F} = 0. \tag{3.1}$$

In order to conserve mass, this correction term leads to diabatic effects, $Q \neq 0$, which conflict with the assumption that mixing occur predominantly along isopycnal surfaces - the adiabatic assumption (see section 2.4). This prompt them to invoke the boundary condition that $\boldsymbol{F} \cdot \hat{\boldsymbol{n}} = 0$, where $\hat{\boldsymbol{n}}$ is the unit vector normal to the domain boundary, to ensure that the domain-integrated ocean remains adiabatic (due to the divergence theorem), even though it is locally diabatic, and hence render it quasi-adiabatic.

In terms of the eddy flux $\boldsymbol{F}$, Gent et al. (1995) show that the eddy-induced velocities in eq. (2.12) become

$$\boldsymbol{u}^* = \frac{\partial \rho}{\partial z} \boldsymbol{F}, \quad w^* = -\boldsymbol{F} \cdot \nabla \rho - Q \left(\frac{\partial \rho}{\partial z} \right)^{-1}, \tag{3.2}$$

such that the eddy mixing is represented as advection by the eddy-induced velocity field. Gent and McWilliams (1990) parameterize the eddy fluxes by

$$\boldsymbol{F} = -\frac{\partial}{\partial \rho} \left(\kappa_{\mathrm{GM}} \nabla_\rho h \right). \tag{3.3}$$

This is a diffusion of isopycnal thickness within a density layer, directed from thick towards thin layer thickness, and κ_{GM} is the thickness diffusivity that determines the strength of the diffusion. Inserting eq. (3.3) in eq. (3.2) the eddy-induced velocities become

$$\boldsymbol{u}^* = -\frac{\partial}{\partial z} \left(\kappa_{\mathrm{GM}} \boldsymbol{L} \right), \quad w^* = \nabla \cdot \left(\kappa_{\mathrm{GM}} \boldsymbol{L} \right) \tag{3.4}$$

where

$$\boldsymbol{L} = -\nabla_2 \rho / \left(\frac{\partial \rho}{\partial z} \right) \tag{3.5}$$

is the large-scale isopycnal slope, and in the meridional plane, these velocities obey the eddy-induced streamfunction (2.15), such that the eddy-induced overturning increases when the large-scale isopycnals steepen.

With $\kappa_{\mathrm{GM}} > 0$, the choice of the parameterization (3.3) mimics two important eddy-processes in the ocean, namely a vertical transport of large-scale momentum, like interfacial form stress, and a domain-averaged depletion of potential energy as expected from baroclinic instability (Gent et al., 1995). As discussed by Gent and McWilliams

(1990), these properties of the parameterization are attractive in a domain-averaged sense, but are not always locally consistent, and possibly the thickness diffusivity κ_{GM} needs to be a function of space and time, and perhaps not even sign-definite. Indeed, Ferreira et al. (2005) does report significant spatial variations. However, neither of the two GM papers elaborate on its functional relationship, and today it is still an open research question to specify κ_{GM}.

One approach to model κ_{GM} is to use the mixing length assumption,

$$\kappa_{\mathrm{GM}} = U_{\mathrm{Eddy}} L_{\mathrm{Eddy}}, \tag{3.6}$$

where U_{Eddy} is a characteristic eddy velocity that transfer paticles over the characteristic length scale L_{Eddy}. Visbeck et al. (1997) draws on theoretical work from the early seventies, and argue that U_{Eddy} is dependent on both the vertical (N) and horizontal stratification (M),

$$U_{\mathrm{Eddy}} = \alpha \frac{M^2}{N} L_{\mathrm{Eddy}}, \tag{3.7}$$

where α is a constant of proportionality. This proposal provides a more sophisticated physically-based estimate of κ_{GM}, that is allowed to vary in both space and time. Alternatively, Eden and Greatbatch (2008) suggests that U_{Eddy} is calculated from the eddy kinetic energy E_{EKE},

$$U_{\mathrm{Eddy}} = \sqrt{E_{\mathrm{EKE}}}, \tag{3.8}$$

which is provided by a prognostic parameterized EKE equation, that is to evolve simultaneously with the other governing equations of the specific numerical model. In both studies, the choice of the characteristic length scale L_{Eddy} is rooted in physical quantities, such as the first baroclinic Rossby deformation radius or the width of the baroclinic zone.

3.2 Quasi-geostrophic model studies and eddy saturation

One way to facilitate the simulation of ocean eddies on a time scale longer than a few decades is that through approximate quasi-geostrophic (QG) models (Pedlosky, 1996). As the name suggests, these models apply to flow in near geostrophic balance, and are subject to a substantial reduction of the complexity of the dynamical equations normally implemented in GCMs. These models allow for baroclinic instability to develope, but

for example do not include thermodynamics, and therefore can not be expected to fully capture all the physical processes that are present in the SO.

Hence, layered high-resolution QG-models are integrated forward efficiently due to their simple nature, which allow the study of explicit eddies, and their interplay with the mean flow. Recognizing the importance of eddies in the SO, Dr. Andrew Hogg and colleagues used a three-layer eddy resolving QG model in a Drake Passage channel domain with realistic topography to understand the role of the eddies (Hogg and Blundell, 2006; Meredith and Hogg, 2006; Hogg et al., 2008; Morrow et al., 2010).

In the limit of low viscosity, the circulation of their model is shown to be subject to a dynamical cycle with a decadal time scale, when forced with a static wind stress profile, that is to mimic the SH westerlies (Hogg and Blundell, 2006).

Initially the winds increase the potential energy of the model ocean by increasing the slope of the isopycnals through Ekman dynamics. This increases the circumpolar transport. At some threshold, the density field becomes baroclinically unstable and eddies spawn, feeding on the potential energy and increases the EKE. Eddies transfer momentum to the bottom while potential energy and circumpolar transport decreases. This transfer facilitates dissipation of energy by bottom form drag, but also increases steering by topography along f/h contours. Topographic steering makes the current meander, which decreases the correlation between the wind stress field and the upper layer velocity, thereby reducing the wind work. This is the primary cause of the cyclic model behavior despite constant wind forcing. When potential energy has decreased to a stable level, the EKE dies off and the current becomes less steered and the cycle starts over.

The time-mean over many such cycles thus confirms the steady-state momentum balance derived in section 2.2, where the bottom form drag balances the wind input of zonal momentum. Moreover, the cycle suggests that the model ACC is subject to threshold behavior, where an upper limit to the isopycnal slope exists, and beyond which the state of the ACC is entirely unstable (Meredith and Hogg, 2006). This is indeed confirmed for a low-frequency wind stress perturbation experiment, where the EKE is seen to increase with increasing wind stress rather than the circumpolar transport (Hogg et al., 2008). This time-mean phenomenon is termed *eddy saturation*, and is also documented in other QG model experiments of the SO (Nadeau and Straub, 2009, 2012).

The question is whether an eddy saturation regime also applies to the observed ACC, and a sustained monitoring of its transport through many decades may be needed in order to answer that question. While such an observation certainly is desireable, it is

also cumbersome, and the questions may be answered more efficiently in the framework of complex and less approximate ocean GCMs.

3.3 Parameterized versus explicit eddies in ocean GCMs

One way to assess the usefulness of the eddy parameterization schemes is to compare a model run at low resolution with parameterized eddies to the same model run, but at eddy-permitting resolution and hence with no parameterized eddies. The model study by Hallberg and Gnadadesikan (2006) conducts exactly such an experiment, and compares how the SO overturning circulation and the circumpolar transport of the ACC changes as function of wind stress given four different model resolutions, varying from coarse (1°) through marginally eddy-permitting (1/2°) to eddy-permitting (1/4° and 1/6°).

They use an isopycnal coordinate ocean model with twenty defined density layers in the interior, realistic topography and a domain that spans the entire southern hemisphere. The model run with 1° resolution uses an eddy parameterization scheme equivalent to the one by Gent and McWilliams (1990) with a space- and time invariant GM coefficient of $\kappa_{\mathrm{GM}} = 1000\,\mathrm{m^2 s^{-1}}$ and the runs with 1/4° and 1/6° resolution form the eddies explicitly. The model run with a 1/2° resolution is run twice: one with parameterized eddies and one with explicit eddies.

For each resolution the model is spun up for 20 years with a fixed wind stress. At the end of this period, the wind stress is perturbed and each specific model run branches into three cases: a case with a 20% decrease in the wind, an unperturbed case and a case with a 20% increase in the wind strength. Holding these perturbations fixed in magnitude, the model is integrated yet another 20 years forward.

A time series of the 1° model run shows that the Drake Passage transport stabilizes quickly around 165 Sv in the spin-up phase. When the increased-wind perturbation is switched on, the transport shows a clear ~ 8 Sv increase, and visa versa with respect to the decreased-wind experiment, suggesting that the system respond approximately linear to the wind stress perturbation.

With explicit resolved eddies, this picture changes. First of all the transport fluctuate around 150 Sv in the 1/6° model run spin-up - the lowest transport out of all four model runs due to an energetic eddy field. Secondly, explicit eddies result in a more variable transport compared to the coarse resolution runs. This result is especially clear from the 1/2° model runs, where the parameterization is found to actually supress variability. Third, and last, the response to the wind perturbations is much less

clear and the model displays a signature of eddy saturation, as also found in the Hogg and Blundell (2006) QG model experiment. This is also evident in the $1/4^\circ$ model run, but becomes less pronounced in the marginally eddy-permitting $1/2^\circ$ simulation.

The upper cell of the SO MOC strenghtens and weakens for increasing and decreasing winds, respectively, independent of resolution. However, the origin of the water that supplies the changes in the northward flowing Ekman drift is quite different. In the 1° model run, most of this water origin from deep upwelling of NADW that enters the SO geostrophically below topography, as also found in the coarse resolution model study by Toggweiler and Samuels (1995). With increasing resolution, some of this water is still supplied from deep upwelling, but a larger fraction of the water origins from eddy-driven mass fluxes above topography. These explicit eddies compensate changes in the Ekman overturning, and the residual overturning changes less to the wind stress perturbation in the fine-resolution experiments compared to the coarse resolution run.

Similar results are found in the model study by Munday et al. (2013) that conduct an exhaustive sensitivity study of the SO circulation to wind stress changes. They use the Massachusetts Institute of Technology (MIT) General Circulation Model (MITgcm) in a domain spanning 20° in longitude and from 60°S to 60°N in latitude, with a re-entrant channel in the southernmost part of the domain. The bottom topography is flat, but with a ridge at the model Drake Passage, sufficiently high to block f/h contours that allows the Johnson and Bryden (1989) momentum balance to govern. This domain, though very idealized, is appealing, because it allows explicit deep water formation in the northern part of the basin, such that the stratification of the model develops explicitly, instead of being imposed by some boundary condition at a domain edge. Furthermore, the computational cost is greatly reduced compared to an entire Earth domain, which makes a robust parameter-space survey possible.

Like the procedure in Hallberg and Gnadadesikan (2006) they run the model at three different resolutions: One run at 2° coarse resolution with the Gent and McWilliams (1990) parameterization (κ_{GM} constant at $1000\,\mathrm{m^2 s^{-1}}$) and two eddy-permitting runs at $1/2^\circ$ and $1/6^\circ$ resolution. The model is forced with a time independent wind stress field that mimics the southern hemisphere westerlies and is zero northward of 30°S. This forcing field is chosen to emphasize the role of the southern hemisphere winds in driving the SO circulation.

The model is integrated sufficiently close to equilibrium for each model resolution and each member of the wind stress magnitude ensemble that varies from 0 to $1\,\mathrm{Nm^{-2}}$. The coarse resolution model setup shows that the Drake Passage transport increases approximately linear to increases in the wind strength. In contrast, the $1/2^\circ$ run satu-

rates at $\sim 0.1\,\mathrm{Nm}^{-2}$ and the $1/6^{\circ}$ run is saturated even with no winds at all. Rather, the energy from the wind work is seen to enter the pool of EKE. That is, the natural variability of the system. For example, this makes the transport vary from $\sim 0\,\mathrm{Sv}$ to as high as $\sim 200\,\mathrm{Sv}$ around the temporal mean transport of $\sim 100\,\mathrm{Sv}$ in the $1/6^{\circ}$ simulation with an extreme wind stress peak of $1.0\,\mathrm{Nm}^{-2}$. The different runs also show that the residual MOC is less sensitive to wind stress changes in the fine-resolution runs compared to the coarse resolution run, just as found in Hallberg and Gnadadesikan (2006).

If one believe that the physics at play in the ocean is better captured by the eddy-resolving model simulations than the eddy-parameterized model runs, These two studies call the Gent and McWilliams (1990) parameterization with const. κ_{GM} into question. While it may be possible to tune the parameter such that the current ocean state in ocean models is correctly represented, the parameterization, and hence the ocean state, will not react correctly to changes in forcing. Specifically, the parameterization does not allow for eddy saturation of the circumpolar transport and does make the residual MOC depend too strongly on the wind stress strength. Conclusively more sophisticated parameterization schemes are needed in order to ensure a correct response of the modelled climate system to forcing scenarios.

Munday et al. (2013) also presents a brief but great discussion of the current state-of-the-art eddy parameterization schemes. One way to simulate a more intense eddy field with increasing winds is to tie the GM coefficient to the isopycnal slope, because this slope is correlated with baroclinic instability, that is the root cause of the transient eddies. This allows for a higher degree of eddy compensation, which for example is shown in the study by Gent and Danabasoglu (2011). They examine the impact of a southern hemisphere wind stress perturbation in the Community Climate System Model version 4 (CCSM4), which uses a κ_{GM} that is dependent on the density field (Danabasoglu and Marshall, 2007).

However, as pointed out, when the coefficient is dependent on the stratification, the model will not eddy saturate, as the thermal wind has to increase in order to generate a stronger eddy field. That is, the modelled circumpolar transport will not react correctly to wind stress perturbations. To solve such problem is important in the context of more accurate climate predictions.

Chapter 4

Methods

4.1 The ocean component of CCSM4

This work utilizes the Community Climate System Model version 4 (CCSM4) to answer the scientific questions outlined in the introduction. It is a GCM with a coupled atmosphere, ocean, land and sea ice component, and is documented in Gent et al. (2011). The ocean component is described in Danabasoglu et al. (2012), and technical details about its dynamical core, the Parallel Ocean Program, is found in Smith and Coauthors (2010).

The ocean model solves the boussinesq-approximated primitive equations on a coarse resolution B-grid, with depth, z, as the vertical coordinate, and the solution is constrained by the boundary conditions of no-normal flow and no-slip. The grid resolution of the ocean component is approximately 1° in longitude and gradually increases in latitude from 0.27° at the equator to about 0.7° at the poles. The vertical is discretized into 60 layers, where the upper layer is 10 m thick and increases monotonically to the deeper layers, which are 250 m thick.

As default CCSM4 uses a refined version of the GM-parameterization for the eddy isopycnal mixing in the interior ocean. In accordance with the brief discussion in section 3.1, κ_{GM} varies in space and time by letting

$$\kappa_{\mathrm{GM}} = \frac{N^2}{N^2_{\mathrm{Ref}}} \kappa_{\mathrm{GM,Ref}}, \tag{4.1}$$

where N^2 is the vertical buoyancy frequency, and is related to the stratification of the ocean. N^2_{Ref} is a reference frequency, and $\kappa_{\mathrm{GM,Ref}}$ is a reference isopycnal thickness diffusivity and is set to $3000\,\mathrm{m^2 s^{-1}}$. This relationship is suggested by Ferreira et al.

(2005), and is based on model output of eddy stresses from the MITgcm constrained to observations i.e. a dynamical consistent state estimate (see the discussion on SOSE in section 3). Thus it does not originate in strict physical reasoning, but rather a fit to observations. Letting κ_{GM} depend on the ocean stratification, instead of keeping it a constant, is found to enhance the cancellation between the Eulerian-mean and the eddy-induced overturning in CCSM4, thereby reducing ocean ventilation (Danabasoglu and Marshall, 2007).

In the control run of CCSM4, where the model is fully-coupled and run with pre-industrial conditions, the steady-state Drake Passage transport is 170 Sv, and exceeds the observed value by more than 30 Sv. This bias arises because the atmosphere component forces the ocean with a too strong zonal wind stress field, and not because the ocean model physics is wrong. Forcing the model with an atmospheric dataset, which closer resembles the observed wind stress field, indeed lowers the transport to 142 Sv - considerably closer to the observed transport (Danabasoglu et al., 2012; Cunningham et al., 2003)

In this dissertation we use the output of one thousand year integration of the fully-coupled model with pre-industrial conditions. This model run was primarily used to study the cause of abrupt climate changes that spawn from the internal variability in the model, and setup and results from this analysis are presented in Kleppin et al. (2015). The run shows three major climate transitions in the North Atlantic region; two transitions from a warm to a cold phase and one opposite event. These transitions are readily seen in time series of annual mean surface temperature at Greenland and annual maximum sea ice concentration in the Labrador Sea, and are initiated by a stochastic change is sea level pressure over the North Atlantic.

4.1.1 Modelling philosophy

Scientists of physical oceanography normally make use of idealized model experiments, when they wish to understand what sets a specific quantity in the ocean. That is, they simplify the ocean system to what they believe represents the fundamental physics, because it faciliates a large ensemble of model runs at fine resolution, that can be run to statistical equilibrium. That makes it possible to survey a large fraction of the parameter space with physics that evolves explicitly. Also, these idealized experiments are normally designed such that the experimentalist is in control of the driving forces, which for example is possible if one looks at an isolated ocean model with prescribed meteorological boundary conditions. This makes it relatively easy to link cause and

effect.

Examples of such idealized sensitivity experiments, where the relationship between wind forcing and SO circulation is in focus, are Hogg and Blundell (2006), Nadeau and Straub (2009) and Munday et al. (2013). These works all investigate an ocean model with some sort of idealized wind forcing, and with either simplified geometry, changed bottom topography or approximated ocean physics.

The study by Hogg and Blundell (2006) run a three-layered QG ocean model in a zonally-periodic SO channel domain, with zonal walls and realistic bottom topography, and the model is forced with a time-independent zonal wind stress profile that has the shape of a jet. Nadeau and Straub (2009) uses a similar setup in a two-layered QG model study, but with flat topography, except for a ridge at the model Drake Passage longitude to generate blocked f/h contours. Munday et al. (2013) uses an ocean GCM in a domain that spans from 60°S to 60°N in latitude, but only 20° in longitude, and with a sill at the open model Drake Passage as the only topography. Again the model is forced with a time-independent wind stress field, that is non-zero in the southern part of the domain only.

The CCSM4 model run in consideration here certainly contrast these model experiments. The model is fully coupled, there is no control of the forcing, the model geometry is complex and the run contains three major climate perturbations - all whistles are blowing at the same time. Moreover, there is only one, though long, quasi-steady-state run to analyze. Certainly it will be harder to pinpoint any change in the system to a specific physical process.

On the other hand, the model is not subject to any severe simplification and no physics is left out. Changes in the forcing of the ocean model arise naturally from internal variability, and the forcing is allowed to respond to changes in the ocean, which imply that feedbacks between the different model components are permitted. For example, Marshall and Connolley (2006) show that SH high latitude winter sea surface temperatures (SST) have an impact on the strength of the SAM, and Hogg et al. (2008) note that these SSTs are influenced by the poleward eddy heat flux in the ocean, which are dependent on the wind stress. This relationship constitutes a feedback mechanism, and deem natural perturbation scenarios in the model run more realistic than the cited idealized model experiments.

Aimed with such arguments, the CCSM4 run constitutes an oppertunity to investigate SO circulation with an alternative approach. Instead of investigating the parameter space, this study focuses on transient responses of the SO circulation to SH wind stress trends that arise from the internal variability in the model. This study thus relies on

statistics, and for a sufficiently long model integration, several internal multi-decadal trends in the SAM will most likely occur.

4.1.2 The memory of the ocean and smoothing of output

In a stratified ocean, wind stress anomalies excite both barotropic and baroclinic Rossby waves (Rintoul and Garabato, 2013). In the region of the ACC, the barotropic waves travel fast and the timescale of the ocean response to local high-frequency wind perturbations is relatively short i.e. on the order of weeks (Mazloff, 2012). The baroclinic signal, in contrast, is slow, and the typical ocean basin adjusts on an interannual timescale (Anderson et al., 1979).

In addition to these characteristic response times, physical processes in the world's ocean, remote to the ACC, that affect the global pycnocline also influence the transport of the ACC. Examples of such processes are deep water formation in the North Atlantic and diapycnal mixing (Gnanadesikan, 1999), and the ACC adjustment timescale to such forcing is decades to centuries (Rintoul and Garabato, 2013). The long memory of the ocean ensures that these remote baroclinic signals are not dissipated before they reach the SO (Allison et al., 2011).

The work by Böning et al. (2008), whos hypothesis is the main inspiration to this study, address changes in the baroclinic transport of the ACC on a multi-decadal timescale, motivated by the sustained trend in the SAM. They do not explicitly compare time series of transport and wind stress anomalies, but investigate differences in property fields between the middle of the 20th century and the present. Hence they do not need to consider the adjusting timescale to baroclinic waves excited by local forcing, as the multi-decadal time period in focus greatly exceeds it. That is, if there is an ocean response to the wind stress trend captured by the SAM, the SO has sufficient time to adjust, setting the influence from the rest of the world's ocean aside.

In contrast, this study is to explicitly compare time series of different wind stress metrics to time series of SO circulation strength, and the ocean response time is thus relevant. However, in order to simplify the study, the following assumptions are made:

1. Despite the interannual ocean response time to local forcing in the SO, it is sensible to compare metrics of wind stress and ocean circulation strength with zero lag.

2. It is possible to extract the response from local wind forcing in the SO circulation metrics.

3. That smoothing the model output with a ten-year running mean is useful, because this study addresses changes on a decadal timescale

It is important to emphasize that this study focus on sustained wind stress anomalies i.e. low-frequency variability. It is thus meaningful to smooth the output, such that the variability in the ocean response that is generated by interannual fluctuations in the wind stress is removed. We expect the baroclinic ocean response to lag the sustained wind stress anomalies by a couple of years, and this is relevant to statistical quantities, as for example the covariance.

The second assumption is valid if the majority of the SO adjusts on a time scale of a decade i.e. it is the local forcing that dominates the full response. The spin-up of a primitive equation model indeed shows that the equilibration exhibit an exponential behavior, and that the majority of the adjustment takes place in the beginning of the model integration (Munday et al., 2013). The e-folding time scale of this adjustment is though closer to a century than to a decade, leaving a substantial part of the adjustment to non-local processes, and it is not expected it is possible to derive a clean and robust relationship between the the wind stress variability and the changes in the density field.

4.1.3 Key ocean circulation diagnostics

To understand how wind forcing is related to the SO circulation, it is nessecary to quantify measures of the circumpolar transport and the MOC, as well as having an idea of the spatial shape of the CCSM4 ACC.

It is common practice to measure the volume transport of the ACC at the Drake Passage (Gent et al., 2001; Nadeau and Straub, 2009; Meredith and Coauthors, 2011). This metric is shown by the black line in figure 4.1 for the model ACC, and is seen to fluctuate around a mean value of $\sim 168\,\mathrm{Sv}$ as expected (Danabasoglu et al., 2012), deviating by approx. $30\,\mathrm{Sv}$ from observations (Cunningham et al., 2003). On a decadal timescale, the greatest changes in transport are seen in the very beginning of the time series and around year 200 and 700, where it changes by as much as $7\,\mathrm{Sv}$ in less than a century.

The MOC is presented in figure 4.2, decomposed into its Eulerian-mean overturning $\overline{\Psi}$ (left panel) and its eddy-induced circulation Ψ^* (right panel), using the GM-parameterization to model the latter. The Eulerian-mean cell shows the circulation that results from Ekman dynamics as function of the wind field that overlies the ocean; upwelling to the south, downwelling to the north and a northward Ekman drift in the surface. Consistent with the theory developed in section 2 and 3, the eddy-induced

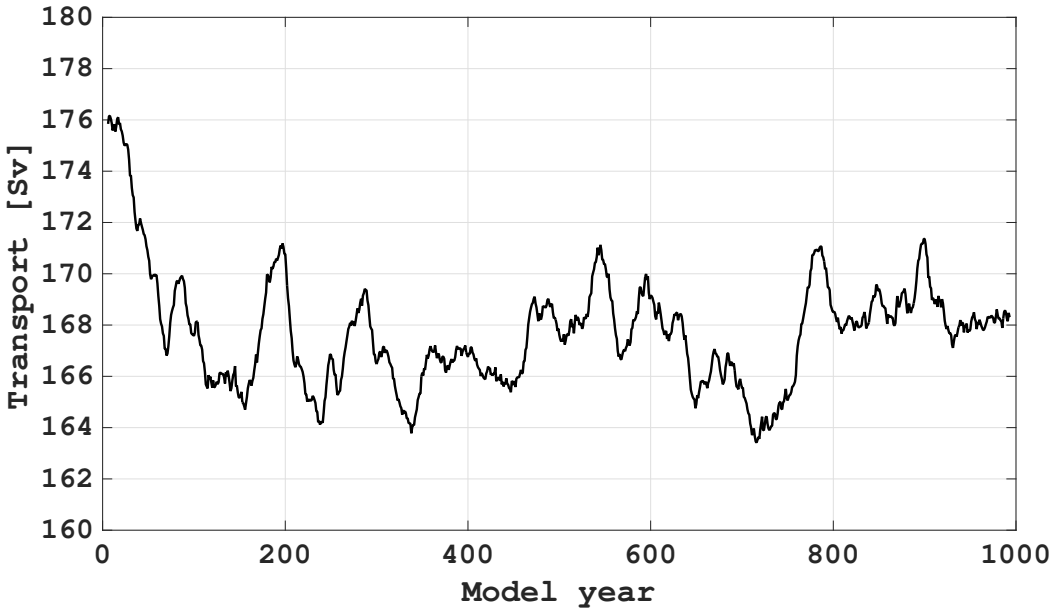

Figure 4.1: The volume transport at the Drake Passage. The units are in Sv ($1\,\mathrm{Sv} \equiv 1 \times 10^6\,\mathrm{m^3 s^{-1}}$). The transport is calculated from one-year means of the zonal velocity field. A ten-year running mean has been applied.

cell is fueled by a conversion of large-scale APE to EKE through baroclinic instability, thereby weakening the slope of the isopycnals. This cell is rotating in the opposite direction to the Eulerian-mean circulation, and the time-mean residual circulation (the sum of the two components) holds an overturning of $\sim 30\,\mathrm{Sv}$.

Figure 4.3 displays the time-mean model ACC, and the reader is encouraged to compare it to figure 1.4, which is equivalent, but based on observations. Both figures agree that the ACC to some extent is steered by topography. For example, both observations and model show that the current should deflect around the Kerguelen and Cambell plateau, and that the flow passes through the gaps in the Pacific ridge. Moreover, it is seen that a branch of the ACC runs along the east coast of South America, before it is deflected eastward at the Brazil current confluence region.

4.1.4 Model drift

Figure 4.4 displays the zonally-averaged potential density field anomaly at $\sim 300\,\mathrm{m}$ depth, which is below the mixed-layer depth in most parts of the SO. It is seen that as time progresses, the waters in the southern part of the domain becomes increasingly dense, and opposite for the northern part. This pattern does not reflect a meridional

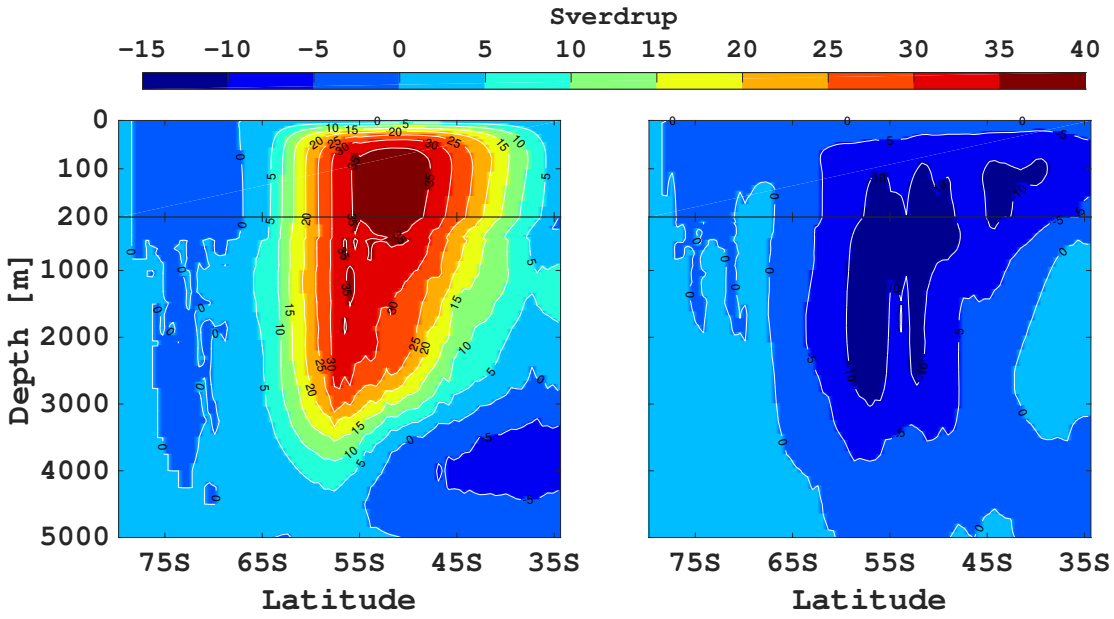

Figure 4.2: The left panel displays the time-mean zonally-averaged Eulerian-mean overturning circulation $\overline{\Psi}$. The right panel displays the time-mean zonally-averaged eddy-induced circulation Ψ^*. Positive values denote clockwise circulation, and opposite for negative values. The sum of the two components results in the residual overturning circulation. The maximum and minimum of these cells, respectively, constitutes the time series of overturning strength.

shift in the density field, as such a change would produce similar anomalies in both the south and in the north. Rather it suggests that heavier water is lifted in the southern part and lighter water subducted to the north, and corresponds to an increase in the meridional tilt of the isopycnals. The change in the tilt in the first 200 years occurs relatively rapid compared to later in the model run, and the field seems closer to thermodynamic equilibrium beyond year 600. This low-frequency change in the density field is accompanied by an increase in the strength of the eddy-induced circulation (black line, figure 4.5), because it is a function of the slope of the large-scale isopycnal (Gent and McWilliams, 1990).

This unexpected model behavior is deemed an artifact of the model run. One of the goals of this dissertation is to understand how changes in wind stress impact the SO density field, and hence the baroclinic transport, but if the signal is dominated by a low-frequency drift, it will complicate analysis.

In order to meet this problem, the first 400 years of the model run is neglected, and the remaining signal is detrended by subtracting a linear least squares fit. This choice is based on the strength of the eddy-induced overturning (figure 4.5), where a change in the magnitude of the trend is evident around year 400. The first 400 years

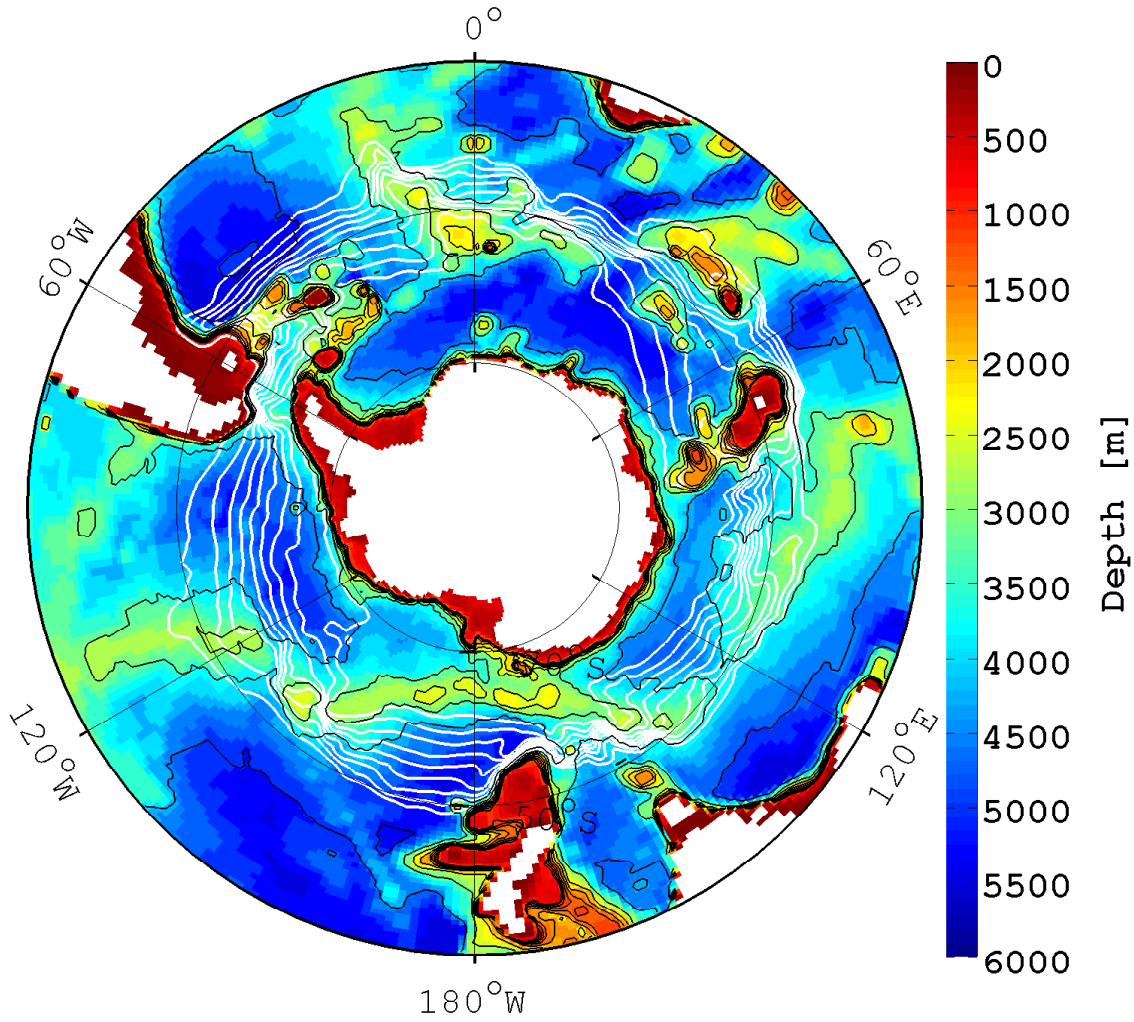

Figure 4.3: Time-mean barotropic streamfunction contours superposed on the CCSM4 bottom topography. The white lines are the streamlines 10 Sv to 170 Sv with an interval of 20 Sv. The black lines are the f/h contours. This figure is the model equivalent to figure 1.4.

(red dash-dotted line) posses a trend that is greater than the mean trend of the entire time series (red solid line), and opposite for the the last 600 years (red dashed line). The drift becomes weaker with time, and it is more appropiate to remove the first part of the time series and detrend the last part with a linear trend, than to detrend and analyze the entire time series.

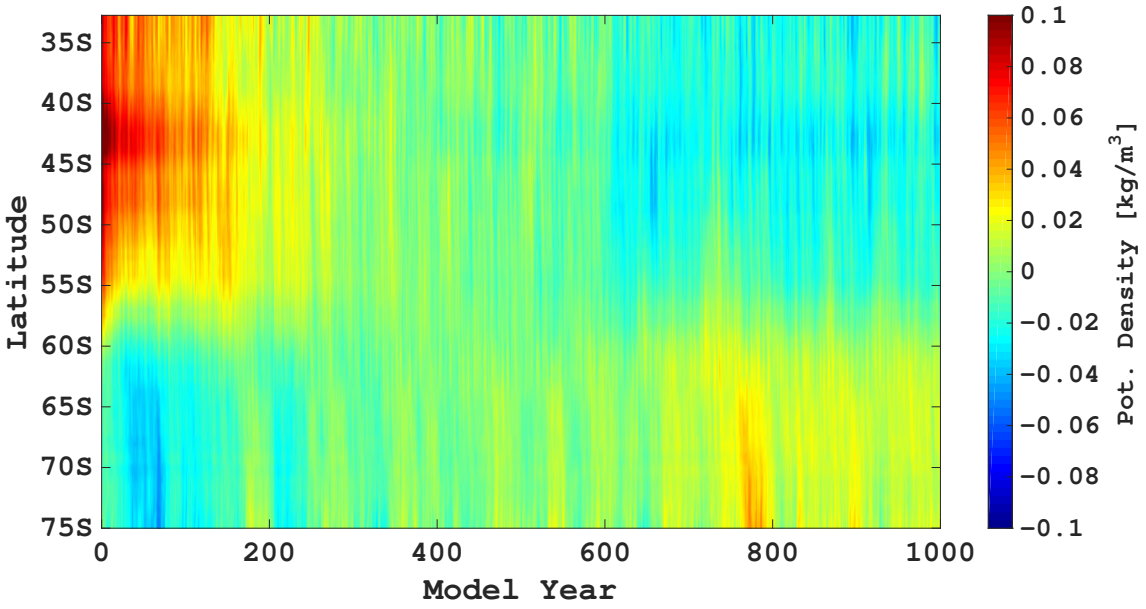

Figure 4.4: The zonal average of the potential density field at $\sim$ 300 m depth, presented in a hovmöller diagram. The 1000 yr temporal mean has been subtracted at each latitude to display the anomaly. The field shows a trend toward steeper isopycnals with time.

4.2 Wind stress metrics

Many studies on the SO circlulation address changes in the wind stress forcing in terms of the SAM (e.g. Böning et al., 2008; Sallée et al., 2008; Morrow et al., 2010; Langlais et al., 2015). Despite that its zonally-symmetric structure is appealing to the quasi-zonal ACC, there is no apriori reason why this mode should capture the relevant variability in the SO wind stress to the circulation. The transport of the ACC is not necessarily equally sensitive to the zonal wind stress at all longitudes (Mazloff, 2012), nor is there a scientific consensus on which metric of the wind stress is relevant (Allison et al., 2010). It is therefore of interest to develope different wind stress metrics, based in physical reasoning, and compare them to the SAM and the SO circulation metrics, to assess whether we expect a change in the circulation given the observed trend in the SAM.

4.2.1 Deriving the SAM through EOF analysis

An instructive approach to the SAM is that through an Empirical Orthogonal Function (EOF) decomposition, and for a great introduction to the topic, see Emery and Thompson (1997). This decomposition is like a principle component analysis, and brings out

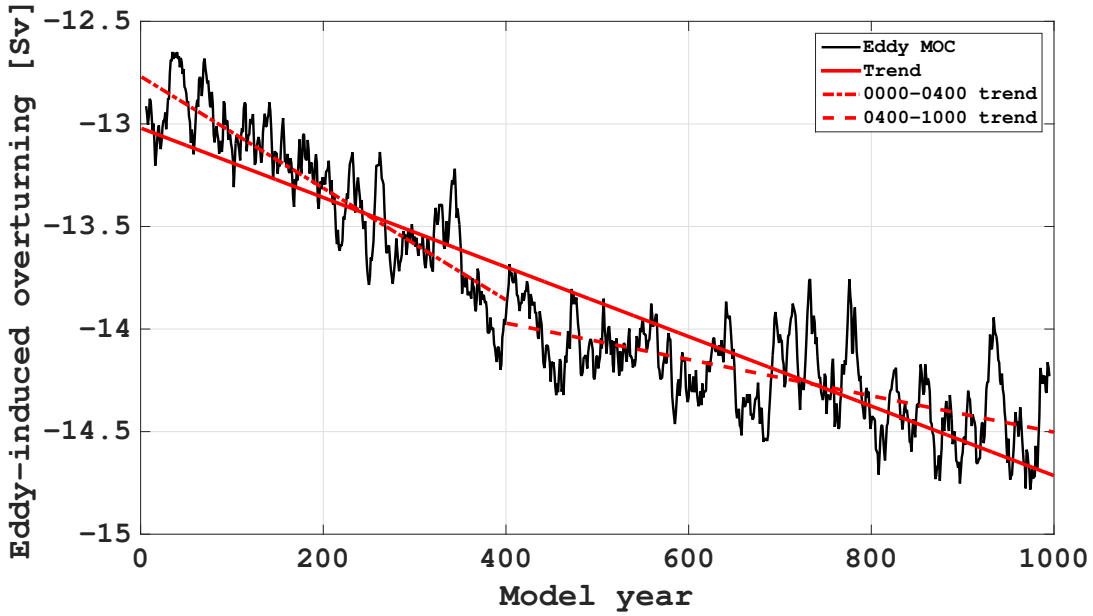

Figure 4.5: The strength of the eddy-induced overturning cell. The black line is the minimum of the eddy overturning cell in the SO (right panel, figure 4.2), calculated from one-year mean stream-function output. The signal has been smoothed by a ten-year running mean. The dash-dotted, the dashed and the solid red lines are a linear least-squares fit to the first 400 years of the time series, the last 600 years of the time series and the entire time series, respectively.

the dominating modes of variability from the time-dependent field. This statistical analysis is thus suitable to look at atmospheric large-scale oscillations like the SAM.

The SAM is often the most dominant mode of variability in different property fields, such as SLP and wind stress (Sallée et al., 2008; Langlais et al., 2015). Here we look at the leading EOF in the zonal wind stress field of the model run.

The first EOF explains about 39% of the variance in the model zonal wind stress (figure 4.6). This EOF features a circumpolar structure, which in many ways is similar to the one found by Langlais et al. (2015), and nicely illustrates how the wind stress pattern is thought to change due to the annular SAM. The mode does however show some asymmetry, and oscillations are stronger above the Pacific Ocean than above the Indian and Atlantic Ocean. The likely cause of this deviation from zonal symmetry is the influence of the El Niño Southern Oscillation, another large-scale oscillation, which too operates in the South Pacific Ocean (Morrow et al., 2010).

This remark illuminates a very important aspect of EOF analysis; An EOF decomposition is a statistical tool, and one can not be sure that the individual EOFs are related to physical modes. Possibly the EOFs are a mixture of more than one physical process, or perhaps not linked to any. In order to understand whether we can ascribe

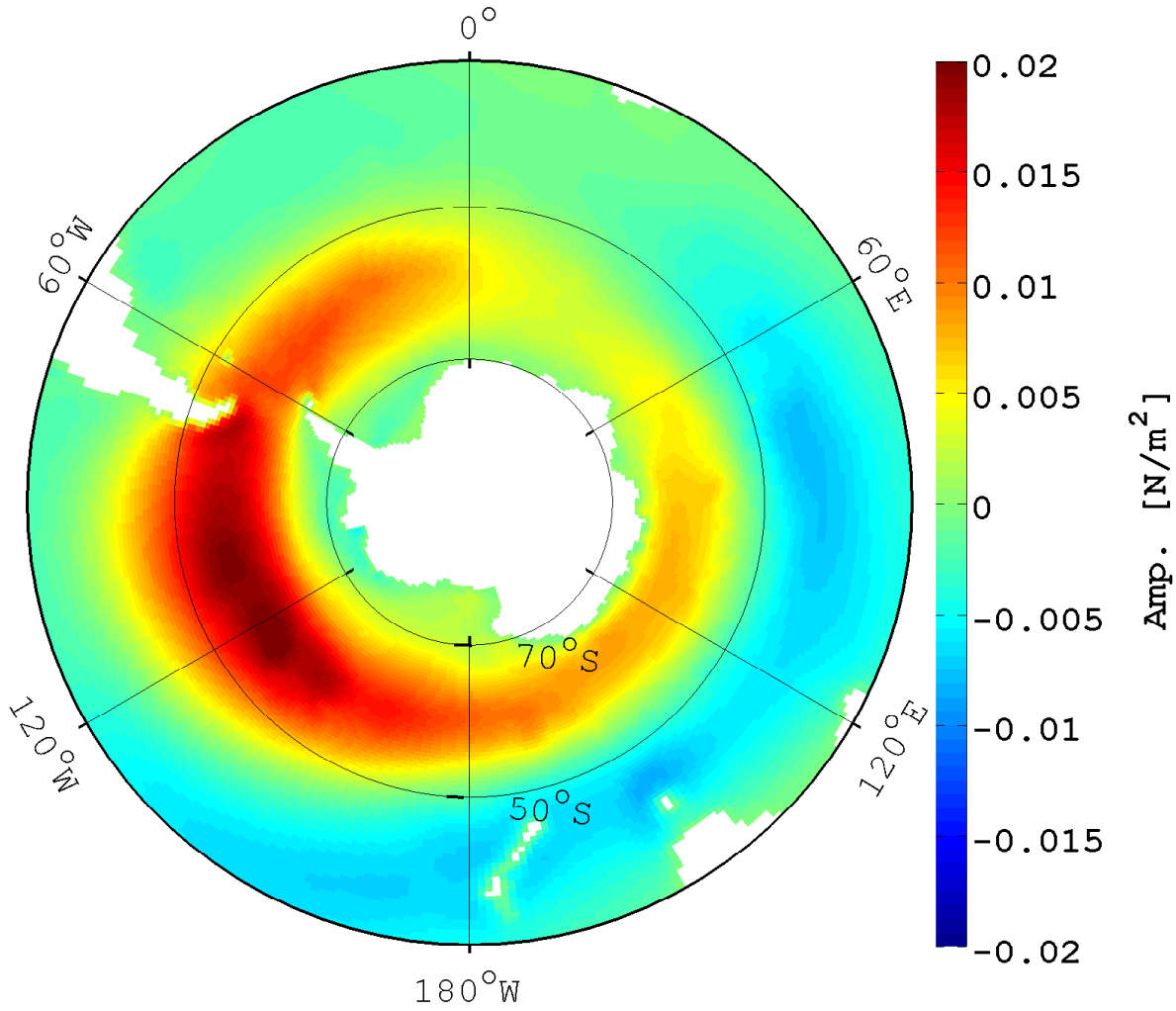

Figure 4.6: The leading empirical orthogonal function (EOF) of the annual mean zonal wind stress field. This function explains about 39% of the variance. The function is annular in structure, but is not entirely zonal symmetric, and the winds stress fluctuate with greater magnitude in the South Pacific Ocean than in the southern sectors of the Atlantic and the Indian Ocean.

any physical meaning to the first EOF, we compare its associated prinicple component (PC1) to the SAM index estimated from the pressure field (see appendix C) in the left panel of figure 4.7.

The two variables clearly correlates ($r = 0.88$, $p < 1\%$), and it is thus meaningful to describe the first EOF as a physical mode, since it is possible to relate it to the oscillations in the meridional atmospheric isobars. The PC1 is henceforth the measure of the amplitude of the wind stress variability captured by the SAM.

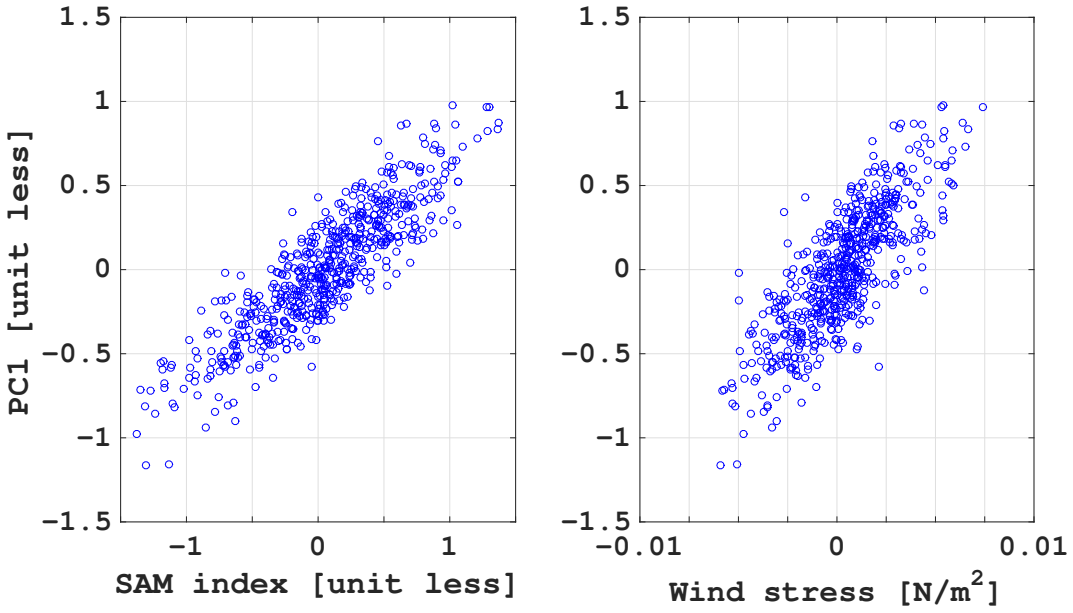

Figure 4.7: The left panel displays the SAM index (see appendix C) against the first principal component of the EOF decomposition. The right panel displays the wind stress over the path of the ACC against the first principal component of the EOF decomposition.

4.2.2 Quantifying measures of the zonal wind stress

Various suggestions of physical meaningful wind stress metrics exist throughout the literature. We choose to departure in the measures summarized in Allison et al. (2010), which include:

1. The zonally-averaged zonal wind stress at the latitude of the northern edge of the Drake Passage.
2. The average zonal wind stress within the Drake Passage latitude band.
3. The maximum of the zonally-averaged zonal wind stress.
4. The mean zonal wind stress over the path of the ACC.

The first measure was suggested by Toggweiler and Samuels (1995) to control the SO upwelling and the Atlantic outflow, and hence the strength of the MOC and slope of the isopycnals. However, their coarse resolution model study did not include eddies, and the model was subject to an unphysical momentum balance. Also, they did not relate it directly to the circumpolar transport. With the advances in coarse resolution modelling since the publication of the paper, this study re-evaluates the importance of this measure.

The second measure is the one that is commonly employed in the zonally-integrated theories (Johnson and Bryden, 1989; Marshall and Radko, 2003), where the flow of the ACC is confined to the Drake Passage latitude band.

The third measure is important, because it is not averaged within a time-independent domain, like the two previous estimates. This estimate follow any potential meridional excursions of the wind stress core, and assesses whether the ACC is sensitive to the wind stress strength itself, instead of being sensitive to wind stress in a specific region.

The fourth measure origins from an analytical model (Gnanadesikan, 1999), and is based on the idea that it is the integrated northward Ekman transport over the path of the ACC that is relevant to the isopycnal slope,

$$\tau_{ACC}(t) = \frac{f_0}{L_x L_y} \oint \int_{\text{south}}^{\text{north}} \frac{\tau^x(x,y,t)}{f(y)} \, \mathrm{d}A, \tag{4.2}$$

where $\tau^x(x,y,t)$ is the zonal wind stress field and the area integral is bounded by the extent of the circumpolar streamlines. L_x and L_y are the mean length and width of the ACC, respectively, and the product of the two will here be given by the actual area covered by the ACC.

In order to obtain τ_{ACC}, a time-dependent mask of the ACC, based on its circumpolar streamlines, is needed. This mask, multiplied onto the zonal wind stress field, is shown in figure 4.8 for the very first year of the model output. The mask is found by setting the region outside streamlines to zero. Superposed on the figure are the two extreme streamlines (the bold black lines) of the Barotropic StreamFunction (BSF) for that particular model output year, specifically streamline 2 Sv and 171 Sv, and it is seen that these follow the border of the mask.

It is quite clear that the four derived wind metrics (figure 4.9) all show similar fluctuation patterns, but posses different means and variances. The area-weighted mean of the zonal wind stress within the Drake Passage latitude band has the lowest mean of the four measures, but is very energetic compared to the other estimates, and therefore displays the greatest changes in the wind stress. In contrast, the wind stress over the ACC path has a relatively small variance with fluctuations around $0.01\,\mathrm{N/m^2}$, and a mean considerably greater than the previous estimate, implying small relative changes.

It is not surprising that the fluctuation pattern is similar between all four metrics, because all estimates undergo some sort of zonal averaging. In Allison et al. (2010) they consider how these wind quantities differ as function of meridional shifts in the zonal wind stress core, and find significant changes when the core is moved by more than ten degrees of latitude. For example, moving the wind stress core to the north, while

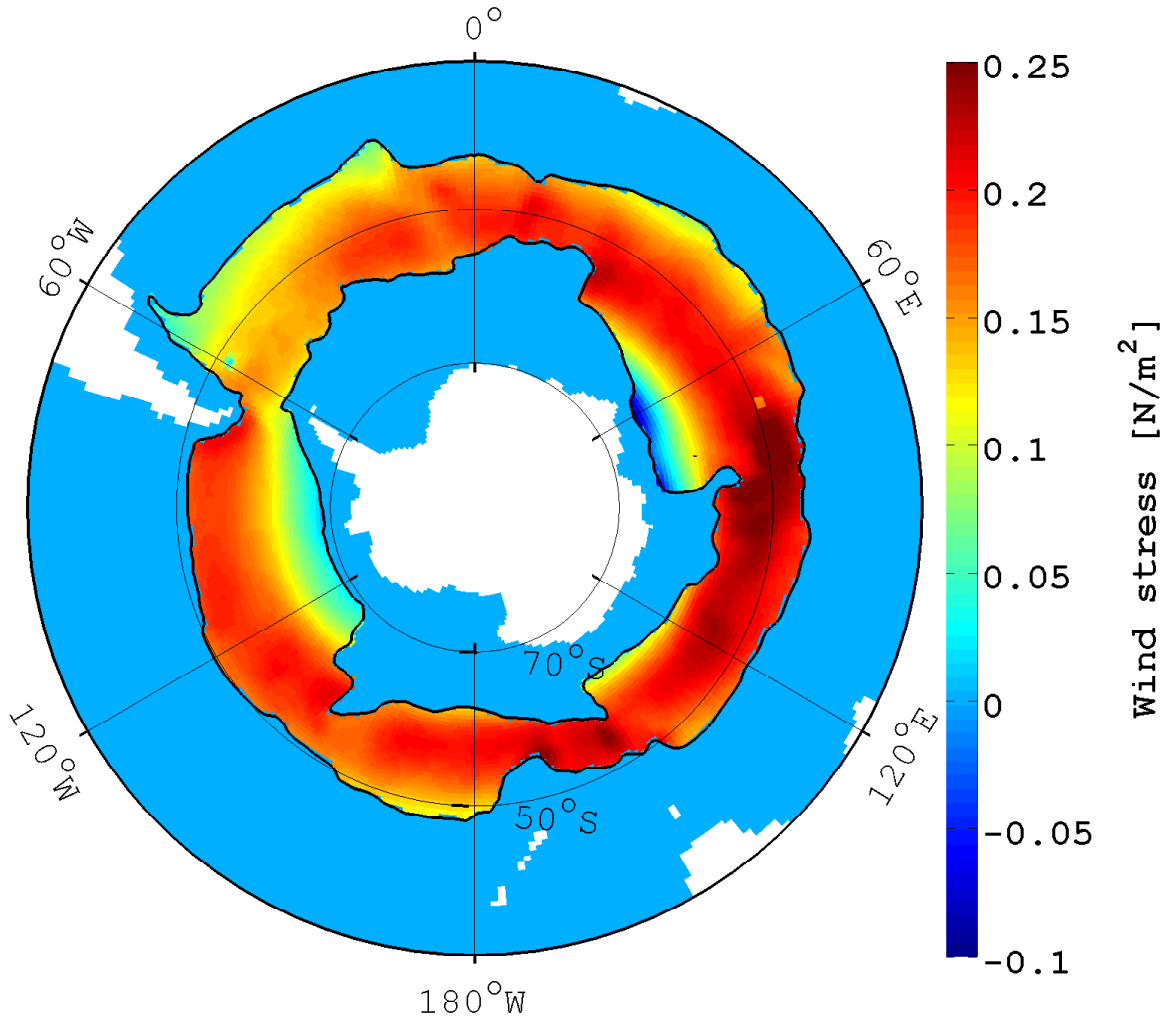

Figure 4.8: An ocean mask multiplied onto the zonal wind stress field, here displayed for model year 1. The boundaries of the ocean mask is defined from the extreme streamlines of the ACC barotropic streamfunction i.e. the outermost circumpolar streamlines. These streamlines are time-dependent, and so the mask varies in time. The extreme streamlines for this particular year are here shown by bold black solid lines, and denote streamlines 2 Sv and 171 Sv.

preserving its magnitude, will change the area-weighted mean within the Drake Passage latitude band, but leave the maximum of the zonally-averaged zonal wind stress core intact. Given the similarities in the wind stress metrics, the wind stress core of the model run does not move much in the meridional.

Recognizing the close relationship between the wind stress time series, the wind stress over the ACC path is chosen to represent the forcing quantities, and is compared to the PC1 of the EOF decomposition (right panel, figure 4.7). It is seen that the

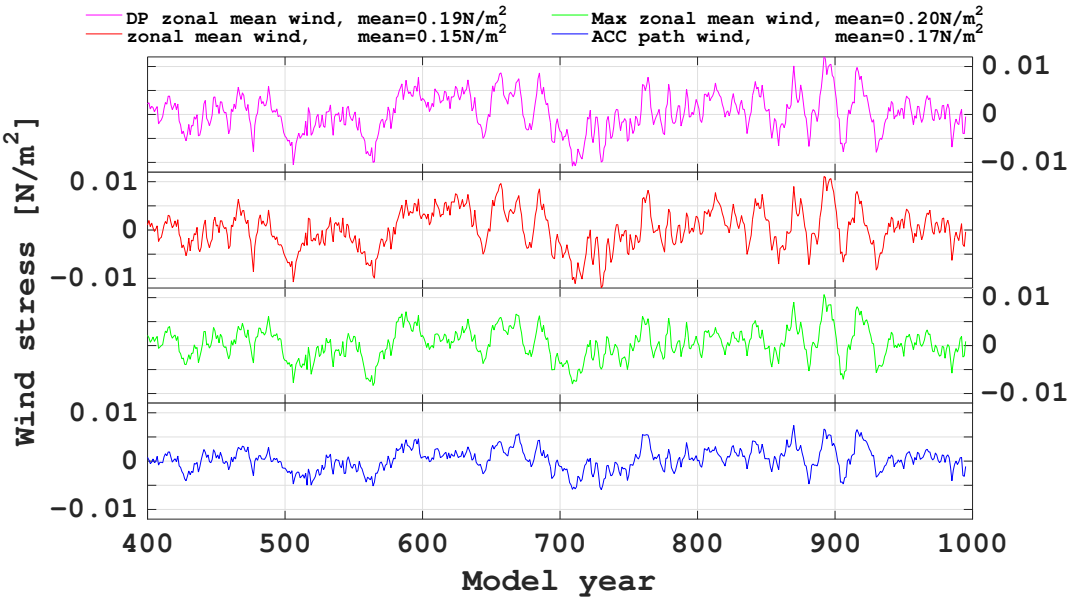

Figure 4.9: Four different metrics of the wind stress at the surface of the SO. The blue line is the wind stress over the ACC path, which is the mean of the zonal wind stress within a time-dependent ocean mask (See figure 4.8). The green line is the maximum of the zonally-averaged zonal wind stress jet. The red line is the area-weighted mean zonal wind stress within the Drake Passage latitude band. The magenta line is the zonally-averaged zonal wind stress at the latitude of the northern boundary of the Drake Passage. All metrics are calculated from one-year means of the zonal wind stress field, and smoothed by a ten-year running mean. The plot shows the anomalies and the corresponding means are found in the figure legend.

fluctuations in the wind stress agree well with the fluctuations in the SAM. Thus, if one of the wind stress metrics prove to be relevant, it is meaningful to relate changes in the SO circulation to the atmospheric variability captured by the SAM.

4.2.3 A comparison to observations

Multi-decadal trends are visible in the wind stress metrics (figure 4.9). In order to clarify whether these trends in the zonal wind stress are significant and mimics the observed present day trend, we compare the three strongest 50 yr model trends to the ERA-40 reanalysis product, produced by the European Centre for Medium-Range Weather Forecasts (ECMWF). The SAM index derived from this reanalysis has proven to compare well to the observed SAM (Marshall, 2003).

The ERA40 reanalysis runs from 1958 to 2001, and the SO wind stress derived from this product is shown in figure C.2 in appendix C. The wind stress is subject to a positive trend, and suggests a statistically significant increase in the wind stress of

$0.030 \pm 0.007 \mathrm{N/m^2}$ (table 4.1) during a 50 yr period.

The three strongest 50 yr model wind stress trends are depicted in figure C.3 in appendix C. The 50 yr trends are not all statistically significant at the 5% level, and are only one half to one third the strength of the present day trend (table 4.1). The strongest 50 yr wind stress trend in the model run is the one between year 665 and 714, and shows a significant decrease of $0.016 \pm 0.005 \mathrm{N/m^2}$ during a 50 yr time span, approximately half the magnitude of the present day trend.

This analysis thus shows that the CCSM4 model run possesses two statistically significant wind stress trends at the 5% level. This enable us to investigate the hypothesis by Böning et al. (2008), who state that the SO circulation is insensitive to low-frequency wind stress changes, though only for wind stress trends that are weaker than the one which is presently observed. If these wind stress trends do not produce a significant response in the baroclinic ACC transport, the study ends inconclusive, because the possibility that stronger trends are able to generate an ocean response remains to be tested. If however the trends do result in a response, it is meaningful to discuss the relevance of the hypothesis.

Table 4.1: The ERA40 and CCSM4 50 yr trends and their associated uncertainties. The trends and uncertainties are in units of $\mathrm{N/m^2/50yr}$. The uncertainty is quantified by the standard deviation, and it is assumed that the variance in the wind stress is the same for each annual mean realization of the wind stress within each of the three 50 yr segments. The significance of the correlation is approached with a t-test, and is deemed significant at the 5% level i.e. that there is a 5% chance that the null-hypothesis is correct, the null-hypothesis being that the variables are uncorrelated.

Trend #	50 yr trend	σ	significance
ERA40	+0.030	0.007	$p < 1\%$
CCSM 0462-0511	−0.011	0.006	$p < 10\%$
CCSM 0551-0600	+0.013	0.005	$p < 5\%$
CCSM 0665-0714	−0.016	0.005	$p < 1\%$

4.3 The components of the circumpolar transport

4.3.1 Baroclinic potential energy

One way to quantify the baroclinic transport of the ACC is through the Baroclinic Potential Energy (BPE)(Borowski et al., 2002). It is a measure of the potential energy associated with the structure of the density field, and is closely related to, but not the same as, the APE (Lorenz, 1955). In its conceptual form, the APE provides a measure

of how much energy it is possible to release from the density field by rearranging it adiabatically to its state of lowest potential energy, and an increase in isopycnal slope increases the APE. The BPE, in contrast, is more of an absolute measure of the potential energy, and it is its associated gradient which is a relevant measure of the isopycnal slope. That is, in an ocean system in a state of lowest potential energy, the APE and the gradient of the BPE are both zero.

The BPE originates from the vertically-integrated momentum equation (A.6) by manipulating the vertical integral of the deviation pressure field using the hydrostatic balance (A.4) and the relationship $(\nabla_2 p)_B - g\delta\rho_B \nabla_2 \eta_B = \nabla_2 p_B$ (See appendix B). In this form, the steady-state vertically-integrated momentum equation appear as

$$f\boldsymbol{k}\times\boldsymbol{U} = \underbrace{-\nabla_2\chi - \frac{g\eta_B}{\rho_0}\delta\rho_B\nabla_2\eta_B}_{\text{A}} + \underbrace{\frac{\eta_B}{\rho_0}(\nabla_2 p)_B}_{\text{B}} + \underbrace{\frac{1}{\rho_0}(\boldsymbol{\tau}_S - \boldsymbol{\tau}_B)}_{\text{C}} + \boldsymbol{G} \tag{4.3}$$

where

$$\boldsymbol{U} = (U, V) = \int_{\eta_B}^{0} \boldsymbol{u}\,\mathrm{d}z \quad \text{and} \qquad \boldsymbol{G} = \int_{\eta_B}^{0} (\boldsymbol{v}\cdot\nabla)\boldsymbol{u}\,\mathrm{d}z \tag{4.4}$$

are the depth-integrated horizontal velocity field and the depth-integrated non-linear terms, respectively. $\delta\rho_B = \delta\rho(x, y, z = \eta_B)$ is the bottom density field and all other terms are defined as previously. The terms in the A-bracket of eq. (4.3) are responsible for the baroclinic transport, the term in the B-bracket is the barotropic transport (bottom geostrophic velocity field multiplied with the height of the ocean column), and the terms in the C-bracket are the transports associated with the Ekman layers. χ is the BPE and given by

$$\chi = \frac{g}{\rho_0}\int_{\eta_B}^{0} z\delta\rho\,\mathrm{d}z, \tag{4.5}$$

and is solely determined from the density field.

The study by Böning et al. (2008) uses the BPE metric to discuss changes in the baroclinic transport of the ACC. They focus on the upper 2000 m of the water column, which is not influenced directly by the bottom topography. In that case $\nabla_2\eta_B = 0$ and the baroclinic zonal transport is given by the meridional gradient of the BPE field i.e.

$$U_{\text{baroclinic}} = -\frac{1}{f}\frac{\partial\chi}{\partial y}. \tag{4.6}$$

To obtain the baroclinic transport we estimate the BPE field given by eq. (4.5). The BPE field from each annual mean potential density field is calculated to a depth of

$\sim 2075\,\mathrm{m}$ (model layer #46) with a reference density of $\rho_0 = 1028\,\mathrm{kg/m^3}$.

The temporal mean BPE field (figure 4.10) is close to uniform in the zonal direction and with a strong meridional gradient, holding a signature of the ACC. This is expected since the deviation density field $\delta\rho = \rho - \rho_0$ becomes increasingly negative in the upper part of the ocean column as equator is approached. The choice of ρ_0 is abitrary, because it does not influence the gradient of the field, and is here chosen such that the field is everywhere positive, which is physically meaningful. Kerguelen- and Cambell Plateau, as well as a few regions in proximity of the Scotia Ridge[1], all show up in the field as areas of low BPE, because the depth of the ocean does not extend to 2000 m and hence restricts the lower bound of the integral.

4.3.2 Averaging along streamlines and conservation of transport

Results are obtained for the streamline-averaged circulation instead of the zonally-averaged. Despite the near zonality of the ACC, the flow is subject to a small southward drift throughout most of the currents voyage around Antarctica, and in addition, the flow meanders and is steered by topography (figure 1.4 and 4.3). Due to the vertical extent of the ACC to the bottom, contours of the the barotropic streamfunction follow the Lagrangian streamlines closely, and averaging along these streamlines give a better representation of the SO structure.

In the following, all figures based on streamline-averaged fields are averaged along streamline 5 Sv through 160 Sv with a 5 Sv interval to ensure that the entire core of the ACC is covered in the analysis. The temporal mean position of these streamlines are superposed on figure 4.10 shown by the black solid lines.

Moreover, the integrated baroclinic transport (meridional integral of eq. (4.6)) is obtained between streamline 5 Sv and 160 Sv, meaning that the total transport (the sum of the baroclinic and barotropic transport) is conserved between the bounds, by construction. To use streamlines as bounds for the ACC is desireable in that it keeps the analysis away from external influence from for example the subpolar gyres and the Agulhas Retroflection. The trade-off is that the integrated baroclinic transport do not capture transport changes of the entire ACC, but rather quantify the amount of baroclinic transport in the conserved 155 Sv volume transport. That is, if the barotropic and baroclinic transport components respond equally to forcing, the time series of the integrated baroclinic transport will reduce to a constant.

[1] Kerguelen and Cambell plateau are the large bathymetry features at 70°E and 170°E, respectively (see figure 1.4). The Scotia Ridge is directly to the east of the Drake Passage.

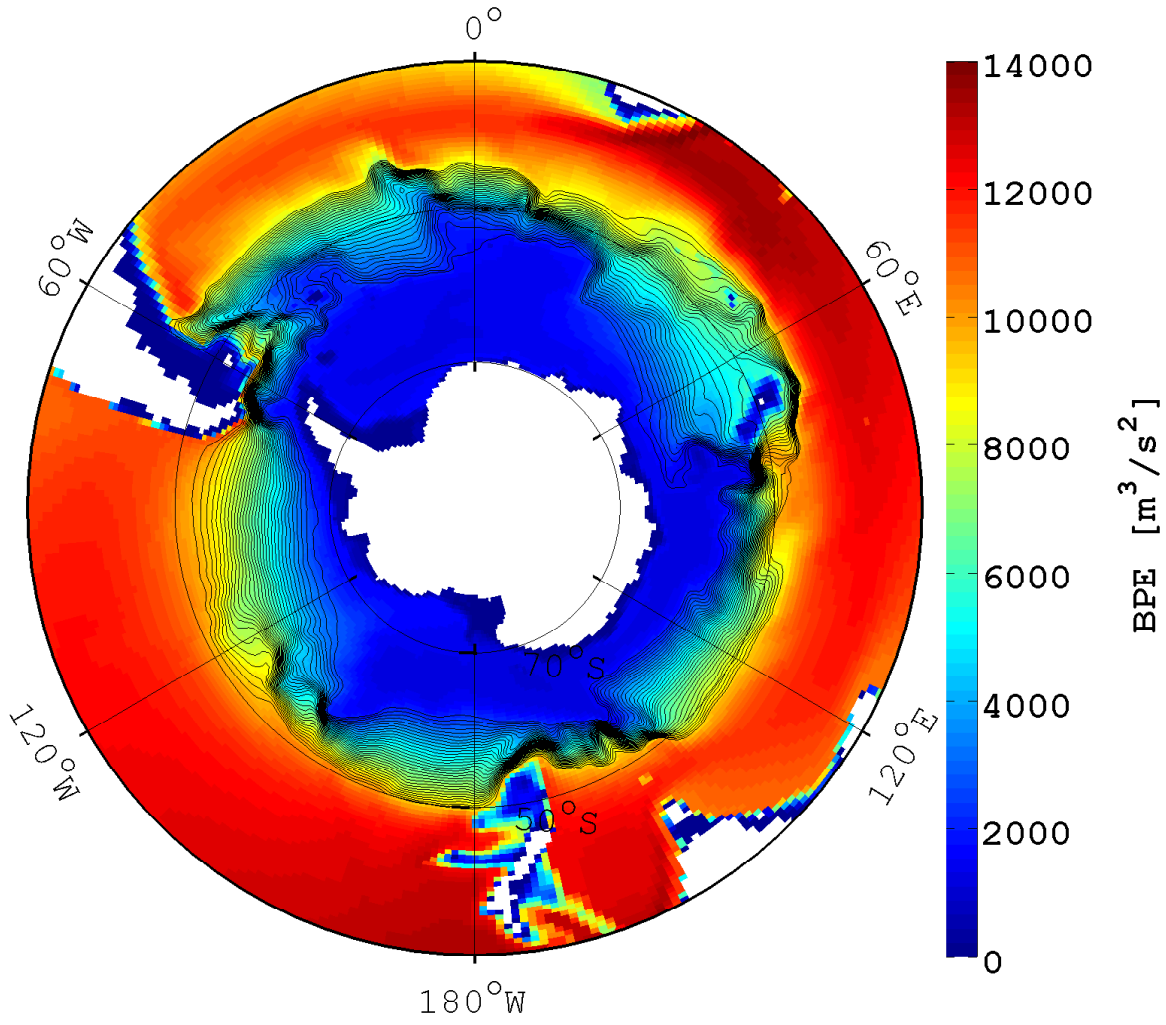

Figure 4.10: The temporal mean baroclinic potential energy (BPE) field calculated from the annual mean potential density field. The field is given by eq. (4.5). The reference density is here chosen to $\rho_0 = 1028\,\mathrm{kg/m^3}$ and the lower integration bound is chosen to $\sim 2075\,\mathrm{m}$, consistent with Böning et al. (2008). The black lines are the temporal mean streamlines, obtained from the barotropic streamfunction, from 5 Sv to 160 Sv with an interval of 5 Sv. Comparing streamlines with the BPE field reveals a strong signature of the ACC in the BPE field.

4.3.3 A simple two-box estimate

Inspired by the method in Langlais et al. (2015) we obtain an additional measure of the baroclinic transport as well as an estimate of the barotropic transport. The rationale is to validate the more complex BPE estimate of the baroclinic transport with a simpler estimate, and to enable a comparison between the wind metrics and the barotropic component.

At a specific longitude the zonal velocity field is divided into two boxes in the vertical, with a user-defined separation boundary. The barotropic component is then given as the mean transport in the lower box multiplied by the water column depth. The baroclinic component is the difference in transport between the two boxes; simply the shear.

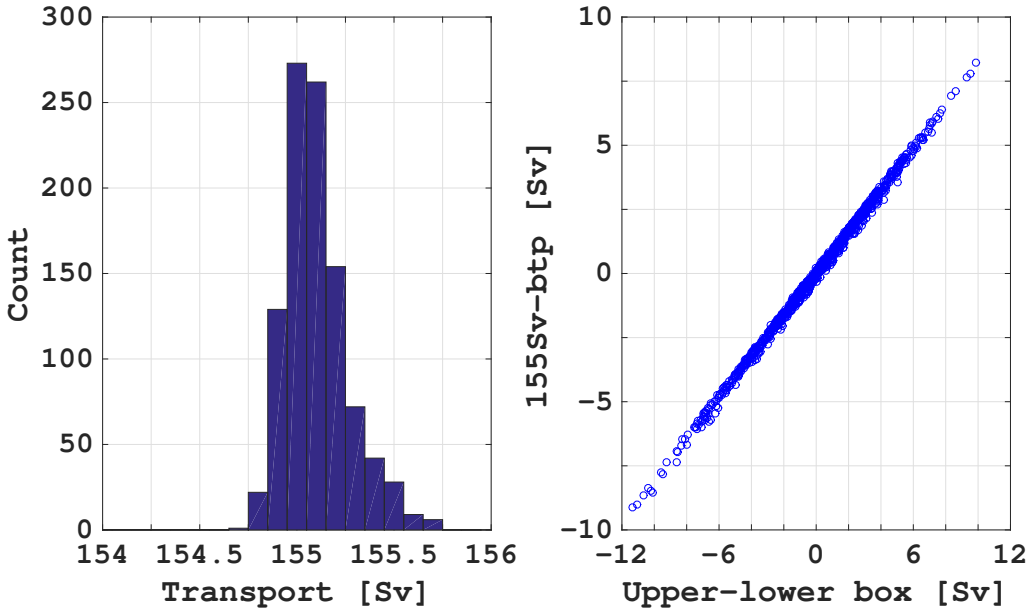

Figure 4.11: The left panel displays the distribution of the volume transport between streamline 5 Sv and 160 Sv for the entire model run by integrating the zonal velocity field using a linear interpolation to estimate the exact location of the streamlines on the coarse model grid. The right panel displays the correlation between the shear estimate (box 2-box 1) and subtracting the barotropic transport component from the conserved 155 Sv volume transport. The analysis is conducted at 275°E.

The two transport components are not overly sensitive to the choice of separation boundary, but the decomposition has to take place away from complex topography that interupts the vertical structure of the ACC (Langlais et al., 2015). The boundary of separation is here picked at the same depth level as for the BPE estimate ($\sim$ 2075 m, model layer #46). The bounds on the meridional integral is kept at streamline 5 Sv and 160 Sv, as are also used in calculating the integrated baroclinic response from the BPE field.

Because the model output is coarse in resolution, these bounds must be interpolated to ensure a conserved volume transport. A simple linear interpolation is used, as it proves to conserve the transport to a satisfactory degree (left panel, figure 4.11), and that the shear estimate is essentially the same as subtracting the barotropic signal from

the conserved 155 Sv transport (right panel, figure 4.11).

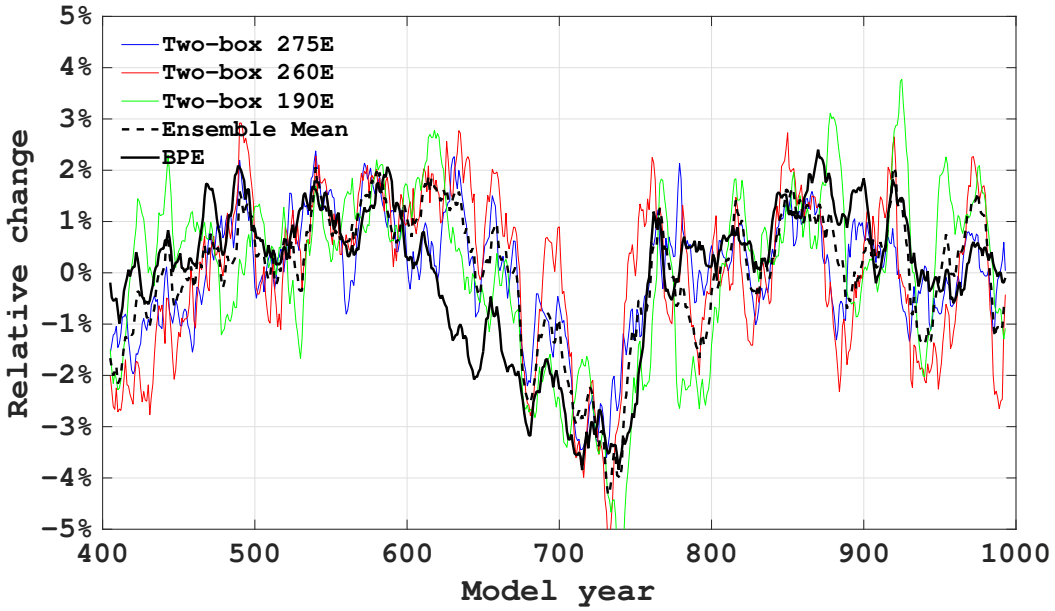

Figure 4.12: The ACC baroclinic transport pr. degree latitude of the ACC estimated using two different methods. The blue, red and green curves are obtained using a simple two-box estimate at long. 275°E, 260°E and 190°E respectively. The black dashed line is the mean of these three estimates. The solid black line is the estimate from the gradient of the BPE field. All the curves are normalized by their temporal means and smoothed by a ten-year running mean.

The decomposition is carried out at three different longitudes, namely at 190°E, 260°E and 275°E, where bottom topography is relatively flat. The ACC baroclinic transport pr. degree latitude at these three longitudes (the blue, red and green line, figure 4.12) show an overall similar structure, but is also subject to disagreement. This suggests that the density field does not vary zonally symmetric, but is properly also a product of the simplicity of the decomposition. Comparing these transport estimates to the one obtained from the streamline-averaged BPE field (solid black line, figure 4.12) leads to the same conclusion, but does not constitute a fair comparison, because the BPE signal represents a circumpolar average, whereas the others do not. The mean of the three two-box esimates (dashed black line, figure 4.12) also yield a closer agreement to the BPE-based signal (black solid line), with a correlation coefficient of 0.75.

Chapter 5

Results

Before the results are presented, the reader is reminded of the goals of the dissertation, and the scientific questions are here restated:

1. Which measure of the SO wind stress is useful to understand variability in the SO circulation?

2. Given the eddy parameterization, how well does this climate model eddy compensate and saturate with respect to the results from eddy-resolving models?

3. How does the barotropic ACC component respond to the SO wind stress?

4. By applying their method to the model output, how robust is the suggestion by Böning et al. (2008) that the SO circulation is insensitive to the observed decadal SAM trend?

The results that aid the answers follow below in a chronological order.

Firstly, the set of wind stress metrics (figure 4.9) is compared to the circulation measures (section 4.1.3), in order to determine which of the four is the most relevant to the SO circulation. Secondly, the influence of the parameterized eddies in closing the MOC, outlined in sections 2.3 and 2.4, is assessed by examining the overturning cells (figure 4.2), to understand the responsiveness of the model circulation to local wind stress forcing. Thirdly, the derived time series of the baroclinic and barotropic transport, provided by the two decompositions of the ACC transport, and described in detail in section 4.3, are presented. Finally, the wind stress metric that is identified as being the most relevant is compared to the baroclinic transport estimate, and the inference by Böning et al. (2008) is evaluated.

5.1 Testing the wind stress metrics

Figure 5.1 compares the Drake Passage transport (figure 4.1) to the wind stress metrics (figure 4.9). Although some agreement between the phase of the transport (black line in each of the four panels) and the wind stress variables (colored lines) is present, a simple robust relationship between the transport and any of the four wind stress metrics is not evident. In general the comparison is subject to large discrepancies, as clearly seen in the latter half of the 7th model century, and in the notable absence of transport responses to several of the wind stress anomalies during the last 200 yrs of the integration. Conclusively, based on these four wind stress metrics, the variability in the Drake Passage transport does not appear to be a function of the local wind stress alone.

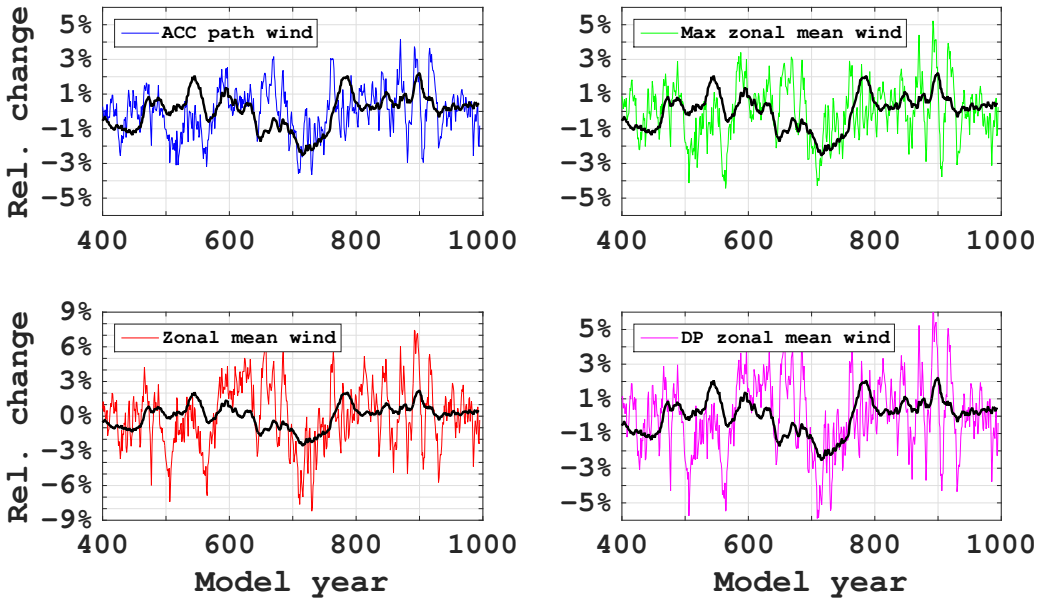

Figure 5.1: The annual-mean Drake Passage transport (black line), shown in figure 4.1, compared to the four wind stress metrics (figure 4.9). The signals have been smoothed by a ten-year running mean and divided by their respective 600 yr temporal means. The upper left panel displays the comparison to the zonal wind stress over the path of the ACC, the upper right to the maximum of the zonally-averaged zonal wind stress, the lower left to the area-weighted mean zonal wind stress within the Drake Passage latitude band and the lower right to the zonally-averaged zonal wind stress at the latitude of the Southern tip of South America.

The characteristic amplitude of the fluctuations in the wind stress over the ACC path (1-2%, upper left panel) generally scales well to that of the Drake Passage transport, but events where the wind stress greatly exceeds the change in transport also occur. The other three wind stress metrics generally exhibit stronger variability than

the circumpolar transport, which is most pronounced for the mean of the zonal wind stress in the Drake Passage latitude band (lower left panel), where the wind stress varies by up to 7% of its mean value ($0.15\,\mathrm{N/m^2}$).

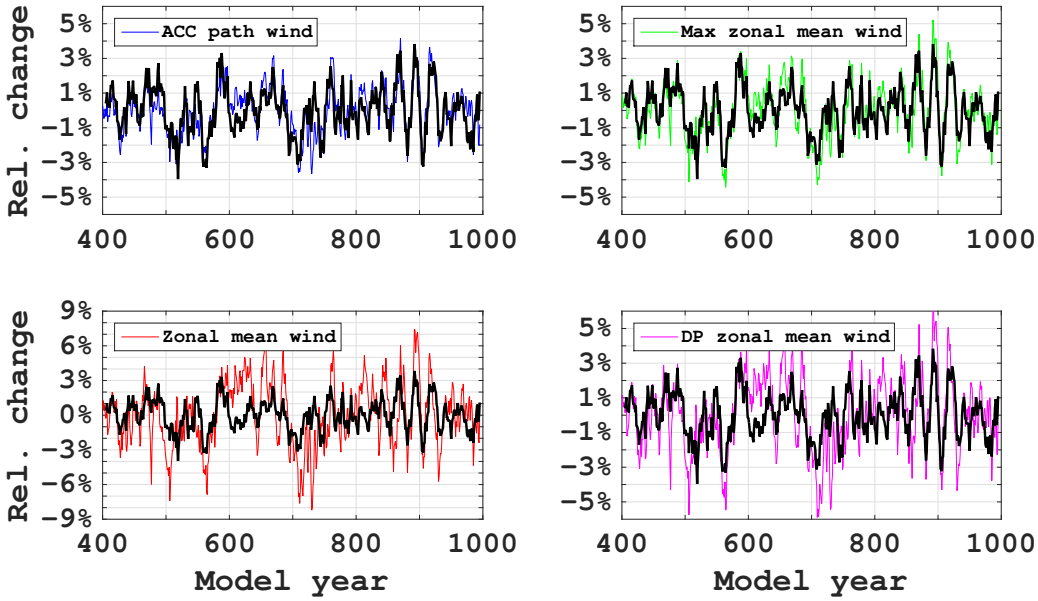

Figure 5.2: The annual-mean strength of the Eulerian-mean overturning cell (black line) compared to the four wind stress metrics (figure 4.9). The signals have been smoothed by a ten-year running mean and divided by their respective 600 yr temporal means. The upper left panel displays the comparison to the zonal wind stress over the path of the ACC, the upper right to the maximum of the zonally-averaged zonal wind stress, the lower left to the area-weighted mean zonal wind stress within the Drake Passage latitude band and the lower right to the zonally-averaged zonal wind stress at the latitude of the Southern tip of South America.

The comparison between the wind stress metrics and the strength of the Eulerian-mean overturning (figure 5.2) displays strong covariance. This is not a surprise, because the Eulerian-mean overturning is governed by Ekman dynamics, and the transport of the equatorward surface Ekman layer is linearly proportional to the zonal wind stress. It is the zonal wind stress integrated over the ACC path ($r = 0.80$, upper left panel) and the maximum of the wind stress core ($r = 0.88$, upper right panel) that provides the closest match to the overturning strength in terms of relative change. The other two metrics in general possess too strong variability, which is most clearly seen from the zonal wind stress within the Drake Passage latitude band ($= 0.55$, lower left panel).

The strength of the eddy-induced (figure 5.3) circulation does not agree as closely with the wind stress metrics as did the Eulerian-mean overturning, but it does appear that a stronger wind stress tends to drive a stronger eddy field. This behavior is also

expected from the inspection of figure 5.2, where the strong link between the wind stress and the directly wind-driven overturning exerts strong control on the large-scale isopycnal slope and hence the model eddy fluxes (Gent and McWilliams, 1990). The relative changes in the eddy-induced overturning are however smaller than those in the Eulerian-mean overturning. Then, given their respective time-mean overturning strengths of $\sim -14\,\mathrm{Sv}$ and $\sim 39\,\mathrm{Sv}$ (figure 4.2), it is possible to conclude without further discussion that the eddies are not able to completely balance the variability in the mean-flow, and that the residual overturning must possess a finite sensitivity to the wind stress variability.

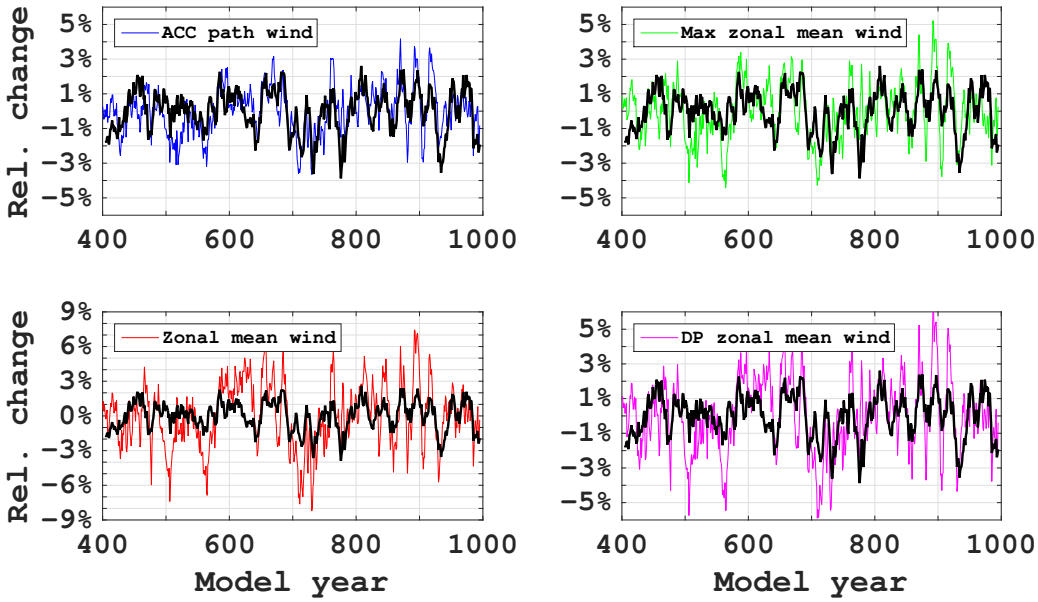

Figure 5.3: The annual-mean strength of the eddy-induced overturning cell (black line) compared to the four wind stress metrics (figure 4.9). The signals have been smoothed by a ten-year running mean and divided by their respective 600 yr temporal means. The upper left panel displays the comparison to the zonal wind stress over the path of the ACC, the upper right to the maximum of the zonally-averaged zonal wind stress, the lower left to the area-weighted mean zonal wind stress within the Drake Passage latitude band and the lower right to the zonally-averaged zonal wind stress at the latitude of the Southern tip of South America.

The relative change in the wind stress over the ACC path ($r = -0.56$, upper left panel) scales with the eddy-induced overturning to some extent, whereas the other three metrics fluctuate more strongly. What functional relationship $\Psi^*(\tau^x)$ to expect in this coarse resolution model setup is however not entirely clear, but certainly depends on the specification of the thickness diffusivity κ_{GM}.

5.2 Eddy sensitivity

The circulation that is set by the parameterized transient eddies potentially compensates a fraction of the directly wind-driven overturning in the model. The degree of this compensating effect determines the sensitivity of the residual MOC to changes in the wind stress magnitude. Eddy compensation is a time-mean concept (Hallberg and Gnadadesikan, 2006; Gent and Danabasoglu, 2011; Munday et al., 2013; Jochum and Eden, 2015), and is normally displayed by plotting the mean residual overturning strength of several equilibrated model runs against their corresponding mean wind stress magnitude. This analysis is not possible in the present study, because we deal with one quasi-equilibrated model run only, and because we are not in control of the driving wind force in the coupled configuration of CCSM4.

In the time-mean of this run, the Eulerian and eddy-induced overturning is $\sim 39\,\mathrm{Sv}$ and $\sim -14\,\mathrm{Sv}$, respectively (figure 4.2), and the residual overturning is $\sim 30\,\mathrm{Sv}$, such that the eddies compensates about $9\,\mathrm{Sv}$ of the Eulerian-mean overturning at the time-mean wind stress magnitude. To obtain the sensitivity of the residual MOC to wind stress variability, we will address the degree to which the instantaneous fluctuations in the eddy-induced circulation compensate the variability in the Eulerian-mean overturning as function of the wind stress.

A scatter plot of the transport anomalies from the Eulerian-mean overturning $\overline{\Psi}$ against the eddy-induced overturning Ψ^* (circular marks, figure 5.4) reveals that the former is subject to more variability than the latter, as also concluded from figure 5.2 and 5.3. The figure also shows that the Eulerian-mean circulation is strongly correlated with the wind stress over the path of the ACC (color of the circular marks). This correlation is likewise present, but less pronounced, when the eddy-induced circulation is subject to the comparison.

The overturning components are weakly anti-correlated ($r = -0.39$). That is, it is slightly more probable that an anomalously strong Eulerian-mean overturning (clockwise circulation, positive anomaly on the horizontal axis) is paired with an anomalously strong eddy-induced circulation (counter-clockwise circulation, negative anomaly on the vertical axis) than it is paired with a weakening of the eddy-induced circulation (positive anomaly on the vertical axis). However, least-squares fitting the pairs with a straight line (dashed line, figure 5.4) to assess the time-mean effect, shows that there is a small certain tendency (-0.12 ± 0.01) that both cells strengthen at the same time.

Figure 5.5 shows the anomaly of the strength of the residual overturning $\Psi_{\mathrm{Res}} = \overline{\Psi} + \Psi^*$ as function of the strength of the Eulerian overturning $\overline{\Psi}$, and these are strongly

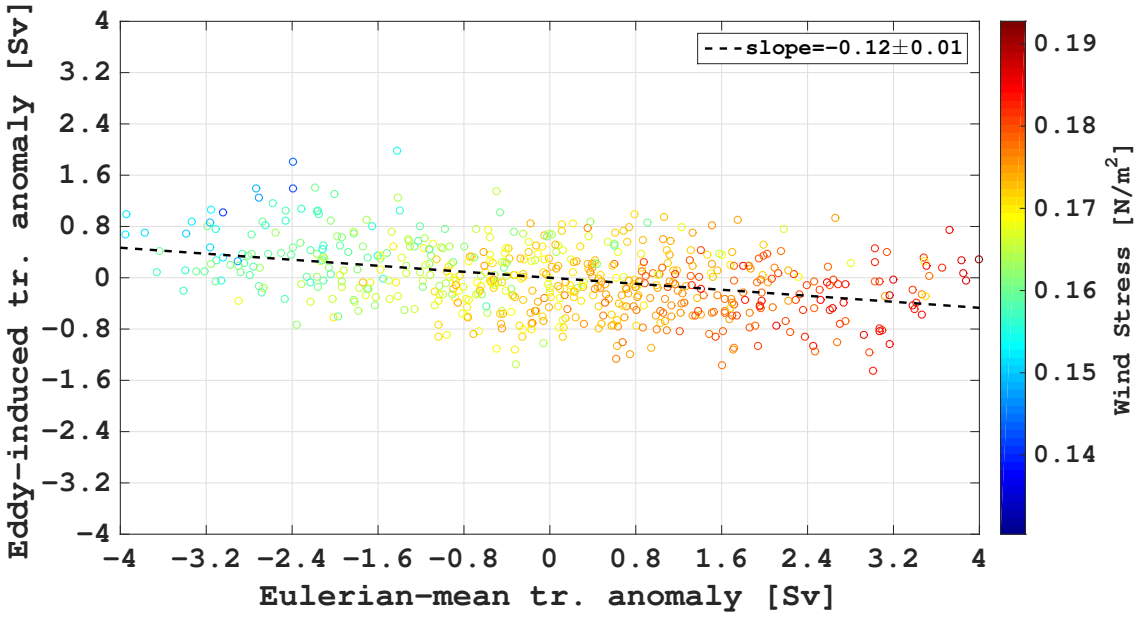

Figure 5.4: The annual-mean strength of the Eulerian overturning cell $\overline{\Psi}$ plotted against the annual-mean strength of the eddy-induced cell Ψ^*. The 600 yr temporal means have been subtracted to provide the anomalies. The color of the marks indicates the zonal wind stress over the ACC path at that specific time. The dashed line is a linear least-squares fit to the data-points.

correlated ($r = 0.97$). The weak influence from the eddies on the Eulerian-mean overturning results in a spread of ~ 2 Sv in the residual overturning at any given wind stress magnitude during the model run. This indicate, as was also shown in figure 5.4, that on an interannual basis, the eddy-induced cell does not always attentuate changes in the Eulerian-mean circulation, but sometimes even amplify it. The dashed line however shows that, on average, the instantaneous change in the eddy-induced circulation compensates the variability in the Eulerian-mean overturning, since its slope is less than unity, albeit weakly. That is, the transient eddies hardly balance any of the fluctuations in the Eulerian-mean overturning in this specific model run.

5.3 The baroclinic and barotropic ACC transport

The temporal mean streamline-averaged baroclinic potential energy (BPE) field (blue line, figure 5.6) shows that the BPE increases monotonically towards equator, consistent with the spatial structure of the BPE field (figure 4.10), and is a product of the strong SO meridional density gradient. This profile is relatively robust given the smallness of the superposed errorbars, which reflect the fluctuations in the density field due to the

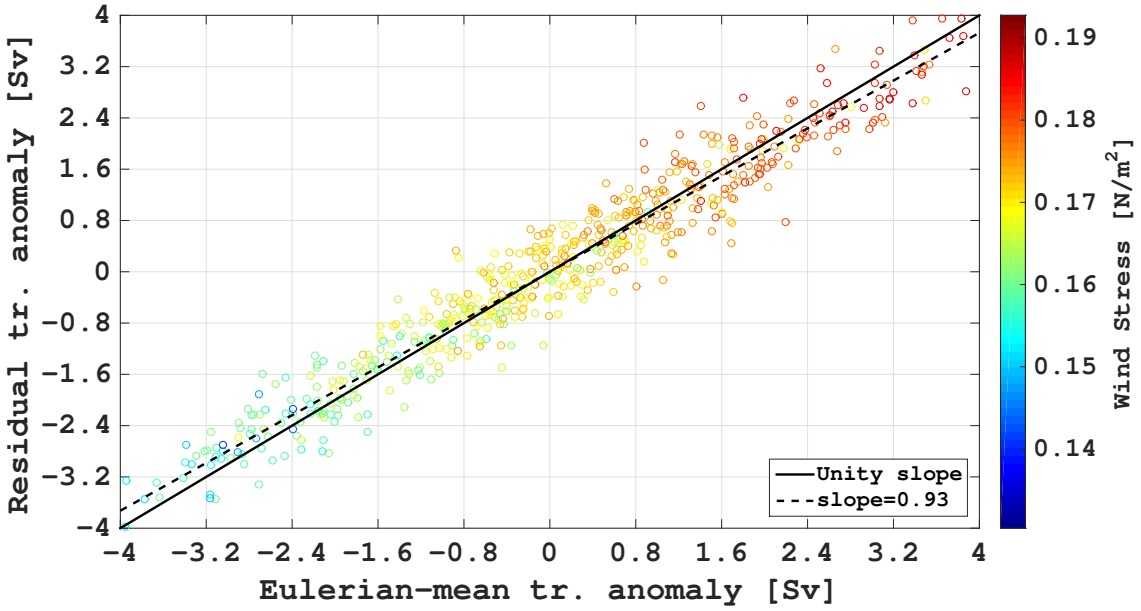

Figure 5.5: As figure 5.4, but for the Eulerian-mean overturning strength $\overline{\Psi}$ against the residual overturning $\Psi_{\mathrm{Res}} = \overline{\Psi} + \Psi^*$. The solid black line is a reference line with unity slope, and the dashed line is a linear least-squares fit to the data-points.

internal variability in the model run. The time-mean baroclinic transport per degree latitude (red curve, figure 5.6) is derived from the the meridional derivative of the streamline-averaged BPE field (eq. (4.6)), and shows two distinct transport maxima at the mean latitudes of $\sim 56°$S and $\sim 52°$S, indicating a local steepening of the isopycnals. Despite the little temporal variability in the BPE profile, the transport estimate varies substantially with time (red errorbars). The area under the transport curve is the baroclinic transport in the upper ~ 2000 m of the water column between streamline 5 Sv and 160 Sv, and amounts to approximately 60 Sv in the time-mean.

The mean of the baroclinic transport pr. degree latitude (blue curve in upper panel, figure 5.7) is a measure of the average slope of the BPE profile and thus constitutes a proxy for the isopycnal slope within the core of the ACC. It fluctuates with time around a value of $\sim 5.3\,\mathrm{SvDeg}^{-1}$, and corresponds to a streamline-averaged width of the ACC core of approx. 11° latitude. This width agrees roughly with the time-mean position of the streamlines 5 Sv and 160 Sv (figure 4.10).

The baroclinic transport integrated between these bounding streamlines (red curve, upper panel of figure 5.7), does not follow the isopycnal slope proxy (blue line), and actually displays a hint of anti-correlation, which at first glance might appear counter-intuitive, because one would expect a steepening of the isopycnals to lead to a stronger

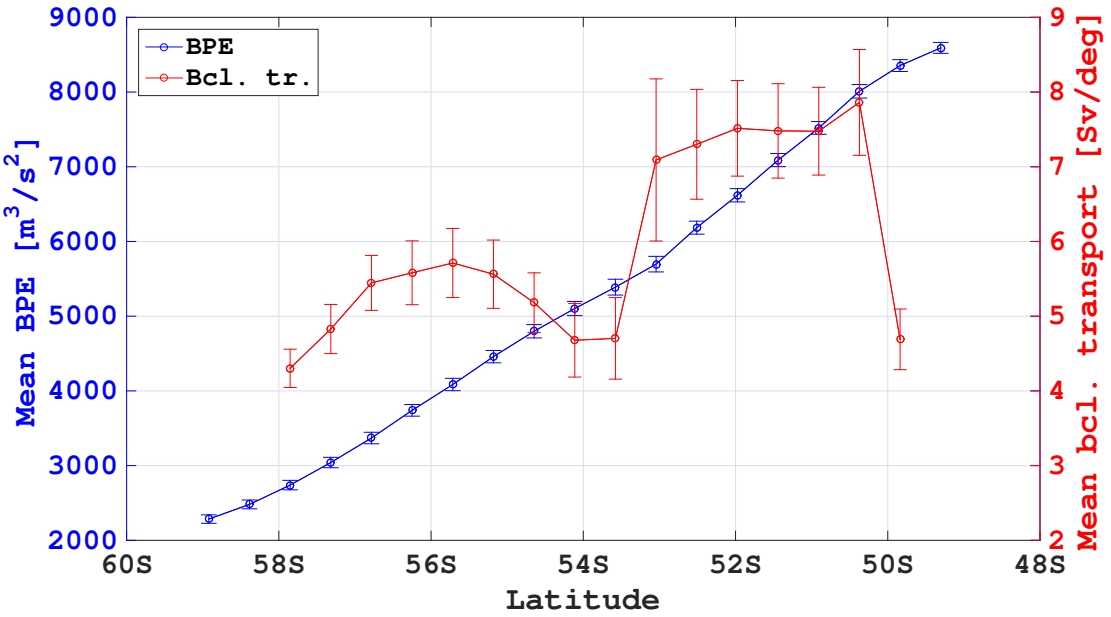

Figure 5.6: The blue curve shows the 600 yr time-mean streamline-averaged baroclinic potential energy (BPE). The annual mean streamline-averaged BPE was interpolated onto the CCSM4 model grid before a temporal mean was computed. The blue errorbar is the standard deviation of the entire time series. The red curve is the 600 yr time-mean baroclinic transport per degree latitude, and is obtained by eq. (4.6). The meridional derivative was taken before the BPE was interpolated onto the model grid. The red errorbars show the standard deviation of the time series.

baroclinic transport. The explanation to this behavior follows by the rather unorthodox method in use; by following the streamlines of 5 Sv and 160 Sv, volume transport is conserved by construction, and the two components that make up the 155 Sv transport, the baroclinic and the barotropic, has to be in anti-phase (as also explained in section 4.3.2).

The volume transport is a product of the zonal velocity field and the area of the meridional transect. When the ACC intensifies, the transect area has to decrease by confluence streamline 5 Sv and 160 Sv in order to conserve the total transport of 155 Sv. When the isopycnal slope proxy (blue line) and the integrated baroclinic transport (red line) are seen not to correlate, it is because the isopycnals do not steepen enough to explain the majority of the intensification of the confined ACC core. That is, the baroclinic transport explains a smaller fraction of the total transport between the ACC core bounds (streamline 5 Sv and 160 Sv) when the current strengthens. The relevant quantity to study is thus not the integrated baroclinic or barotropic component in solitude, but instead their ratio, which indicate whether it is the barotropic or the baroclinic transport component that dominates change in the transport of the ACC

core. The baroclinic transport of the *entire* current (not the 155 Sv ACC core) does however increase during an intensification of the ACC, consistent with the steepening of the isopycnals, as expected.

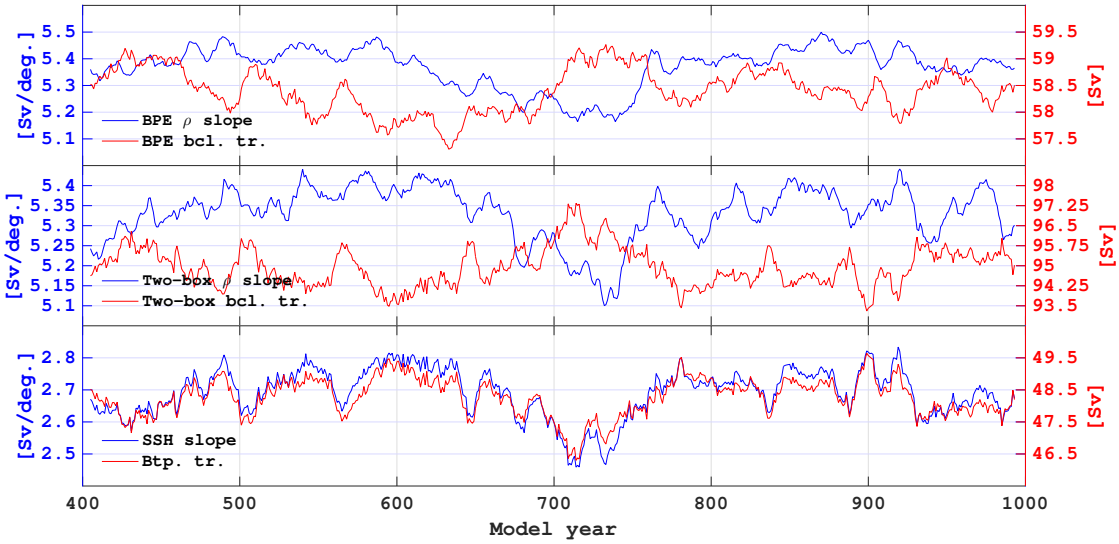

Figure 5.7: The upper panel displays the baroclinic transport obtained from the BPE field (section 4.3.1). The middle and lower panel shows the baroclinic and barotropic transport signals, respectively, from the two-box method (section 4.3.3). The blue curves are the means of the transport per degree latitude. These constitute a proxy for the isopycnal slope and the slope of the sea surface height within the ACC core, for the baroclinic and baroptropic components, respectively. The red curves are the integrated transports.

This notion is supported by the baroclinic signal from the simpler two-box method (middle panel, figure 5.7), outlined in section 4.3.3, which also gives the impression that the baroclinic transport fraction of the 155 Sv (red curve) decreases during steepening of the isopycnals (blue curve). This estimate yields a ~ 40 Sv greater baroclinic transport than the one obtained from the BPE field, but the relative variability is comparable. The ratio of the integrated transport (red curve) to the measure of the isopycnal slope (blue line) provides an estimate of the width of the current of about 18° in latitude, which is much greater than the streamline-averaged width obtained from the BPE estimate (approx 11°). The transport components obtained using the two-box method are however extracted from the flow where topography is relatively flat, where the current is less constrained by f/h contours, and hence occupies a larger area (look at the width of the current at 190°E, 260°E and 275°E, figure 4.10).

The barotropic component (lower panel, figure 5.7), in contrast, exhibits a strong

correlation between the mean barotropic transport per degree latitude (a proxy for the mean sea surface height) and the integrated barotropic transport. This suggests that the strengthening of the zonal velocity field due to a stronger SSH gradient is greater than the narrowing of the streamlines and the decrease of the transect area, and conclusively, the barotropic response is stronger than the baroclinic response during an intensification of the current. As noted above, the integrated baroclinic (red curve, middle panel) and barotropic transport (red curve, lower panel) signals are strictly anti-correlated, because volume transport is conserved.

5.4 The response of the Southern Ocean density field to wind stress variability

Having tested the relevance of the wind stress metrics and determined the sensitivity of the residual MOC to wind stress variability, as well as having decomposed the circumpolar transport, it is now possible to present the results that aim to answer the fourth and last scientific question; How insensitive is the SO circulation to low-frequency wind stress changes?

The streamline-averaged BPE anomaly time series (upper panel, figure 5.8) shows that the variations in the SO density field is mainly uniform in the meridional, with deviations from the time-mean BPE by up to $300\,\mathrm{m^3 s^{-2}}$. The definition of the BPE (eq. (4.5)) implies that such latitudinally invarient response arises from a general subsidence or lift of the isopycnals, because the deviation density field $\delta\rho(x, y, z, t) = \rho(x, y, z, t) - \rho_0$ must change equally at all latitudes. That is, if $\delta\rho$ becomes less negative, because heavier water is lifted up into the upper $\sim 2000\,\mathrm{m}$ of the ocean, the BPE must decrease. Consequently, this type of response does not impact the meridional slope of the BPE field or the baroclinic transport.

There appears to be a widespread lift of the isopycnals in the last half of the 7th model century, and a gradual depression beginning around year 800. This anomaly is associated with a weakening of the winds over the ACC path (blue line in lower panel, figure 5.8), and also coincides with the decadal model trend from year 665 to 714 (figure C.3). The density field does not experience any other major displacements, despite that similar fluctuations in the wind stress occur.

The BPE-based proxy of the isopycnal slope (blue line, upper panel figure 5.7), is seen to co-vary with the wind stress over the path of the ACC (lower panel, figure 5.8), though with a few major offsets, such as the one found around year 675. It follows

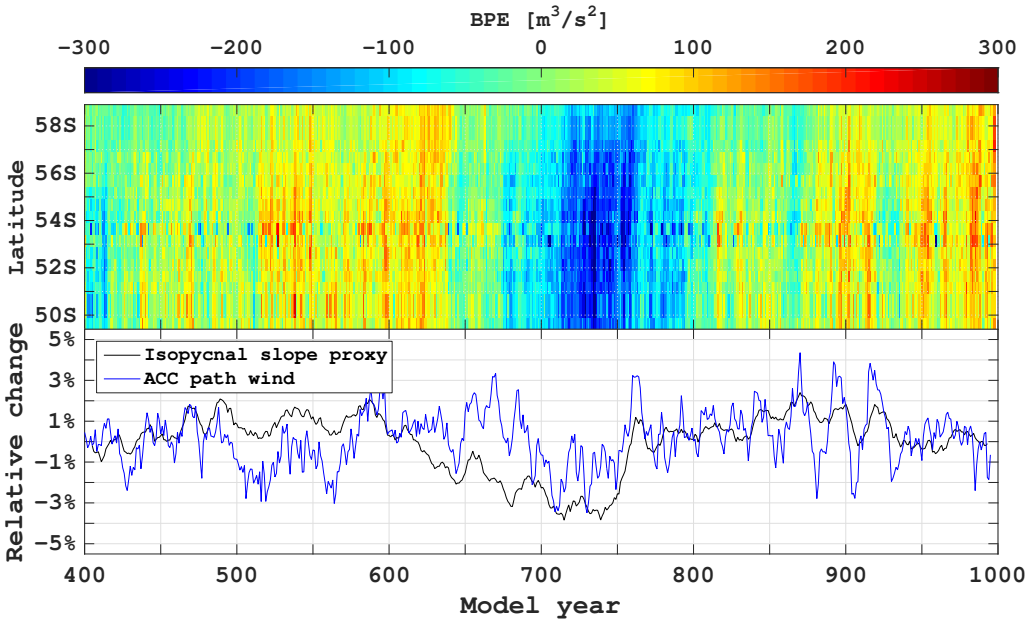

Figure 5.8: The upper panel displays the BPE field, regridded to the CCSM4 model grid. The 600 yr temporal mean has been subtracted to provide the anomalies in the BPE. The black curve in the lower panel displays the isopycnal slope proxy (blue curve in upper panel, figure 5.7) that is derived from the BPE field. The blue curve is the wind stress over the path of the ACC.

that there is a change in the slope of the isopycnals with time (upper panel, figure 5.8), but which is hardly visible, because the meridional uniform lift and subsidence of the isopycnals saturates the density field variations. Thus, in this model setup, the isopycnals are not completely insensitive to the local wind stress variability.

In order to study this relationship between the baroclinic transport of the ACC and the wind stress variability in detail, we analyse figure 5.8 by focusing on the three wind stress trends (figure C.3), which were discussed in section 4.2.3.

The first 50 yr wind stress trend from year 462 to 511 is negative (upper panel, figure 5.9), and is only weakly significant (table 4.1), because the decrease in wind stress is only present in the last part of the time span in focus, starting around year 490. Nevertheless, the two wind stress anomalies prior to the negative trend in the wind stress are seen to excite two baroclinic responses (middle panel, figure 5.9), and the baroclinic transport is also seen to decrease at the onset of the negative wind stress trend. The transport signal is seen to exhibit less variability compared to the wind stress in terms of the relative change. The entire 50 yr trend in the isopycnal slope proxy is though statistically insignificant ($p > 10\%$).

The transport maximum around year 480 is caused by a depression of the isopycnals

on the tropical flank of the ACC (lower panel, figure 5.9), and the subsequent minimum at year $\sim$ 490 is associated with a general decrease in the isopycnal slope. The decrease in transport during the negative wind stress trend is less apparent in the BPE field, but in the end of the time series at year 510 the poleward flank of the ACC holds a positive BPE anomaly, whereas the tropical flank is subject to a negative. In general, the baroclinic signal appears lagged by a couple of years with respect to the wind stress signal.

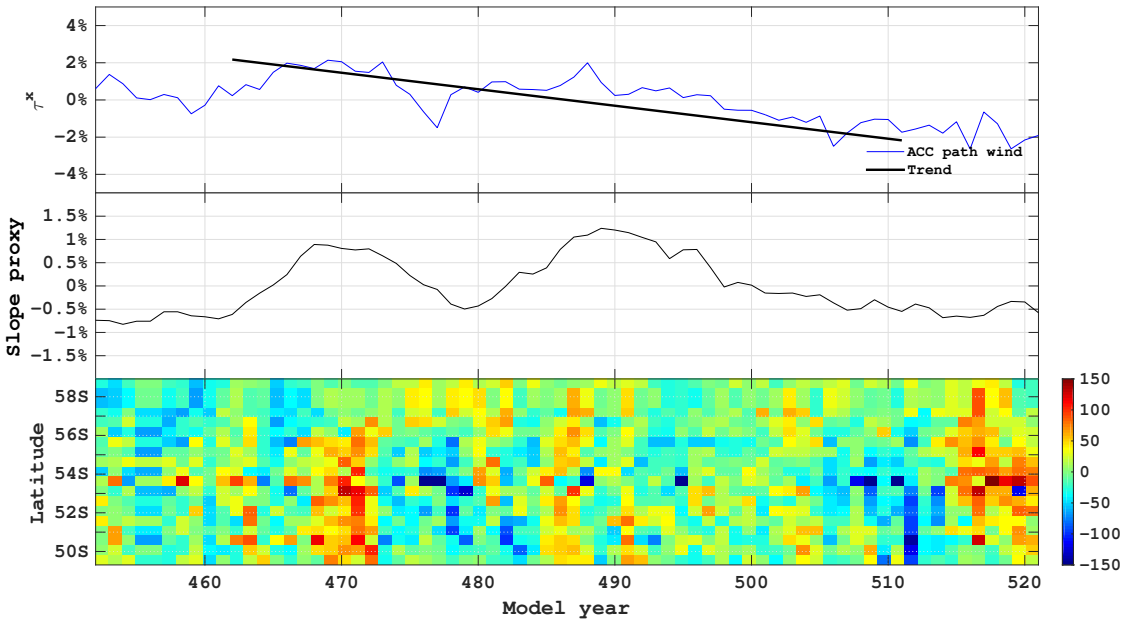

Figure 5.9: Analysis of the model wind stress trend from year 462 to 511. The blue and black lines in the upper panel displays the wind stress over the ACC path and the associated 50 yr trend, respectively, normalized by their temporal means. The middle panel displays the meridional mean of the baroclinic transport per degree latitude (isopycnal slope proxy) obtained from the BPE field. This signal has also been normalized by its temporal mean. The lower panel is the streamline-averaged BPE field. The wind stress trend is significant at the 10% level, but the associated trend in the baroclinic transport is insignificant. The units of the colorbar are $\mathrm{m}^3\mathrm{s}^{-2}$.

The significant wind stress trend from year 551 to 600 is positive, and is seen to excite a statistically significant ($p < 5\%$) baroclinic response (left panels, figure 5.10), that appears around year 565, but with a smaller amplitude than the wind stress trend, as was also the case for the 462-511 yr trend. The link between the transport and the density field is less clear, but in general the isopycnals are found to subside on the tropical flank during the wind stress anomaly. Interestingly, the baroclinic response ceases before the wind stress reaches its maximum.

The model trend from year 665 to 714 is the strongest in the 1000 yr integration, and

is also the most statistically significant (table 4.1), showing a seven percent decrease in the wind stress over the ACC path (upper right panel, figure 5.10) during the 50 yr time span. It is associated with a statistically significant 2% drop in the isopycnal slope proxy (middle right panel, figure 5.10), and a large-scale lift of the isopycnal surfaces across the ACC (lower right panel, figure 5.10). The most pronounced change in the meridional density gradient is on the poleward ACC flank. Like the other cases, the baroclinic signal appears to lag the wind stress by a few years.

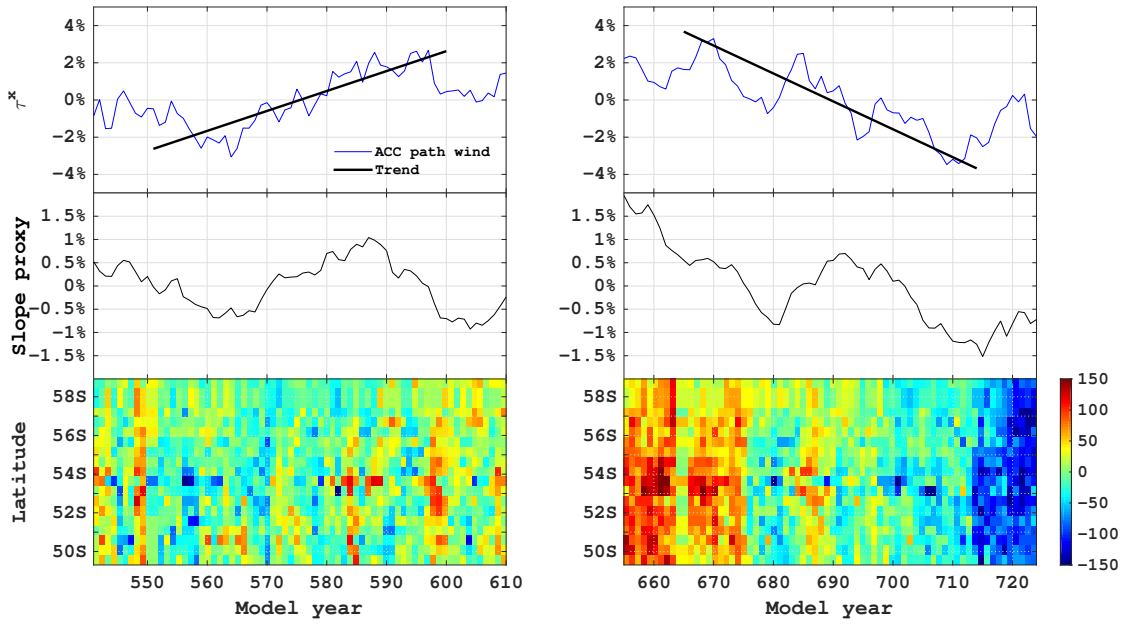

Figure 5.10: Same as figure 5.10, but for model wind stress trend from 551 to 600 (left panels) and from 665 to 714 (right panels). The trends in the wind stress and the isopycnal slope proxy in the time span 551-600 are both significant at the 5% level. The trends in the wind stress and the isopycnal slope proxy in the time span 665-714 are significant at the 1% and 10% level, respectively.

Despite that it is possible to identify covariability between the SO local wind stress and the large-scale isopycnal slope in the model (figure 5.8, 5.9 and 5.10), a robust linear relationship between the two variables is not apparent. It is visible that strong wind events are associated with relatively steep isopycnals, but from figure 5.11 it is also seen, that a minor cluster of strong wind events is concurrent with a negative anomaly in the isopycnal slope proxy i.e. a relaxation of the isopycnals. Such event are also clearly visible in the time series (lower panel, figure 5.8), as for example in the time span from year 600-650, where the winds are relatively strong, but the baroclinic transport of the entire ACC decreases. The barotropic response (blue curve in lower panel, figure 5.7) shows similar behavior, and strong wind stress events are found to

pair with both positive transport anomalies as well as no response at all.

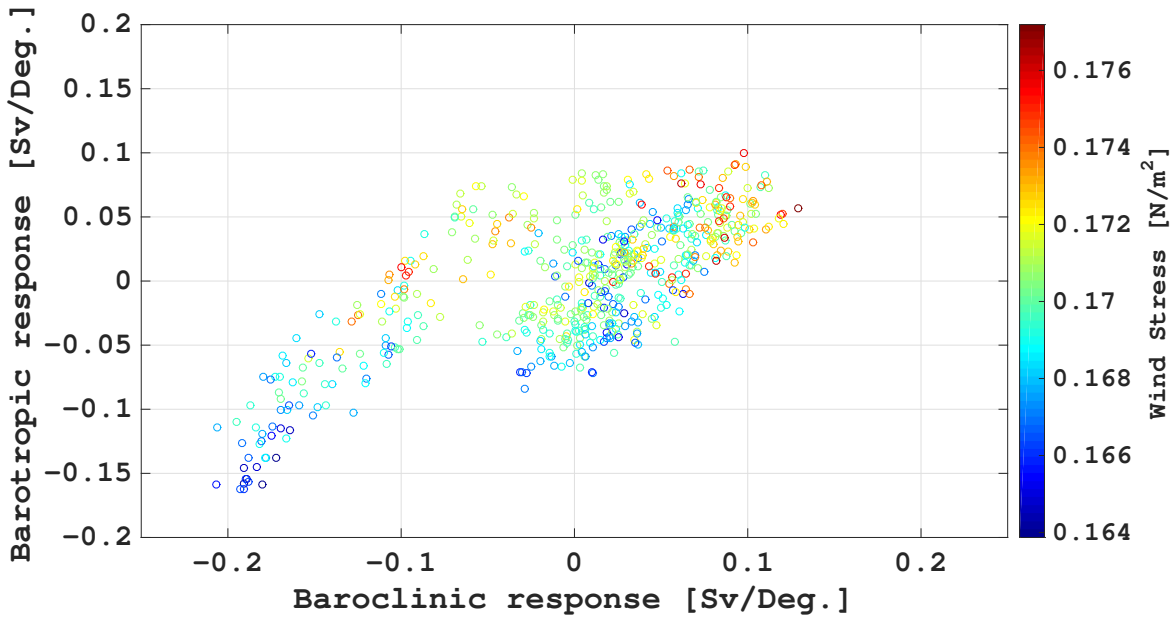

Figure 5.11: The isopycnal slope proxy (blue line in upper panel of figure 5.7) obtained from the BPE field against the sea surface height proxy (blue line in lower panel of figure 5.7) obtained from the two-box method. The 600 yr temporal means have been subtracted to provide the anomalies. The color of the circular marks indicate the wind stress over the ACC path.

The barotropic and baroclinic responses within the ACC core show a degree of positive correlation ($r = 0.73$, figure 5.11) i.e it is likely that both responses are excited at the same time.

Chapter 6

Discussion

6.1 The relevance of the wind stress metrics

Let us first address the scientific question that revolves around the need of a relevant wind stress metric.

From figure 5.1 it was not possible to establish a simple and robust relationship between any of the wind stress metrics and the Drake Passage transport. Together with local wind forcing, the circumpolar volume transport of the ACC has previously been shown to be a function of surface buoyancy fluxes (Gent et al., 2001), diapycnal mixing (Munday et al., 2013), eddies (Hallberg and Gnadadesikan, 2006), topography (Hogg and Blundell, 2006; Nadeau and Straub, 2009), and a link to the deep water formation in the northern hemisphere has also been suggested (Gnanadesikan, 1999). The influence from these processes on the decadal variations in the transport are thus significant, and addressing the relevance of the wind stress metrics from this comparison alone is consequently a complicated matter.

To lent further support to this conclusion, a fifth measure of the zonal wind stress is defined and compared to the Drake Passage transport. This metric is the zonal wind stress directly over the Drake Passage gap (the square patch between long. 286°E and 297°E and between lat. 63°S and 55°S), and is choosen on the basis of a model sensitivity study, that shows that the transport is highly sensitive to the zonal wind stress in this specific area (Mazloff, 2012). Physically, the Ekman divergence due to the wind stress shear add vorticity to the ocean and allows the water column to advect across the closely packed f/h contours in the region (figure 1.4) and generate a barotropic response along them.

The comparison of this metric to the Drake Passage transport is shown in figure

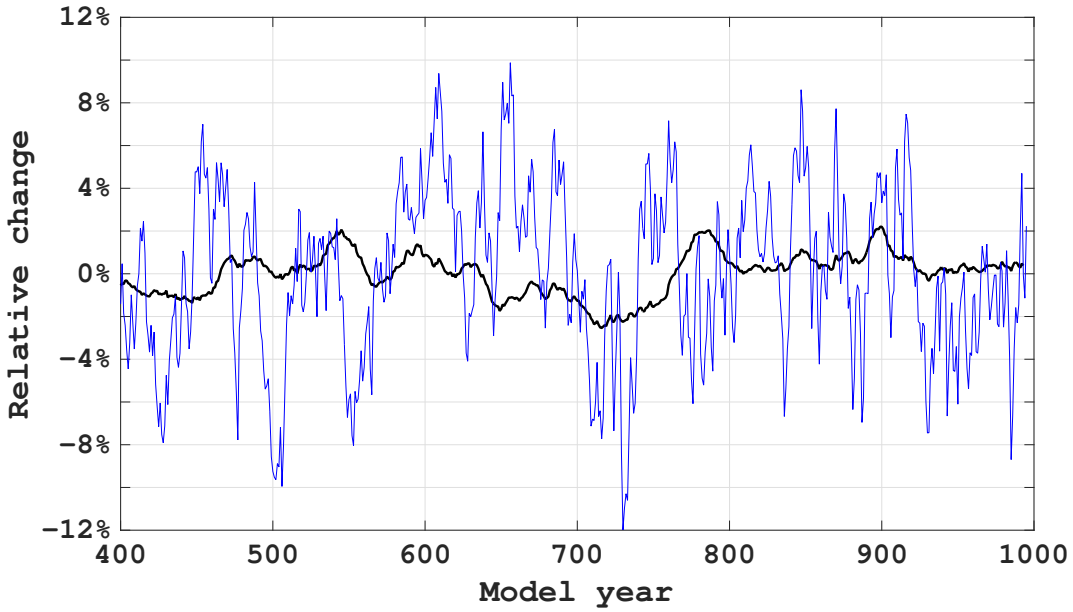

Figure 6.1: The black line is the Drake Passage volume transport (figure 4.1). The blue line is the wind stress at the Drake Passage, and is given by the mean zonal wind stress between long. 286°E and 297°E and between lat. 63°S and 55°S. A ten-year running mean has been applied to both curves.

6.1. This metric shows strong fluctuations of up to 10% of its mean value ($0.14\,\mathrm{N/m^2}$), and even exceed the fluctuations in the energetic mean wind stress within the Drake Passage latitude band (red curve, figure 4.9), but it is also constrained by fewer grid points. The correlation between the two variables is though insignificant, and this wind stress metric does not provide any further insight on how the wind forces the current.

Neither do the comparison between the eddy-induced circulation and the wind stress metrics aid our desire to decide on the most relevant wind stress measure (figure 5.3). The modest covariability between the two variables indicates that the density field, which the cell depend on, is not only set by the winds. Moreover, they are not necessarily directly proportional, because it is possible to to have a finite isopycnal slope, and thereby an eddy-induced overturning, at zero wind stress, due to thermal- and fresh water fluxes at the ocean surface (Borowski et al., 2002). It is therefore made difficult to even quantify the correct scaling between the two variables in terms of relative change, as the zero wind stress overturning is unknown in this specific model run.

However, the comparison of the wind stress metrics to the Eulerian-mean overturning cell (figure 5.2) is more accessible, because the wind stress is linearly porportional to the overturning through Ekman dynamics (Marshall and Radko, 2003). The wind

stress over the path of the ACC scales with the circulation metric the best in terms of relative change, and is therefore deemed the most relevant wind stress metric out of the four, followed by the maximum of the zonally-averaged zonal wind stress field.

This conclusion might be supported by energy considerations. The time-mean zonal wind stress is the main wind power input to the surface geostrophic circulation in the Southern Ocean (Wunsch, 1998), which drives the Ekman pump (Roquet et al., 2011), that in turn converts large-scale kinetic energy into large-scale APE (Storch et al., 2012). This reservoir of potential energy is depleted through baroclinic instability, which generates mesoscale eddies and hence EKE. This EKE is mainly dissipated at the bottom through form drag (Munk and Palmén, 1951; Johnson and Bryden, 1989), thereby balancing the power input from the strong westerlies (the approximate momentum balance presented in section 2.2).

Eddy resolving model studies, executed with present-day conditions, but in idealized settings, show that that the equilibrated ACC is baroclinically unstable, and that the wind power input sustains a pool of EKE of considerable size, manifested by strong variability around the time-mean transport of the ACC (Hallberg and Gnadadesikan, 2006). More importantly, with a sustained increase in the wind power input, the enhanced Ekman pump does not necessarily result in more large-scale APE and a stronger ACC. The production of mesoscale eddies might increase simultaneously, and the excess APE is immediately converted to EKE and subsequently dissipated. This is the eddy saturation limit, in which the time-mean circumpolar transport is independent from the wind stress (Hogg and Blundell, 2006; Munday et al., 2013).

The coarse resolution CCSM4 with a constant thickness diffusivity does not possess a similar energy cycle, because the conversion rate of large-scale APE to EKE is dependent on the size of the pool of APE itself (Gent et al., 1995). A sustained increase in the wind power input must result in steeper isopycnals, in order to enhance the effect of baroclinic instability, and a depletion of the APE pool at a rate that balances the associated generation of the APE. An increase of the ACC transport will always follow a wind stress increase in CCSM4, fundamentally different from the threshold behavior of eddy resolving models, where the generation rate of mean kinetic energy to APE always balances the dissipation rate of APE to EKE, without a change in the large-scale isopycnal slope, as soon as the baroclinic instability threshold is reached.

With a κ_{GM} that allows for spatiotemporal variability, it is in principle possible to mimic the eddy saturation dynamics of the eddy resolving models, if the thickness diffusivity increases sufficiently in the wake of a sustained increase in the wind power input to the APE reservoir. This will facilitate a conversion of APE to EKE without

a change in the isopycnal slope and the ACC transport. However, practically this does not seem likely, as the formulation of the thickness diffusivity in the present model configuration is dependent on the stratification as well (Ferreira et al., 2005; Danabasoglu and Marshall, 2007).

The pool of EKE in the model run does not appear to change much with variations in the low-frequency wind stress, as seen when one investigates the variability of the eddy-induced circulation (figure 5.4). The Ekman pump is seen to generate relatively strong variability in the Eulerian-mean overturning ($\pm 4\,\mathrm{Sv}$), with a noticable effect on the density field (lower panel, figure 5.8), but the eddy-induced overturning does only change by $\pm 1.5\,\mathrm{Sv}$. In the light of the eddy resolving model studies, this prompt the conclusion that the conversion rate of APE to EKE is too insensitive to changes in the ocean density structure, and that the reason might be that the thickness diffusivity ($\kappa_{\mathrm{GM}} = 604 \pm 11\,\mathrm{m^2/s}$)[1] should possess stronger variability with time.

This discussion suggests that the dominant changes in energy due to low-frequency wind stress changes are found in the pool of large-scale APE, and hence in the mean transport of the ACC. Many model studies with parameterized eddies find a close to linear match between the wind stress and the circumpolar transport in the time-mean; Munday et al. (2013) and Hallberg and Gnadadesikan (2006) uses the maximum of the zonal wind stress jet as their metric, and Jochum and Eden (2015) uses the wind stress at the northern limit of the Drake Passage. If this linear response can be extended to the study of low-frequency variability, as is the focus here, we expect the relative changes in wind stress and transport to match closely in scale (figure 5.1). Despite that no simple relationship is apparent, the fluctuations in the wind stress over the path of the ACC matches those in the Drake Passage transport better than any of the other three wind stress metrics, supporting the previous conclusion.

It is perhaps not surprising that it is the wind stress over the ACC path that appears to be the most relevant metric. The wind stress within the Drake Passage latitude band is a consequence of assuming that the ACC is purely zonal (e.g. Johnson and Bryden, 1989), and the zonally-averaged zonal wind stress at the latitude of the Southern tip of South America, suggested by Toggweiler and Samuels (1995), stem from the Drake Passage constraint on the SO dynamics. However, as noted from both observations and the model output (figure 1.4 and 4.3), the ACC escapes the Drake Passage latitude band in many locations on the circumpolar path, due to steering by topography. Moreover,

[1]This estimate of the thickness diffusivity is obtained from the κ_{GM} field by applying a complete zonal average, a meridional average from 66°S to 38°S and a depth average from 200 m to 1000 m. The measure is inspired from (Jochum and Eden, 2015).

eddies play a key role in the SO dynamics, and the northward Ekman transport at the northern bound of the Drake Passage does not necessarily scale with the amount of water that upwells in the Drake Passage latitude band.

Defining the wind metric as the maximum of the zonally-averaged zonal wind stress field or the wind over the ACC path is more suitable. In contrast to the other two wind stress metrics, these measures of the wind are dependent on both space and time. Since the ACC appears to be located at the wind stress maximum (see the wind stress field within the mask of figure 4.8), these two metrics capture the wind stress that coincides with the position of ACC. It is these winds that help to maintain the density structure through Ekman dynamics.

Finally, the fluctuations in the SAM co-varies with the wind stress over the path of the ACC throughout the entire model run (right panel, figure 4.7). The wind stress variability captured by the SAM is thus relevant to the discussion on the relationship between the wind forcing and SO circulation, as assumed in many wind forcing studies of the SO (e.g. Langlais et al., 2015).

6.2 Model limitations

We now pursue an answer to the second question, which addresses the sensitivity of the residual MOC to changes in the wind stress, given that the wind stress over the ACC path is the most relevant wind stress metric.

It is not possible in the present study to address the degree to which eddies compensates the directly wind-driven MOC as function of wind stress in CCSM4, because only one equilibrated model integration is available. The effect though is key, because it determines the sensitivity of the density field to sustained wind stress changes. Previous coarse resolution model studies have concluded that modelling the effect of the eddies with a GM-parameterization and a constant thickness diffusivity produces too little compensation compared to eddy-resolving models (Hallberg and Gnadadesikan, 2006). However, with κ_{GM} specified as in Ferreira et al. (2005), it has been shown through a wind stress sensitivity model study that CCSM4 now compensates to a degree that agrees with high-resolution model studies (Gent and Danabasoglu, 2011).

The validity of this assertion has recently been questioned (Jochum and Eden, 2015). Where both overturning cells are indeed found to respond to increases in wind stress, ranging from zero wind stress to a doubling of the present day magnitude, the residual overturning circulation remains linearly dependent on the wind stress magnitude. This finding does not support the idea of increasing eddy compensation with wind stress,

which is suggested by eddy resolving models (Munday et al., 2013), and the quality of the parameterization is again subject to dispute. Hence the MOC response to wind stress change is not substantially different from the coarse resolution model runs with a constant thickness diffusivity. This shortcoming is attributed to the fact that the position of the two cells do not coincide exactly, which conflicts with analytic zonally-integrated theory (section 2.4).

Parallel to the possible lack of eddy compensation in the model, figure 5.5 shows that fluctuations in the wind stress over the path of the ACC are strongly correlated with those of the Eulerian-mean overturning. Moreover, the variability in the Eulerian-mean overturning almost solely determines the variability in the residual overturning. These results suggest that the model SO density field is relatively sensitive to low-frequency wind stress variability, just as the lack of eddy compensation faciliates a relatively strong response in the density field to changes in the time-mean wind stress. It seems likely that the similarity between these two types of responses are related, because they both depend on the eddy closure.

In addition, and as already briefly touched upon, the parameterization prevents the model from eddy saturating, because the eddy transfer coefficient is dependent on the stratification. With explicit eddies, the ACC possesses threshold behavior, where an upper limit to the slope of the isopycnals exists, and beyond which the current is entirely unstable. Wind perturbations are able to generate a response in the density field, such that the isopycnal slope momentarily exceeds the threshold. The isopycnals will though immediately slump back to the threshold level, converting the excess large-scale APE into EKE through baroclinic instability, and enhance dissipation of momentum at the ocean bottom (Hogg and Blundell, 2006).

The ocan component of CCSM4 does not possess an upper threshold for the isopycnal slope, and hence the transport of the ACC will always increase with increasing winds (Fyfe and Saenko, 2006), and will not generate a sufficiently strong eddy field. Other specifications of κ_{GM}, such as the scheme by Eden and Greatbatch (2008) that depends on a prognostic equation for the EKE, might capture the necessary physics to provide eddy saturation. This has yet to be tested. In concert with the incorrect eddy compensation behavior, these problems highlight the need of a thickness diffusivity that correctly mimics these physical processes, in order to increase the accuracy of climate predictions.

6.3 Assessment of the Böning-hypothesis

Despite the shortcomings of the model, the time-mean BPE profile and its associated transport (figure 5.6) compares well to those obtained by Böning et al. (2008) (see their figure 5a). Both figures show a BPE profile (blue line) that increases monotonically towards equator and two characteristic transport maxima (red line), but with a general offset between the two figures by $\sim 4°$ in latitude. Specifically, their maxima fall on 53°S and 47°S, whereas the peaks presented in figure 5.6 sit at 56°S and 52°S.

They identify the two peaks as the two major fronts of the ACC, the subantarctic front and the polar front, but since these frontal regions are not resolved in CCSM4, the same conclusion cannot apply to the peaks in figure 5.6. Rather they are a product of the potential vorticity constraint on the flow, where certain streamlines are seen to confluence in the proximity of topography (figure 4.3).

In contrast to the claim by Böning et al. (2008) that the ACC baroclinic transport is insensitive to wind stress changes captured by the SAM, this study shows a noticeable response in the isopycnal tilt to wind stress variability over the path of the ACC (figure 5.8). This response is illuminated by the detailed study in the three largest 50 yr wind stress trends of the model integration, of which two produce statistically significant ($p < 10\%$) responses in the density field (figure 5.9 and 5.10). All of these wind stress trends are one-half to one-third the strength of the present day trend (table 4.1), but are nonetheless able to produce a response of a few sverdrups. The strongest trend from year 665 to 714 produces the greatest response, and it seems likely that a more pronounced wind stress trend would produce a stronger response in the density field. The validity of these results are though dependent on the sensitivity of the model i.e. the degree of eddy compensation, which has proven to be insufficient. That is, the ocean response is most likely overestimated, in favor of Böning's hypothesis.

As noted from the discussion of the three wind stress trends (figure 5.9 and 5.10), the wind stress over the path of the ACC appears to be leading the baroclinic response by a couple of years. A cross correlation between the two signal does also confirm this behavior (blue line, figure 6.2), and is expected due to the slow propagation of the signal by the baroclinic Rossby waves (Rintoul and Garabato, 2013). The peak correlation is though weak, and might indicate that the variations in the density field are far from determined by the wind stress field alone. This questions the assumption made in section 4.1.2, that it is possible to extract the ocean response to local forcing from the circulation metrics. However, from the inspection of figure 5.8, it is clear that the two variables are at least dependent. For comparison, the fast barotropic response

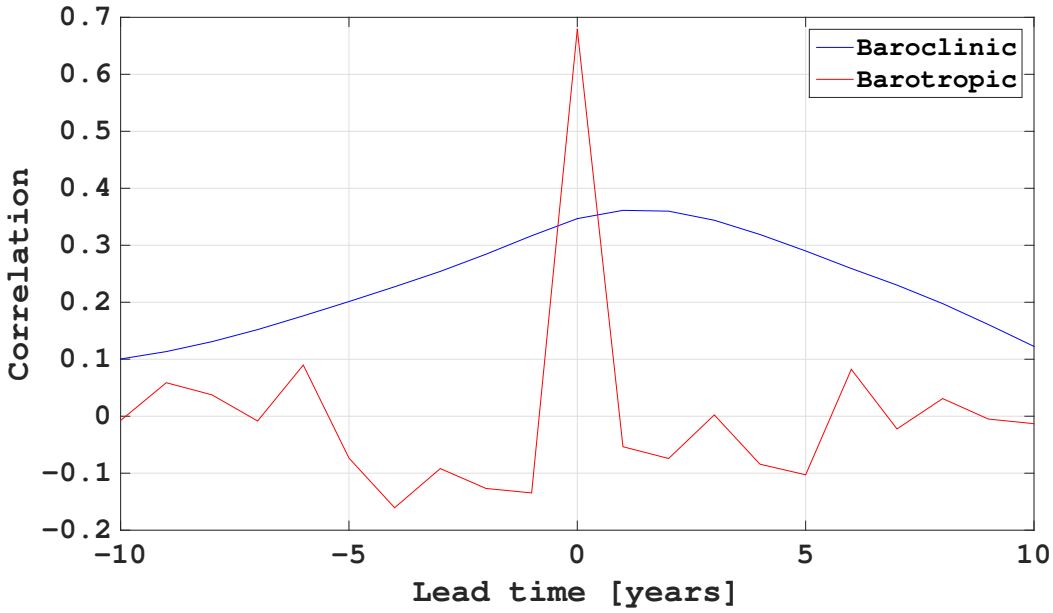

Figure 6.2: The blue line is the cross-correlation between the wind stress over the ACC path and the BPE estimated isopycnal slope proxy. The red line is the cross-correlation between the highpass filtered Drake Passage transport and the highpass filtered wind stress over the ACC path. The wind stress leads the transport metrics.

(red line, figure 6.2) is seen to sit at zero lag, with a dramatic drop in correlation for other lead times.

The time-mean baroclinic volume transport of the ACC core, obtained from the BPE field, is approx. 60 Sv, and is smaller than expected (upper panel, figure 5.7). Böning et al. (2008) report a baroclinic transport of about 80 Sv using the same method, the analytical model of Marshall and Radko (2003) suggests a transport of 75 Sv and review papers on the SO in general indicate that the ACC is considerably more baroclinic than barotropic (Talley et al., 2011; Rintoul and Garabato, 2013). The discrepancy between the presented time-mean baroclinic transport to these estimates might be evidence of that a substantial part of the baroclinic transport sits below the depth of ~ 2 km. This requires that the shear of the model zonal velocity field with depth is relatively weak.

Decomposing the flow with the simple two-box model also suggests a more realistic estimate of the baroclinic transport (approx. 100 Sv, middle panel, figure 5.7). This conflicts with the above assertion that the velocity profile should be weakly sheared, because the lower box contain about 30 Sv, and the separation boundary between the boxes is identical (~ 2075 m) to the one used in estimating the BPE signal. The upper part of the SO must contain the majority of the transport, and conclusively, the BPE

method fails to capture the correct amount of transport.

During the development of the baroclinic transport metric (4.6), it was assumed that the second term on the right hand side of eq. (4.3) is negligible. This rest upon the statement that $\nabla_2 \eta_B$ is zero at a depth of two kilometers, or in physical terms, that the circulation in the upper ocean does not encounter bathymetric features. From figure 4.10 it is visible that the flow is mainly steered around topography, and hence does not encounter it directly. A few streamlines are however noted to flow across the

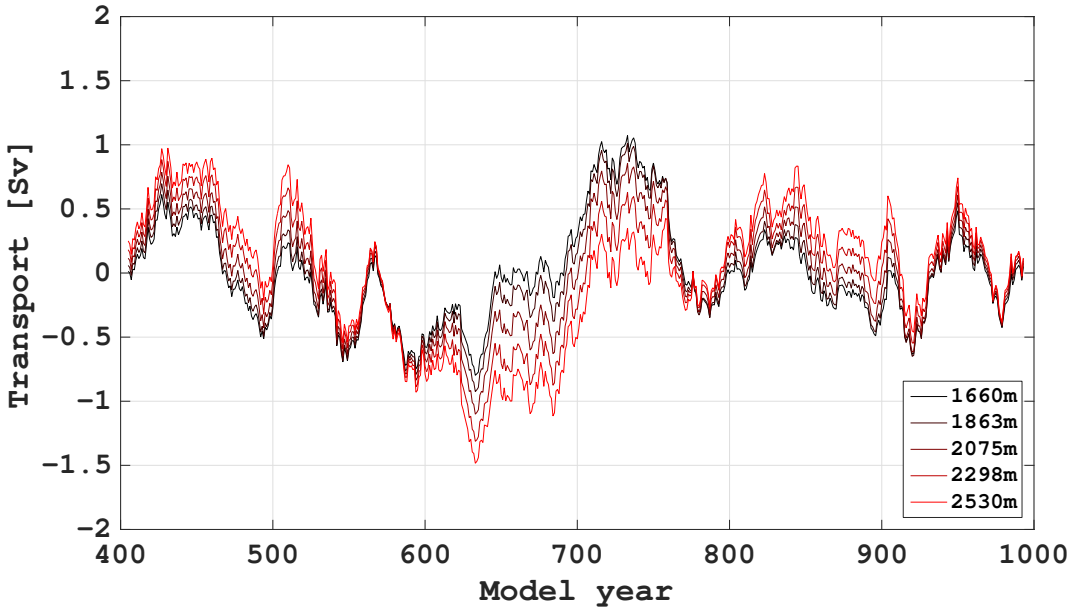

Figure 6.3: The integrated baroclinic transport obtained from the streamline-averaged BPE field for five different separation depths, ranging from 1660 m to 2530 m. The default metric is at 2075 m depth. The means have been subtracted, and range from $\sim$ 48 Sv to $\sim$ 64 Sv going from shallowest to deepest separation depth.

Kerguelen plateau, where the assumption obviously does not hold, but given the size of the discrepancy of about 40 Sv, it seems unlikely that this is the explanation to the shortcoming of the method.

A sensitivity test on the choice of separation boundary also shows that the structure of the signal is robust (figure 6.3), but that the mean baroclinic transport varies with separation depth, as expected. Then, a more likely explanation to the discrepancy between the two baroclinic transport estimates is that the fraction of baroclinic transport out of the conserved 155 Sv varies with longitude (the two-box estimates were obtained at 190°E, 260°E and at 275°E whereas the BPE-signal is a circumpolar average).

6.4 On the vertical displacement of the isopycnals

The rise of the isopycnals across the ACC concurrent with the relatively rapid decrease in wind stress from model year 665 to 714 is consistent with the finding by Böning et al. (2008), that the isopycnals subside during the present intensification of the westerlies. This behavior is not seen during the two other wind stress trends (the time spans from 462 to 511 and from 551 to 600), and it is therefore of interest to understand what conditions of the SO that leads to such response. figure 6.4 displays the spatial distribution of the difference in BPE, and it is seen that the rise of the isopycnals is evident in the entire SO, but is most prominent in the proximity of the ACC. Especially the rise in the Pacific Ocean and at the Drake Passage strikes the eye.

One possible explanation is an equatorward shift in the density field and a displacement of the ACC, as such an event would generate a negative BPE anomaly. However, from the streamlines superposed on the BPE difference (figure 6.4) it is seen that the ACC did not displace significantly during the 50 yr wind stress event. Moreover, if the ACC had moved with the displaced isopycnals, the BPE average along the streamlines would not have changed, and that is not the case (upper panel, figure 5.8).

It is more revealing to investigate the spatial changes in the zonal wind stress during the three wind stress events. Figure 6.5 shows that the negative wind stress trends (lower left and lower right panel) are associated with a weakening of the winds over the majority of the ACC path, as expected, but are also connected to a strengthening of the winds to the north. The opposite is true for the positive wind stress event (middle lower panel). With respect to the negative trends, this implies enhanced wind stress shear on the northern flank of the ACC and hence weakened downwelling. This constitutes a possible mechanism that is able to lift the pycnocline and hence explain the response in the BPE.

However, only the wind stress trend from year 665 to 714 generates a large-scale lift of the isopycnals, even though the change in the wind stress shear is evident during all three events. The changes in the shear during the two early wind stress events are though not as zonally symmetric and strong as the change for the last trend, which might explain the absent response in the ocean density field.

To further illuminate if this is the responsible mechanism, we take a look at the hydrographic changes in the upper 2 km of the zonally-averaged water column, before and after the lift of the isopycnals (figure 6.6). The field of potential temperature difference (left panel) shows a strong negative change at 50°S that intensifies near the surface, and is consistent with a lift of colder water towards the surface. This change

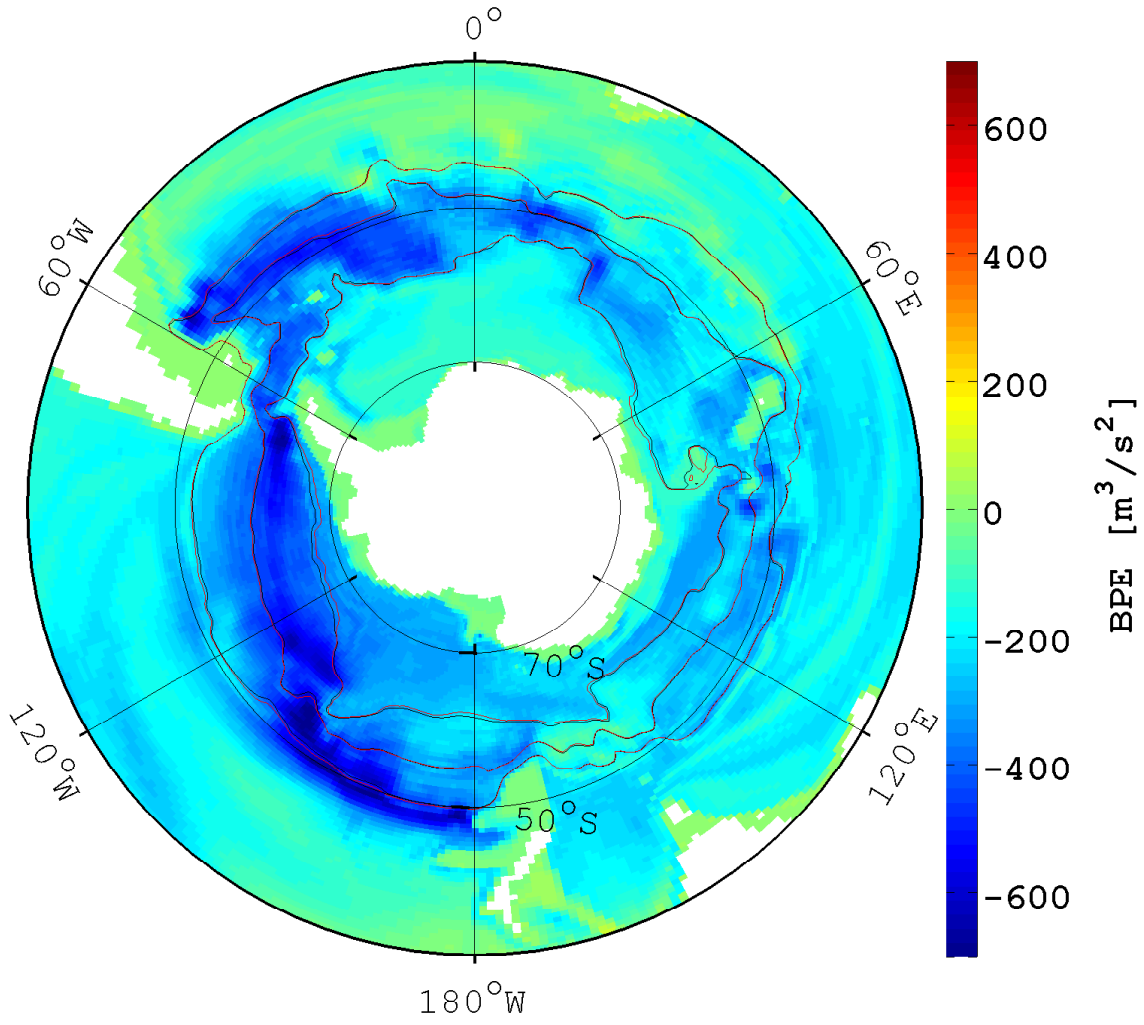

Figure 6.4: The BPE difference between the mean of the time span 730-760 and the mean of the time span 600-630. The three black lines are the streamlines 5, 80 and 160 Sv from the barotropic streamfunction from the mean of the early time span. The three red lines are the same as the black, but for the later time span.

also occur where the downwelling is seen to weaken the most (lower right panel, figure 6.5).

The salinity section (right panel) does not show a similar change. Due to the general downwelling of fresher water, we do not expect to see a sign-definite change throughout the water column, if it was mechanically forced to move upwards. The change does however confine itself to the very surface, especially evident at 60°S. The location of the isopycnals before (black lines) and after (white lines) the decrease in

BPE are superposed on both panels, and show that the largest movement takes place at depth, and not at the surface. That is, despite the greatest hydrographic changes sit in the upper part of the water column, they are not sufficient to explain the lift of the isopycnals, mainly because the stratification at the surface is strong.

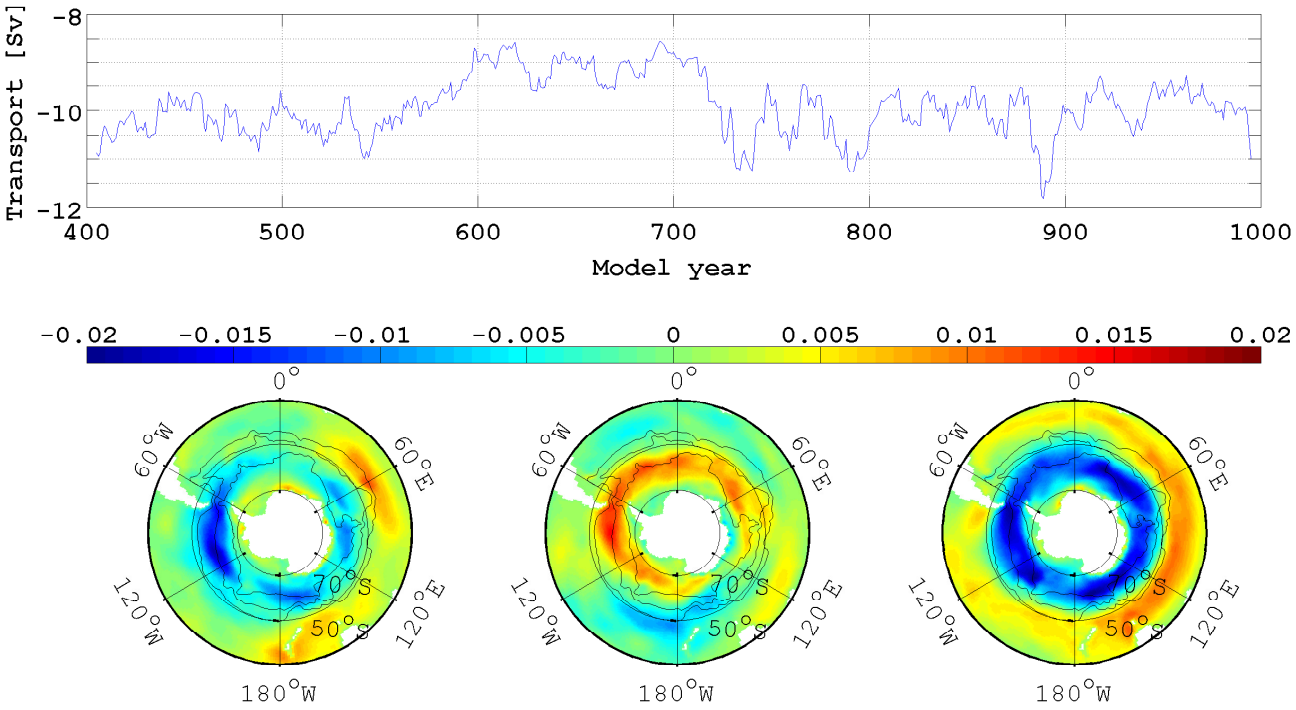

Figure 6.5: The upper panel displays the strength of the bottom cell of the MOC. The three lower panels display the difference in zonal wind stress across the three strongest multi-decadal wind stress trends of the model run. From left to right, mean of 500-520 minus mean of 450-470, mean of 590-610 minus mean of 540-560 and mean of 710-730 minus mean of 650-670.

What explains the lift of the isopycnals at the bottom remains unknown, but one explanation could be enhanced bottom water formation (upper panel, figure 6.5). Quantified by looking at the strength of the lower cell in the global MOC, it is seen that the production was rather low in the period from year 600 to year 700, but the lift of the isopycnal begins around year 650, and the connection is therefore not clear.

6.5 AMOC and climate

One major unanswered question, but beyond the scope of this thesis, is whether the SO response to the wind stress variability manifests itself as a change in the recirculation

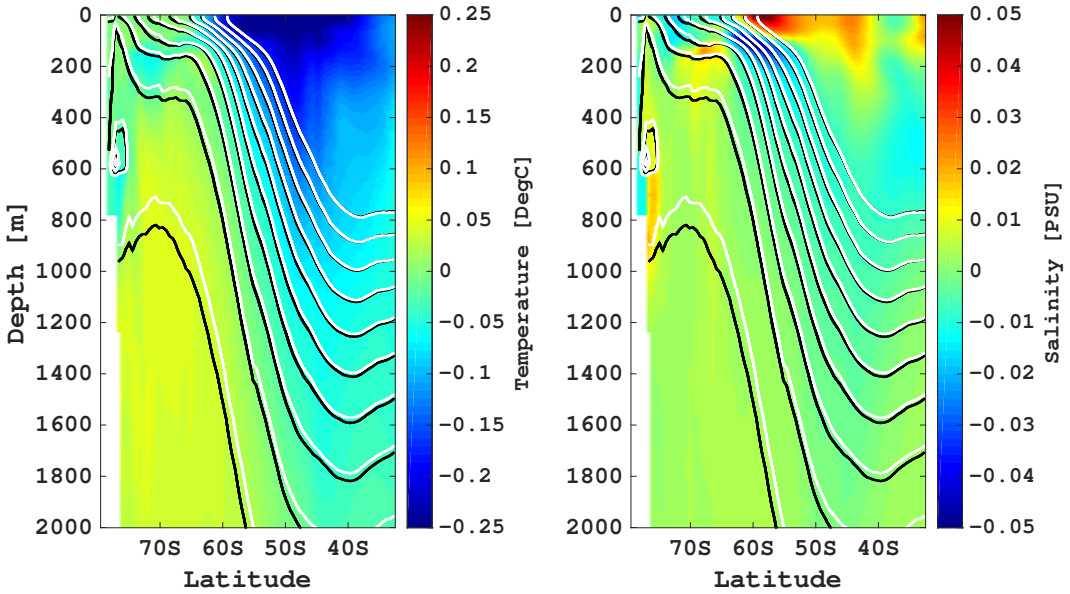

Figure 6.6: The left panel displays the difference in the zonally-averaged temperature field between the time spans 730-760 and 600-630. The right panel displays the same, but for salinity. Superposed on both panels are the mean location of the isopycnals 1027 kg/m^3 to 1028 kg/m^3 with a 0.1 kg/m^3 increment for both the time span 600-630 and 730-760.

of the SO MOC or a change in the AMOC strength. In the non-eddy limit, the Atlantic outflow into the SO, and hence the strength of the AMOC, is controlled by the strength of the wind stress, as long as deep water formation in the north is provided (Toggweiler and Samuels, 1995). In this limit, the amount of water that recirculates does not change as function of the wind stress magnitude. Idealized eddy-resolving models do show that the AMOC is governed by the SO winds to some extent, albeit weaker due to the compensating effect of eddies. This points toward a total eddy compensation limit, in which the wind stress does not increase the residual overturning (Munday et al., 2013).

However, a recent model study using CCSM4 has suggested that the SO wind stress do not possess strong control on the strength of the AMOC, but rather the way in which the AMOC is closed (Jochum and Eden, 2015). In the limit of strong wind stress, the water that is subducted in the northern hemisphere is returned to the surface by the adiabatic pathway in the SO. In the opposite limit (no winds), however, the water returns in the equatorial Indo-Pacific Ocean through diapycnal mixing, with no or weak effect on the AMOC strength, despite the lack of eddy compensation in the model. An increase in wind stress magnitude only produces a stronger recirculation in the SO.

This result contrasts with the previous finding, but is defended by the compromised basin geometry of the idealized model study, which do not have a Pacific Ocean, and hence inhibit the diabatic pathway.

Then, in the light of this study and the present context, the implimentation of a correct specification of the thickness diffusivity is expected to have strong implications for the MOC and the atmospheric carbon-dioxide balance (Sigman and Boyle, 2000), due to enhanced compensation by eddies, but not with respect to the AMOC.

Another important aspect of the climate system is the apparent connection between the climate signals in the two hemispheres, observed in ice core records from Greenland and Antarctica. Currently, the accepted explanation to this phenomenon is that of the bipolar seesaw (Stocker and Johnson, 2003), where a cooling-event in the north will coincide with a warming in the south, and visa versa, due to a net northward heat transport in the region of the Atlantic Ocean, even at SH latitudes. However, the role of the Atlantic Ocean in transmitting such an interhemispheric climate signal is yet not fully understood, mainly because of the SO, where the ACC is able to work as a barrier to meridional signal propagation Rheinlænder (2015). One standing hypothesis is that the eddies of the SO are important agents in bringing the signal across the ACC. Then, in order to generate a correct global climate response, the ocean models are again dependent on the correct formulation of κ_{GM} (Ferrari and Nikurashin, 2010).

Chapter 7

Conclusion

This study has attempted to answer the four scientific questions, presented in the introduction, with the use of a 1000 yr integration of the fully coupled configuration of the Community Climate System Model version 4 (CCSM4) (Gent et al., 2011). The run is documented in Kleppin et al. (2015), and eddies are modeled using the GM-parameterization (Gent and McWilliams, 1990) with the associated thickness diffusivity formulated in terms of the ocean stratification (Ferreira et al., 2005).

It has been shown that a convenient framework in which to discuss Southern Ocean (SO) dynamics is that of the residual-mean (Marshall and Radko, 2003). In this theory, the Meridional Overturning Circulation (MOC) is composed of two cells. The Eulerian-mean cell, which is driven by the winds through Ekman dynamics, and a counter-flowing eddy-induced cell, which is fueled by the potential energy associated with the meridional density gradient, through baroclinic instability. Their interplay determines the density structure of the SO, and thereby the strength of the Antarctic Circumpolar Current (ACC).

Four different low-pass filtered wind stress metrics have been tested for relevance to the SO circulation (Allison et al., 2010). These are:

1. The zonally-averaged zonal wind stress at the latitude of the northern edge of the Drake Passage.

2. The average zonal wind stress within the Drake Passage latitude band.

3. The maximum of the zonally-averaged zonal wind stress.

4. The mean zonal wind stress over the path of the ACC.

All of these metrics are found to compare well in phase. This is expected, since they all are a product of some sort of zonal averaging, and because the dominating mode of zonal wind stress variability in the southern hemisphere is zonally symmetric (Thompson and Wallace, 2000). This is also shown to be true for the model through an Empirical Orthogonal Function (EOF) analysis, where the leading function explains about 40% of the variance. However, the time-mean and the variability differ across the forcing metrics, with fluctuations of 4% of the mean for the wind stress over the path of the ACC, against as much as 7% for the wind stress averaged within the Drake Passage latitude band.

In a comparison to the circumpolar volume transport at the Drake Passage, none of these metrics suggest a simple and robust relationship to the SO circulation. Evidently the variability in the Drake Passage transport on a decadal timescale is strongly dependent on other physical processes, such as surface buoyancy fluxes (Gent et al., 2001) and diapycnal mixing (Gnanadesikan, 1999), in addition to the wind forcing. A fifth measure of the wind stress, obtained from a region to which the Drake Passage transport has shown to be highly sensitive, did also not aid the establishment of a relationship (Mazloff, 2012).

The Ekman dynamics that governs the strength of the Eulerian-mean cell provides a strong constraint on the wind stress metrics, as these are expected to be directly proportional (Marshall and Radko, 2003). It is found that the wind stress over the path of the ACC meets this requirement most satisfactory, with a correlation coefficient of $r = 0.8$. This metric captures the flux of momentum into the ACC where the overturning controls the isopycnal slope, why its success is not a surprise. Moreover, this metric is found to correlate well with the variability in the SAM. Both quantities are therefore deemed relevant to the discussion on the forcing of the SO circulation.

A measure of the mean isopycnal slope within the core of the ACC has been derived for the upper 2000 m of the water column, through the use of the baroclinic potential energy (Borowski et al., 2002). A comparison of this proxy to the wind stress over the path of the ACC highlights that the two variables are in fact dependent (Marshall and Speer, 2012). Their correlation peaks when the wind stress signal leads the ocean response by a couple of years, due to the slow propagation of the baroclinic signal (Rintoul and Garabato, 2013). However, the correlation is weak, which is partly ascribed to the internal variability of the model.

The relationship is however more evident from a study of the three strongest multi-decadal wind stress trends of the model run, which consistently show that the large-scale isopycnal steepens with stronger wind stress. All three wind stress trends are significant

at the 10% level, and the same is true for two of the ocean responses.

An estimate of the barotropic component of the ACC core transport is obtained through an additional simple decomposition of the zonal velocity field. It is shown that the barotropic response often is concurrent with the baroclinic ($r = 0.73$). This covariability is consistent with the results from a recent model study, but which focused on the interannual timescale (Langlais et al., 2015). As for the baroclinic component, its relationship with the wind stress over the path of the ACC is not well determined through this analysis.

Where the variability in the wind stress over the ACC path is found to generate similar fluctuations in the wind-driven overturning, the variability in the counter-acting eddy-induced circulation is found to correlate less with the wind stress ($r = -0.56$), and is less variable. It follows that the strength of the residual overturning is a strong function of the wind stress, and that the isopycnal slope is relatively sensitive to wind stress change.

It has previously been shown that coarse resolution models with a GM parameterization for isopycnal mixing generates too little eddy compensation i.e. that the residual circulation is too sensitive to a sustained change in the wind stress (Hallberg and Gnadadesikan, 2006; Jochum and Eden, 2015). It is therefore likely that the model MOC is overly sensitive to the decadal variability in wind stress as well, and that the documented response in the isopycnal slope is overestimated. This result is in favor of the finding by Böning et al. (2008), that the density structure of the SO is remarkably insensitive to the ongoing intensification of the southern hemisphere westerlies.

The insufficient representation of eddy compensation in coarse resolution models coincides with an inability to mimic eddy saturation (Munday et al., 2013). That is, the limit in which the time-mean circumpolar transport of the ACC becomes independent from the wind stress (Hogg and Blundell, 2006). These drawbacks are atleast partly related to an incomplete specification of the eddy transfer coefficient κ_{GM}. The results from this thesis emphasize the need of a continous effort to formulate a physical consistent eddy transfer coefficient, to ensure accurate climate predictions for the eddy-rich Southern Ocean.

Bibliography

Allison, L. C., H. Johnson, and D. P. Marshall (2011). Spin-up and adjustment of the antarctic circumpolar current and global pycnocline. *Journal of marine research 69*, 167–189.

Allison, L. C., H. L. Johnson, D. P. Marshall, and D. R. Munday (2010). Where do the winds drive the antarctic circumpolar current? *Geophysical Research Letters 37*, L12605.

Anderson, D. L. T., K. Bryan, A. E. Gill, and R. C. Pacanowski (1979). The transient response of the north atlantic: Some model studies. *Journal of Geophysical Research 84*, 4795–4815.

Borowski, D., R. Gerdes, and D. Olbers (2002). Thermohaline and wind forcing of a circumpolar channel with blocked geostrophic contours. *Journal of Oceanography 32*, 2520–2540.

Böning, C. W., A. Dispert, M. Visbeck, S. R. Rintoul, and F. U. Schwarzkopf (2008). The response of the antarctic circumpolar current to recent climate change. *Nature Geoscience 1*, 864–869.

Chelton, D. B., R. A. DeSzoeke, M. G. Schlax, K. E. Naggar, and N. Siwertz (1998). Geographical variability of the first baroclinic rossby radius of deformation. *Journal of Physical Oceanography 28*, 433–460.

Cunningham, S. A., S. G. Alderson, B. A. King, and M. A. Brandon (2003). Transport and variability of the antarctic circumpolar current in drake passage. *Journal of Geophysical Research 108 (C5)*, 8084.

Danabasoglu, G., S. C. Bates, B. P. Briegleb, M. Jochum, W. G. Large, S. Peacock, and S. G. Yeager (2012). The ccsm4 ocean component. *Journal of Climate 25*, 1361–1389.

Danabasoglu, G. and J. Marshall (2007). Effects of vertical variations of thickness diffusivity in an ocean general circulation model. *Ocean Modelling 18*, 122–141.

Eden, C. and R. J. Greatbatch (2008). Towards a mesoscale eddy closure. *Ocean Modelling 20*, 223–239.

Emery, W. J. and R. E. Thompson (1997). *Data analysis methods in physical oceanography* (1st ed.). Elsevier.

Ferrari, R. and M. Nikurashin (2010). Suppresion of eddy diffusivity across jets in the southern ocean. *Journal of Physical Oceanography 40*, 1501–1519.

Ferreira, D., J. Marshall, and P. Heimbach (2005). Estimating eddy stresses by fitting dynamics to observations using a residual-mean ocean circulation model and its adjoint. *Journal of Physical Oceanography 35*, 1891–1910.

Flato, G., J. Marotzke, B. Abiodun, S. C. Braconnot, W. C. Chou, P. Cox, F. Driouech, S. Emori, V. Eyring, C. Forest, P. Gleckler, E. Guilyardi, C. Jakob, V. Kattsov, C. Reason, and M. Rummukainen (2013). Evaluation of climate models. In *Climate Change 2013: The Physical Science Basis. Contribribution of Working Group I to the Fifth Assessment Report of the Intergovernmental Panel on Climate Change*, Chapter 9. Cambridge University Press, Cambridge, United Kingdom and New York, NY, USA.

Fyfe, J. C. and O. A. Saenko (2006). Simulated changes in the extratropical southern hemisphere winds and currents. *Geophysical Research Letters 33*, L06701.

Gent, P. R. and G. Danabasoglu (2011). Reponse to increasing southern hemisphere winds in ccsm4. *Journal of climate 24*, 4992–4998.

Gent, P. R., G. Danabasoglu, L. J. Donner, M. M. Holland, E. C. Hunke, S. R. Jayne, D. M. Lawrence, R. B. Neale, P. J. Rasch, M. Vertenstein, P. H. Worley, Z.-L. Yang, and M. Zhang (2011). The community climate system model version 4. *Journal of Climate 24*, 4973–4991.

Gent, P. R. and J. C. McWilliams (1990). Isopycnal mixing in ocean circulation models. *Journal of Physical Oceanography 20*, 150–155.

Gent, P. R., J. Willebrand, T. J. McDougall, and J. C. McWilliams (1995). Parameterizing eddy-induced tracer transports in ocean circulation models. *Journal of Physical Oceanography 25*, 463–474.

Gent, P. R., G. L. William, and F. O. Bryan (2001). What sets the mean transport through drake passage? *Journal of Geophysical Research 106*, 2693–2712.

Gille, S. (2003). Float observations of the southern ocean. part ii: Eddy fluxes. *Journal of Physical Oceanography 33*, 1182–1196.

Gille, S. T. (1994). Mean sea surface height of the antarctic circumpolar current from geosat data: Method and application. *Journal of Geophysical Research 99*, 18225–18273.

Gnanadesikan, A. (1999). A simple predictive model for the structure of the oceanic pycnocline. *Science 283*, 2077–2079.

Hallberg, R. and A. Gnadadesikan (2001). An exploration of the role of transient eddies in determining the transport of a zonally reentrant channel. *Journal of Physical Oceanography 31*, 3312–3330.

Hallberg, R. and A. Gnadadesikan (2006). The role of eddies in determining the structure and response of the wind-driven southern hemisphere overturning: Results from the modeling eddies in the southern ocean (meso) project. *Journal of Physical Oceanography 36*, 2232–2252.

Hogg, A., M. P. Meredith, D. P. Chambers, E. P. Abrahamsen, C. W. Hughes, and A. K. Morrison (2015). Recent trends in the southern ocean eddy field. *Journal of geophysical research 120*, 257–267.

Hogg, A. M. and J. R. Blundell (2006). Interdecadal variability of the southern ocean. *Journal of Physical Oceanography 36*, 1626–1645.

Hogg, A. M., J. R. Blundell, M. P. Meredith, and C. Wilson (2008). Eddy heat flux in the southern ocean: Response to variable wind forcing. *Journal of Climate 21*, 608–620.

Holton, J. R. (2004). *An introduction to Dynamical Meteorology* (4th ed.). Elsevier.

Ivchenko, V. O., A. M. Treguier, and S. E. Best (1997). A kinetic energy budget and internal instabilities in the fine resolution antarctic model. *Journal of Physical Oceanography 27*, 5–22.

Jochum, M. and C. Eden (2015). The connection between southern ocean winds, atlantic meridional overturning circulation and indo-pacific upwelling. Early online release, Journal of Climate.

Jochum, M., A. Jahn, S. Peacock, D. A. Bailey, J. T. Fasullo, J. Kay, S. Levis, and B. Otto-Bliesner (2012). True to milankovitch: Glacial inception in the new community climate system model. *Journal of Climate 25*, 2226–2239.

Johnson, G. C. and L. H. Bryden (1989). On the size of the antarctic circumpolar current. *Deep-sea Research 36*, 39–55.

Kim, Y. S. and A. H. Orsi (2014). On the variability of antarctic circumpolar current fronts inferred from 1992-2011 altimetry. *Journal of Physical Oceanography 44*, 3054–3071.

Kleppin, H., M. Jochum, B. Otto-Bliesner, C. A. Shields, and S. Yeager (2015). Stochastic atmospheric forcing as a trigger for sudden greenland warmings. *Journal of Climate 28*, 7741–7763.

Knauss, J. A. (2005). *Introduction to Physical Oceanography* (2nd ed.). Waveland Press, inc.

Langlais, C. E., S. R. Rintoul, and J. D. Zika (2015). Sensitivity of antarctic circumpolar current transport and eddy activity to wind patterns in the southern ocean. *Journal of Physical Oceanography 45*, 1051–1067.

Large, W. G. and S. G. Yeager (2004). Diurnal to decadal global forcing for ocean and sea-ice models: The data sets and flux climatologies. Technical report, National Center for Atmospheric Research, Boulder, Colorado.

Lorenz, E. N. (1955). Available potential energy and the maintenance of the general circulation. *Tellus 2*, 157–167.

Marshall, G. J. (2003). Trends in the southern annular mode from observations and reanalyses. *Journal of Climate 1*, 4134–4143.

Marshall, G. J. and W. M. Connolley (2006). Effect of changing southern hemisphere winter sea surface temperatures on the southern annular mode strength. *Geophysical Research Letters 33*, L17717.

Marshall, J. and T. Radko (2003). Residual-mean solutions for the antartic circumpolar current and its associated overturning circulation. *Journal of Physical Oceanography 33*, 2341–2354.

Marshall, J. and K. Speer (2012). Closure of the meridional overturning circulation through southern ocean upwelling. *Nature Geoscience 5*, 171–180.

Mazloff, M. R. (2012). On the sensitivity of the drake passage transport to air-sea momentum flux. *Journal of Climate 25*, 2279–2290.

Mazloff, M. R., P. Heimbach, and C. Wunsch (2010). An eddy-permitting southern ocean state estimate. *Journal of Physical Oceanography 40*, 880–899.

Meredith, M. P. and Coauthors (2011). Sustained monitoring of the southern ocean at drake passage: Past achievements and future priorities. *Reviews of Geophysics 49*, RG4005.

Meredith, M. P. and A. M. Hogg (2006). Circumpolar response of southern ocean eddy activity to a change in the southern annular mode. *Geophysical Research Letters 33*, L16608.

Morrow, R., M. L. Ward, A. Hogg, and S. Pasquet (2010). Eddy response to southern ocean climate modes. *Journal of Geophysical Research 115*, C10030.

Munday, D. R., H. L. Johnson, and D. P. Marshall (2013). Eddy saturation of equilibrated circumpolar currents. *Journal of Physical Oceanography 43*, 507–532.

Munk, W. H. and E. Palmén (1951). Note on the dynamics of the antarctic circumpolar current. *Tellus 3*, 53–55.

Nadeau, L. and D. N. Straub (2009). Basin and channel contributions to a model antarctic circumpolar current. *Journal of Physical Oceanography 39*, 986–1002.

Nadeau, L. and D. N. Straub (2012). Influence of wind stress, wind stress curl, and bottom friction on the transport of a model antarctic circumpolar current. *Journal of Physical Oceanography 42*, 207–222.

Orsi, A. H., T. Whitworth, and W. D. Nowlin (1995). On the meridional extent and fronts of the antarctic circumpolar current. *Deep-sea Research 42*, 641–673.

Pedlosky, J. (1996). *Ocean Circulation Theory* (1st ed.). Springer.

Rheinlænder, J. W. (2015). Interhemispheric climate variability in a pre-industrial control simulation of ccsm4. Master's thesis, University of Copenhagen, Niels Bohr Institute, Centre for Ice and Climate.

Riley, K. F., M. P. Hobson, and S. J. Bence (2006). *Mathematical Methods for Physics and Engineering* (3rd ed.). Cambridge University Press.

Rintoul, S. R. and A. C. N. Garabato (2013). *Ocean Circulation and Climate - A 21st Century Perspective* (2nd ed.), Volume 103. Academic Press.

Roquet, F., C. Wunsch, and G. Madec (2011). On the patterns of wind-power input to the ocean circulation. *Journal of Physical Oceanography 41*, 2328–2342.

Sallée, J. B., K. Speer, and R. Morrow (2008). Response of the antarctic circumpolar current to atmospheric variability. *Journal of Climate 21*, 3020–3039.

Sigman, D. M. and E. A. Boyle (2000). Glacial/interglacial variations in atmospheric carbon dioxide. *Nature 407*, 859–869.

Smith, R. D. and Coauthors (2010). The parallel ocean program (pop) reference manual, ocean component of the community climate system model (ccsm). Technical report, Los Alamos National Laboratory.

Smith, W. H. and D. T. Sandwell (1997). Global sea floor topography from satellite altimetry and ship depth soundings. *Science Magazine 277*, 1956–1962.

Solomon, S. and D. W. J. Thompson (2002). Interpretation of recent southern hemisphere climate change. *Science 296*, 895–899.

Stocker, T. F. and S. J. Johnson (2003). A minimum thermodynamic model for the bipolar seesaw. *Paleoceanography 18(4)*, 1087.

Stommel, H. (1957). A survey of ocean current theory. *Deep-sea Research 6*, 149–184.

Stommel, H. and A. B. Arons (1959). On the abyssal circulation of the world ocean - i. stationary planetary flow patterns on a sphere. *Deep Sea Research 6*, 140–154.

Storch, J. V., C. Eden, I. Fast, H. Haak, D. Hernández-Decker, E. Maier-Reimer, J. Marotzke, and D. Stammer (2012). An estimate of the lorenz energy cycle for the world ocean based on the 1/10° storm/ncep simulation. *Journal of Physical Oceanography 42*, 2185–2205.

Talley, L., G. Pickard, W. Emery, and J. Swift (2011). *Descriptive Physical Oceanography: An Introduction* (6th ed.). Elsevier, Boston.

Thompson, A. (2008). The atmospheric ocean: Eddies and jets in the antarctic circumpolar current. *Philosophical transactions of the royal society 366*, 4529–4541.

Thompson, A. F. and A. C. N. Garabato (2014). Equilibration of the antarctic circumpolar current by standing meanders. *Journal of Physical Oceanography 44*, 1811–1828.

Thompson, D. W. J. and J. M. Wallace (2000). Annular modes in the extratropical circulation. part i: Month-to-month variability. *Journal of Climate 13*, 1000–1016.

Toggweiler, J. R. and B. Samuels (1995). Effect of drake passage on the global thermohaline circulation. *Deep-Sea Research 42*, 477–500.

Vallis, G. K. (2006). *Atmospheric and Oceanic Fluid Dynamics* (1st ed.). Cambridge University press.

Visbeck, M., J. Marshall, T. Haine, and M. Spall (1997). Specification of eddy transfer coefficients in coarse-resolution ocean circulation models. *Journal of Physical Oceanography 27*, 381–402.

Williams, R. G., C. Wilson, and C. W. Hughes (2007). Ocean and atmosphere storm tracks: the role of eddy vorticity forcing. *Journal of Physical Oceanography 37*, 2267–2289.

Wunsch, C. (1998). The work done by the wind on the oceanic general circulation. *Journal of Physical Oceanography 28*, 2332–2340.

Yuan, X. (2004). High-wind-speed evaluation in the southern ocean. *Journal of Geophysical Research 109*, D13101.

Zika, J. D., J. L. Sommer, C. O. Dufour, A. N. Garabato, and A. Blaker (2013). Acceleration of the antarctic circumpolar current by wind stress along the coast of antarctica. *Journal of Physical Oceanography 43*, 2772–2784.

Appendices

Appendix A

The vertically- and zonally-integrated boussinesq-approximated momentum equation

This section derives the vertically- and zonally-integrated boussinesq-approximated momentum equation, which is fundamental to the zonally-integrated models. The derivation departures in the Euler equation,

$$\frac{D\boldsymbol{v}}{Dt} + f\boldsymbol{k} \times \boldsymbol{v} = -\frac{1}{\rho}\nabla p + \frac{1}{\rho}\frac{\partial \boldsymbol{\tau}}{\partial z} - g\boldsymbol{k}, \tag{A.1}$$

and with the pressure and density field decompositions

$$\begin{aligned} \rho(x, y, z, t) =& \rho_0 + \delta\rho(x, y, z, t) \\ p(x, y, z, t) =& p_0(z) + \delta p(x, y, z, t). \end{aligned}$$

Here $\boldsymbol{v} = (u, v, w)$ is the three dimensional velocity field, f is the Coriolis parameter, $\boldsymbol{k} = (0, 0, 1)$ is the vertical unit vector, ρ is the density field, p the pressure field, $\boldsymbol{\tau} = (\tau^x, \tau^y, 0)$ is the interfacial stress vector field and g is the gravitational acceleration. The decomposition of the density field involves a deviation density $\delta\rho$ that fluctates around the mean ρ_0, and likewise for the pressure field decomposition, where the reference pressure field is dependent on depth only, $p_0(z)$, and the reference density and pressure are in hydrostatic balance by definition,

$$\frac{\partial p_0(z)}{\partial z} = -\rho_0 g. \tag{A.2}$$

It is assumed that $\rho_0 \gg \delta\rho$ and $p_0 \gg \delta p$.

Inserting the decomposition in eq. (A.1) results in

$$(\rho_0 + \delta\rho)\left(\frac{D\boldsymbol{v}}{Dt} + f\boldsymbol{k}\times\boldsymbol{v}\right) = -\boldsymbol{k}\frac{\partial p_0}{\partial z} - \nabla\delta p + \frac{\partial\boldsymbol{\tau}}{\partial z} - g\rho_0\boldsymbol{k} - g\delta\rho\boldsymbol{k}$$

and using the hydrostatic balance (A.2) and the fact that $\rho_0 \gg \delta\rho$ results in

$$\frac{D\boldsymbol{v}}{Dt} + f\boldsymbol{k}\times\boldsymbol{v} = -\frac{1}{\rho_0}\nabla\delta p + \frac{1}{\rho_0}\frac{\partial\boldsymbol{\tau}}{\partial z} - g\delta\rho\boldsymbol{k}. \tag{A.3}$$

This is the three-dimensional boussinesq-approximated momentum equation, and we will in the following assume that the deviation density and pressure field balance eachother i.e.

$$\frac{\partial\delta p}{\partial z} = -\delta\rho g. \tag{A.4}$$

Integrating the horizontal part of (A.3) in the vertical from the bottom $\eta_B(x,y)$ to the surface $\eta_S(x,y)$ of the water column results in

$$\frac{\partial}{\partial t}\int_{\eta_B}^{\eta_S}\boldsymbol{u}\,\mathrm{d}z + \int_{\eta_B}^{\eta_S}(\boldsymbol{v}\cdot\nabla)\boldsymbol{u}\,\mathrm{d}z + f\boldsymbol{k}\times\int_{\eta_B}^{\eta_S}\boldsymbol{u}\,\mathrm{d}z = -\frac{1}{\rho_0}\int_{\eta_B}^{\eta_S}\nabla_2\delta p\,\mathrm{d}z + \frac{1}{\rho_0}(\boldsymbol{\tau}_S - \boldsymbol{\tau}_B)$$

where $\boldsymbol{u} = (u,v)$ is the horizontal velocity field, ∇_2 is the horizontal counterpart to ∇, $\boldsymbol{\tau}_S = \boldsymbol{\tau}(x,y,z=\eta_S)$ is the surface wind stress and $\boldsymbol{\tau}_B = \boldsymbol{\tau}(x,y,z=\eta_B)$ is the bottom stress.

Exploiting the smallness of variation in the surface height η_S compared to bottom topography variations η_B, we assume a rigid lid and set $\eta_S = 0$ at $z = 0$. Moreover we use Leibnitz' rule of integration (see Riley et al. (2006), chapter five) to rewrite the pressure gradient term, because the lower bound on the integral depends on x and y:

$$\int_{\eta_B(x,y)}^{0}\nabla_2\delta p\,\mathrm{d}z = \nabla_2\int_{\eta_B(x,y)}^{0}\delta p\,\mathrm{d}z + \delta p_B\nabla_2\eta_B. \tag{A.5}$$

Here $\delta p_B = \delta p(x,y,z=\eta_B)$ is the bottom deviation pressure field. Inserting eq. (A.5), the momentum equation changes to

$$\frac{\partial}{\partial t}\int_{\eta_B}^{0}\boldsymbol{u}\,\mathrm{d}z + \int_{\eta_B}^{0}(\boldsymbol{v}\cdot\nabla)\boldsymbol{u}\,\mathrm{d}z + f\boldsymbol{k}\times\int_{\eta_B}^{0}\boldsymbol{u}\,\mathrm{d}z = -\frac{1}{\rho_0}\nabla_2\int_{\eta_B}^{0}\delta p\,\mathrm{d}z - \frac{1}{\rho_0}\delta p_B\nabla_2\eta_B + \frac{1}{\rho_0}(\boldsymbol{\tau}_S - \boldsymbol{\tau}_B). \tag{A.6}$$

This is the vertically-integrated boussinesq-approximated momentum equation.

The zonal steady-state component of eq. (A.6) is

$$\int_{\eta_B}^{0} (\boldsymbol{v}\cdot\nabla)u\,\mathrm{d}z - f\int_{\eta_B}^{0} v\,\mathrm{d}z = -\frac{1}{\rho_0}\frac{\mathrm{d}}{\mathrm{d}x}\int_{\eta_B}^{0}\delta p\,\mathrm{d}z - \frac{1}{\rho_0}\delta p_B\frac{\partial\eta_B}{\partial x} + \frac{1}{\rho_0}(\tau_S^x - \tau_B^x).$$

Using the continuity equation $\nabla\cdot\boldsymbol{v} = 0$ enables us to rewrite the first term on the left hand side (LHS) to

$$\int_{\eta_B}^{0} (\boldsymbol{v}\cdot\nabla)u\,\mathrm{d}z = \int_{\eta_B}^{0}\frac{\partial uu}{\partial x} + \frac{\partial vu}{\partial y}\,\mathrm{d}z$$

because $w(z=0) = w(z=\eta_B) = 0$.

This means that the momentum balance now reads

$$\int_{\eta_B}^{0}\frac{\partial uu}{\partial x}\,\mathrm{d}z + \int_{\eta_B}^{0}\frac{\partial uv}{\partial y}\,\mathrm{d}z - f\int_{\eta_B}^{0} v\,\mathrm{d}z = -\frac{1}{\rho_0}\frac{\mathrm{d}}{\mathrm{d}x}\int_{\eta_B}^{0}\delta p\,\mathrm{d}z - \frac{1}{\rho_0}\delta p_B\frac{\partial\eta_B}{\partial x} + \frac{1}{\rho_0}(\tau_{\eta_S}^x - \tau_{\eta_B}^x).$$

Now we execute a zonal integral on the momentum equation. First we note that continuity requires that

$$f\oint\int_{\eta_B}^{\eta_S} v\,\mathrm{d}z\,\mathrm{d}x = 0.$$

Furthermore, the zonal pressure gradient does also vanish, because the zonal integral is periodic,

$$\oint\frac{\mathrm{d}}{\mathrm{d}x}\int_{\eta_B}^{0}\delta p\,\mathrm{d}z\,\mathrm{d}x = \int_{\eta_B}^{0}\delta p(x=L) - \delta p(x=0)\,\mathrm{d}z = 0,$$

because $\delta p(x=L) = \delta p(x=0)$, since the two longitudinal positions coincide. Likewise, $u(x=0) = u(x=L)$ and the $\frac{\partial uu}{\partial x}$ vanish too. We are thus left with the balance

$$\oint\mathrm{d}x\left[\int_{\eta_B}^{0}\frac{\partial(uv)}{\partial y}\,\mathrm{d}z + \frac{1}{\rho_0}p_B\frac{\partial\eta_B}{\partial x} + \frac{1}{\rho_0}\tau_B^x = \frac{1}{\rho_0}\tau_S^x\right].$$

Appendix B

Baroclinic potential energy

To arrive at the vertically integrated momentum equation, with the baroclinic potential energy term occuring explicitly, we rewrite the pressure gradient in eq. (A.6) term the following way:

$$\int_{\eta_B}^{0} \delta p \, \mathrm{d}z = \int_{\eta_B}^{0} \left[\mathrm{d}(z\delta p) - z \frac{\partial \delta p}{\partial z} \mathrm{d}z \right].$$

Executing the integral while using eq. (A.4) gives

$$\int_{\eta_B}^{0} \delta p \, \mathrm{d}z = -\delta p_B \eta_B + g \int_{\eta_B}^{0} z\delta\rho \, \mathrm{d}z = -\delta p_B \eta_B + \rho_0 \chi$$

where

$$\chi = \frac{g}{\rho_0} \int_{\eta_B}^{0} z\delta\rho \, \mathrm{d}z. \tag{B.1}$$

χ is the baroclinic potential energy (BPE).

Inserting in eq. (A.6) results in

$$\frac{\partial \boldsymbol{U}}{\partial t} + f\boldsymbol{k} \times \boldsymbol{U} = \frac{1}{\rho_0}\eta_B \nabla_2 \delta p_B - \nabla_2 \chi + \frac{1}{\rho_0}(\boldsymbol{\tau}_S - \boldsymbol{\tau}_B) + \boldsymbol{G} \tag{B.2}$$

with

$$\boldsymbol{U} = (U, V) = \int_{\eta_B}^{0} \boldsymbol{u} \, \mathrm{d}z$$

and

$$\boldsymbol{G} = -\int_{\eta_B}^{0} (\boldsymbol{v} \cdot \nabla)\boldsymbol{u} \, \mathrm{d}z.$$

Appendix C

The Southern Annular Mode

The state of the Southern Annular Mode (SAM) is well captured by its associated index,

$$\text{SAM} = p^*_{40^\circ\text{S}} - p^*_{65^\circ\text{S}}, \tag{C.1}$$

where $p^*_{40^\circ\text{S}}$ and $p^*_{65^\circ\text{S}}$ are the normalized zonally-averaged sea level pressures (SLP) at 40°S and 65°S, respectively (Marshall, 2003). This index, based on the model SLP, is shown in the upper panel of figure C.1. When this index is positive i.e. when the zonally-averaged SLP at 40°S is greater than normal, and opposite at 65°S, the meridional isobars are relatively steep, and the westerlies blow stronger. The opposite is true for a negative index. The lower panel of figure C.1 displays the absolute value of the slope coefficient to a running fifthy-year linear least squares fit, and helps to determine the temporal location of the strongest trends in the SAM.

Figure C.2 shows the maximum of the zonally-averaged zonal wind stress for the time span 1958 to 2001, and is obtained from the European Centre for Medium-Range Weather Forecasts (ECMWF) reanalysis product, ERA40. Superposed is a linear least squares fit that shows the present intensification of the wind stress.

Figure C.3 shows the three strongest trends in the maximum of the zonally-averaged zonal wind stress in the model run, picked with the aid of the lower panel in figure C.1. The coefficients of the fits presented in both figure C.2 and C.1 are given in table 4.1.

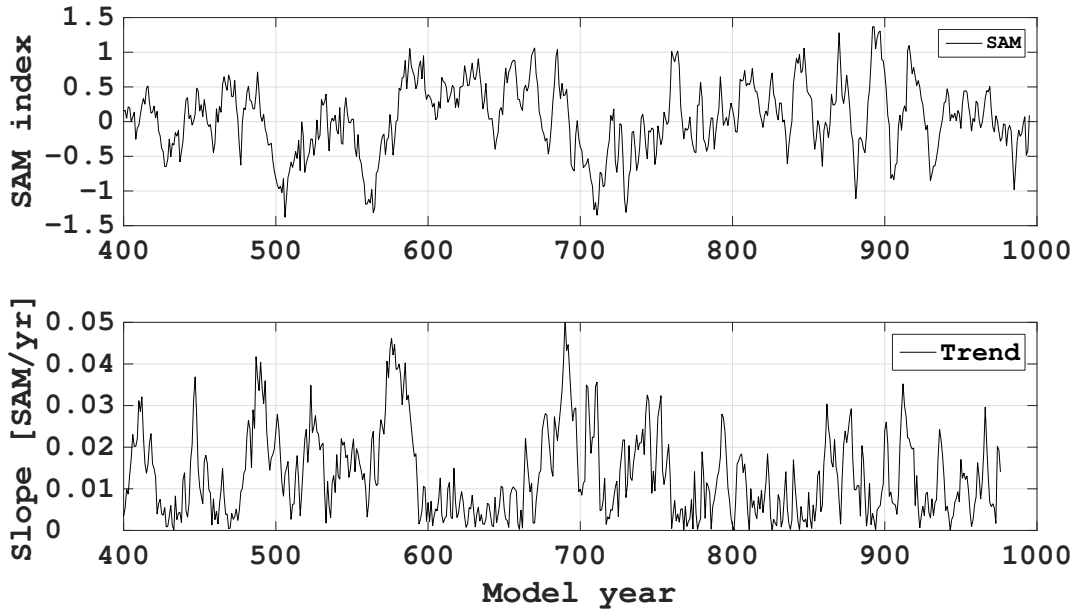

Figure C.1: The upper panel displays the annual mean SAM index calculated from the difference between the zonally-averaged monthly-mean sea level pressure field at 40°S and 65°S. Normalization is obtained by dividing through with the corresponding temporal means and multiplying by a factor of 10^3. A ten-year running mean has been applied to the signal. The lower panel displays a fifty-year running linear trend in the annual-mean unsmoothed SAM. The y-axis is the absolute value of the slope of this trend in the SAM index.

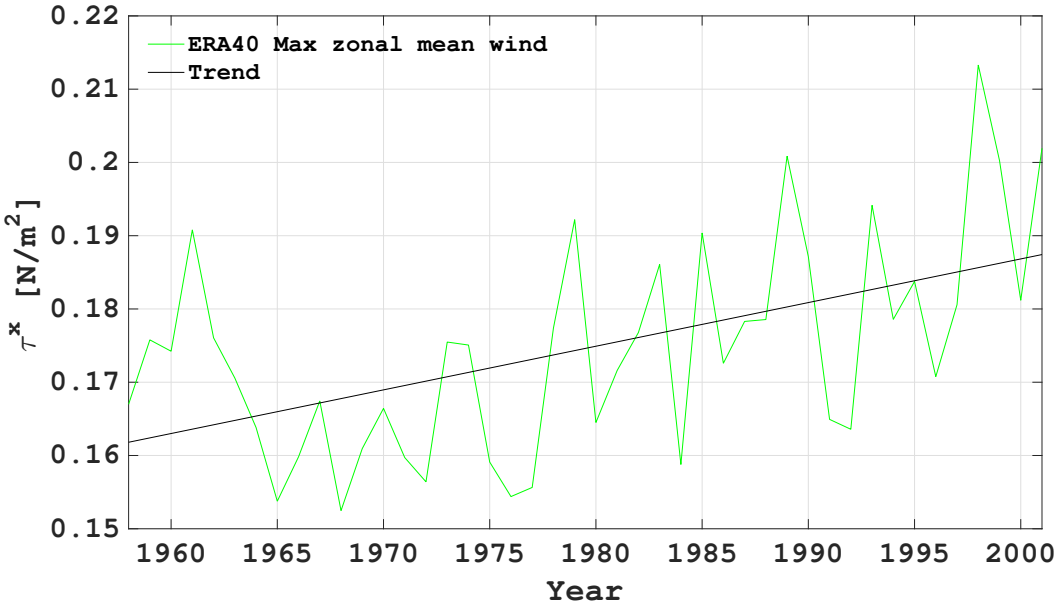

Figure C.2: The green line is the annual mean maximum of the zonally-averaged zonal wind stress field in the ERA40 reanalysis product. The black line is a linear least squares fit to the wind stress time series and suggests a 50 yr increase in the present SO zonal wind stress of $0.030 \pm 0.007 \mathrm{N/m^2}$.

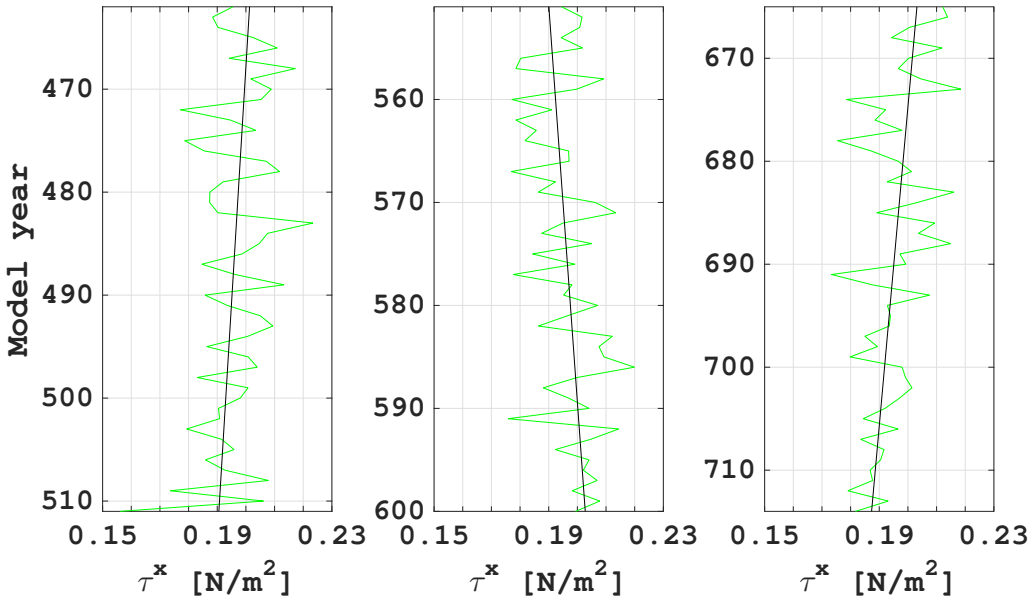

Figure C.3: The three strongest 50 yr wind stress trends in the SO, choosen with the aid of figure C.1 in appendix C. The green lines are the annual mean maximum of the zonally-averaged zonal wind stress, and the black lines are linear least squares fits to the wind stress time series. The coefficients of the fit are found in table 4.1.